Dielectric, Ferroelectric and Impedance Spectroscopic Studies of $AgNbO_3$ and its Modified Systems

Rakesh Muduli

Physics and Astronomy

National Institute of Technology Rourkela

Dielectric, Ferroelectric and Impedance Spectroscopic Studies of $AgNbO_3$ and its Modified Systems

Dissertation submitted to the
National Institute of Technology Rourkela
in partial fulfillment of the requirements
of the degree of
Doctor of Philosophy
in
Department of Physics and Astronomy
by

Rakesh Muduli
(510PH105)

Under the supervision of
Prof. Simanchala Panigrahi
and
Prof. Pawan Kumar

September 30, 2016.
Department of Physics and Astronomy
National Institute of Technology Rourkela

Physics and Astronomy

National Institute of Technology Rourkela

September 30, 2016

Supervisors' Certificate

This is to certify that the work presented in this dissertation entitled "Dielectric, Ferroelectric and Impedance Spectroscopic Studies of $AgNbO_3$ and its Modified Systems" by Rakesh Muduli", RollNumber 510PH105, is a record of original research carried out by him under our supervision and guidance in partial fulfillment of the requirements of the degree of *Doctor of Philosophy* in *Physics and Astrophysics*. Neither this dissertation nor any part of it has been submitted for any degree or diploma to any institute or university in India or abroad.

<Co-Supervisor's Name>
Co-Supervisor

<Supervisor's Name>
Principal Supervisor

कर्मण्येवाधिकारस्तेमाफलेषुकदाचन।

माकर्मफलहेतुर्भूर्मातेसङ्गोऽस्त्वकर्मणि॥

Dedicated to

my nation

my village

my family

Declaration of Originality

I, Rakesh Muduli, Roll Number 510PH105 hereby declare that this dissertation entitled *"Dielectric, Ferroelectric and Impedance Spectroscopic Studies of $AgNbO_3$ and its Modified Systems"* represents my original work carried out as a doctoral student of NIT Rourkela and, to the best of my knowledge, it contains no material previously published or written by another person, nor any material presented for the award of any other degree or diploma of NIT Rourkela or any other institution. Any contribution made to this research by others, with whom I have worked at NIT Rourkela or elsewhere, is explicitly acknowledged in the dissertation. Works of other authors cited in this dissertation have been duly acknowledged under the section "Bibliography". I have also submitted my original research records to the scrutiny committee for evaluation of my dissertation.

I am fully aware that in case of any non-compliance detected in future, the Senate of NIT Rourkela may withdraw the degree awarded to me on the basis of the present dissertation.

January 18, 2016 Rakesh Muduli

NIT Rourkela

ACKNOWLEDGEMENT

I am indebted to the **National Institute of Technology, Rourkela** of providing me the opportunity to pursue my Ph.D. programme.

I am grateful to the **Dept. of Physics and Astronomy** of selecting me as a research scholar.

I Praise in high tone to **Honourable Director Sir**, **Prof. Sunil ku. Sarangi** for creating a positive atmosphere in the institute for the research programme.

I express deep gratitude to my supervisor **Prof. S. Panigrahi** of accepting me as his student. His consistent support and proper guidance only led me to achieve this end.

I am also thankful to my Co-supervisor Prof**. P. Kumar** who always insists me to focus on the work.

I am very much thankful to the **H.O.D Prof. D. K. Bisoyi**, who created a very cordial atmosphere in the department

I am willingly obedient to my DSC members **Prof. S. C. Mishra, Prof. A. Mallick and Prof. D. K. Pradhan** who properly shaped my objective of research work.

I am indebted to **Prof. D. Behera** who provided me the Impedance Analyser for electrical measurement.

I honestly honour **Ganguly Sir, Jena Sir, Viswakarma Sir, Singh Sir, Mahanandia Sir, Kar Sir, Dash Sir, Chowdhury Sir** and others in the Dept being a source of inspiration. My sincerely thanks to **Ali Sir, Radharaman, Smita, DungDung Bhai, Balaram bhai, Lokanath Bhai, Prakash Bhai** and **Nana**.

I highly valued to Subrat, Senthil, Naresh ,Achyuta, Prakash (palei), Satya (N.Tripathy) for making me familiar with research. I am deeply thankful to **Ranjit (Kanha)**, **Jyoti, Prakash (Paku), Ranjit (Baba), Sudhansu** for their constant supports and cooperation. I want to give credit to my loving juniors Satya (Satapathy), Tapobrata, Surya, Bamadev, Prakash, Kailash, Soumya, Binayak, Satya (junior), Hari, Nilakantha, Chandrasekhar, Sourav, Vinesh, Sunirmal, Subhajit, Laxman, V. Ram, Asim, Budhhadev, Bibek, Aalok, Abhishek, S. Tarenia, Jayarao, Sukant, Jashashri, Sanghamitra, Sridevi, Arpana, Mousumi, Punyatoya, Priyadarshini, Kadambini, Priyanka, Kruttika, Rashmi, Sweta, Santripti, Krishna, Mithra, Smaranika, Krishna, Deepika

I am willing to share my success and happiness with my RSS brothers, friends and well-wisher.

Abstract

This thesis contains some fundamental understandings of mechanism related to the dielectric, ferroelectric and impedance spectroscopic study of $AgNbO_3$ and its modified systems. The results analysis are mostly qualitative in nature which has accounted previous reported facts while explaining as well as added some new concepts that fits to be more appropriate. The quantitative figures are less stressed in order to focus more on the underlying physics for different mechanisms of some particular electric properties in the titled compounds. The modified systems are designed by partially incorporating impurity atoms at the B-site of the ABO_3 perovskite compound. The impurity atoms are chosen of isovalent (Ta^{5+}, Sb^{5+}, V^{5+}) as well as alieovalent (Mn^{4+}, W^{6+}, Ti^{4+}) in nature. The alieovalent impurities are chosen to design charge carrier (electron/hole)-doped systems. The effect of Jahn-Teller ions (Mn^{3+}, W^{5+} and Ti^{3+}) on the ferroelectric properties also understood and properly explained. The role of impurities in bringing structural and microstructural changes and their effect on dielectric, ferroelectric and other electric properties of the compound is extensively analysed and discussed in the subsequent chapters.

This work was carried out to improve the dielectric and ferroelectric properties of $AgNbO_3$ to be an alternative for the hazardous lead (Pb) based ferroelectrics. This is because the dynamics of cations (Ag, Nb) and nature of Ag-O, Nb-O bonds in $AgNbO_3$ features similarly to that of the dynamics of cations in Pb-based compounds. The compound exhibits an exceptionally large spontaneous polarisation ($52\mu C/cm^2$) in its polycrystalline form at sufficient applied field (220kV/cm) and is comparable to 50 $\mu C/cm^2$ of polycrystalline $PbTiO_3$ ceramic, at room temperature. But, the former shows a poor 0.041 $\mu C/cm^2$ at ~12kV which is quite lower than the latter, which is a matter of concern. Multiple dielectric anomalies also appear in the temperature dependent permittivity of the compound which is related to the complex coupling between NbO_6 octahedra and the cations dynamics. Therefore, numbers of modifications were carried out to verify the effects of dopants on dielectric and ferroelectric parameters and to understand the underlying science of several mechanisms.

Solid state synthesis route is chosen to prepare samples for the investigated compound ($AgNbO_3$) in which required oxide materials are taken as raw precursors (Ag_2O, Nb_2O_5). Manual grinding is opted in order to properly mix the oxide powders for their homogeneous presence. Calcination and sintering are two thermal processes which are followed to bring the desired phase of the compound and to densify the pellet type sample for various experiments. The modified systems are titled with the element oxide (Ta_2O_5, Sb_2O_5, V_2O_5, MnO_2, WO_3, TiO_2)-doped $AgNbO_3$ systems. The amount of element oxides is measured in molecular weight fraction of Nb_2O_5 in order to partially incorporate the metal elements in place of Nb, at the B-site of ABO_3 perovskite structure. All the prepared samples are characterised with X-ray diffraction technique (XRD), Scanning electron microscope (SEM)/Field emission scanning electron microscope (FESEM), X-ray photoelectron spectroscopy (XPS) and RAMAN spectroscopy to extract the structure and microstructure information. The frequency dependent electrical parameters (impedance, dielectric loss, phase angle and capacitance) are collected with the help of Impedance analyser within a broad range of temperature from room temperature (RT), 25^{o}C to 450^{o}C. The temperature dependent dielectric constant is extracted from the impedance data to examine the nature of dielectric anomalies, the effect of modification on dielectric constants, Curie temperatures and dielectric losses of the compounds. The

polarisation-electric field (P-E) hysteresis loops for all the samples are collected by Radiant precision loop tracer.

The role of precipitated silver particles in $AgNbO_3$ is thoroughly and systematically investigated by complex impedance spectroscopy within frequency and temperature domain of 100Hz to 1MHz and 25 ^oC to 450 ^oC respectively. Extensive analysis over relaxation mechanisms verified that only intrinsic (grain) conduction is the major contributing source. The absence of extrinsic (interfacial) conduction indicates that the precipitated silver nano particles has no active role in the electrical properties as these are supposed to be deposited in various interfaces. In the isovalent metal oxides doping, satisfactory results in ferroelectric properties came in Sb_2O_5-doped and V_2O_5-doped systems. In the Sb_2O_5-doped system, the improved P-E loop appeared at higher applied field. MnO_2-doped $AgNbO_3$ systems are prepared successfully by retaining the phase of the parent system. Low concentration of MnO_2 was substituted in molecular weight fraction (x = 0.02, 0.04) of Nb_2O_5 to prepare the modified $AgNbO_3$ compound by solid state route, with an object to partially incorporate Mn^{4+} in place of Nb^{5+} site. The XPS results identify the presence of manganese in Mn^{4+} and Mn^{3+}state. The ferroelectric parameters were improved and results were properly discussed. WO_3-doped $AgNbO_3$ systems were successfully prepared by retaining the phase of the parent system. Low concentration of WO_3 was substituted in molecular weight fraction (x = 0.02, 0.04) of Nb_2O_5 to prepare the modified $AgNbO_3$ with an object to incorporate W^{6+} in place of Nb^{5+} to design the electron doped systems. XPS peaks identify the presence of tungsten in W^{6+} and W^{5+} state and hence confirm the possible hole doping in the modified systems. In the AWN2 system, the ferroelectric properties reduced but in AWN4 system, significant increase in the parameters was observed which were analysed with possible reasons. Transition metal oxide TiO_2 was selected to dope with the $AgNbO_3$ system in order to partially incorporate Ti^{4+} in place of Nb^{5+} cation. XPS results confirmed the presence of Ti^{4+} and Ti^{3+} state and hence the possible hole doping in the system was successful. In the TiO_2-doped systems, though ferroelectric parameters exhibited high enhanced value but the shape of the loop approaches lossy feature. Apart from this, the effect of modifications on structure, microstructure, dielectric constant, tangent loss, activation energy, resistance of the materials were accurately reported, sincerely analysed and properly discussed.

The thesis provides some qualitative information regarding the titled compound which will benefit the other researchers to go for other transition metal oxide modifications. The properties of the modified systems are also suitable to be used in capacitors and memory applications.

Keywords: ceramics; dielectric response; lead free ferroelectrics; electrochemical Impedance spectroscopy

Contents

List of Figures

List of Tables

List of Abbreviations and Notations

AN	Silver Niobate
SEM	Scanning electron microscopy
FESEM	Field emission scanning electron microscopy
XRD	X-ray diffraction
E	Applied field

E_C	Coercivity
P_r	Remnant Polarization
P_S	Saturation Polarization
Z	Impedance
Z'	Real impedance
Z"	Imaginary impedance
M	Electric modulus
M'	Real modulus
M"	Imaginary modulus
τ	Relaxation time
ε	Dielectric constant
σ	Electrical conductivity
ρ	Electrical resistivity
Tan δ	dielectric loss
T	Temperature
eV	electron volt
K	Kelvin
g	gram
Hz	Hertz
nm	nanometer
Å	angstrom
d	Inter planner spacing
ɵ	Bragg angle

Chapter 1

Introduction

Oxide materials show amazing electric and magnetic properties on which still lots of research is going on to explore the underlying fundamental science which is responsible for various phenomena [1]. Dielectric, ferroelectric, piezoelectric, electro-optic, optical, semiconducting, magnetic, giant magnetoresistance, superconducting etc. are some of the physical properties which have been highly investigated and reported since the beginning of the last century [3]. The above mentioned properties are reported to be strongly related to the structure in which the oxide material has been crystallised. Some of the structures which are more favourable for the oxide materials to crystallise are (a) Rutile structure, (b) Garnet structure, (c) Perovskite structure and (d) spinel structures. Among them, oxide materials which are crystallised in perovskite (ABO_3) structures have been studied extensively since the report of ferroelectricity in $BaTiO_3$ in 1945. Thereafter, perovskite oxide materials are reported with a range of properties such as: dielectric ($CaTiO_3$, $KTaO_3$), ferroelectric ($PbTiO_3$, $KNbO_3$), piezoelectric ($PbZr_{1-x}Ti_xO_3$), electro-optic ($Pb_{1-y}La_yZr_{1-x}Ti_xO_3$), semiconducting ($Ba_{1-x}La_xTiO_3$), Magnetic ($GdFeO_3$, $LaMnO_3$), giant magnetoresistance ($LaMnO_{3-x}$), high T_C superconductivity ($Y_{1/3}Ba_{2/3}CuO_{3-x}$) and many more. These materials promise for better and suitable application in electronics and telecommunication industries like: high energy storage capacitors, Non-volatile computer memory, microwave communication, sensors, read heads in hard disks, magnetic detectors, electrolyte in solid oxide full cells, laser etc. The simplicity in their structure and the versatility in their nature make them more attractive for unfolding the science behind different physical phenomena [1-7].

1.1 Perovskite structure

The mineral ($CaTiO_3$) was discovered by Gustav Rose in 1839 from the samples found in the Ural mountain and the structure possessed by this mineral is named as perovskite after a Russian mineralogist, Count Lev Aleksevich von Perovskite.

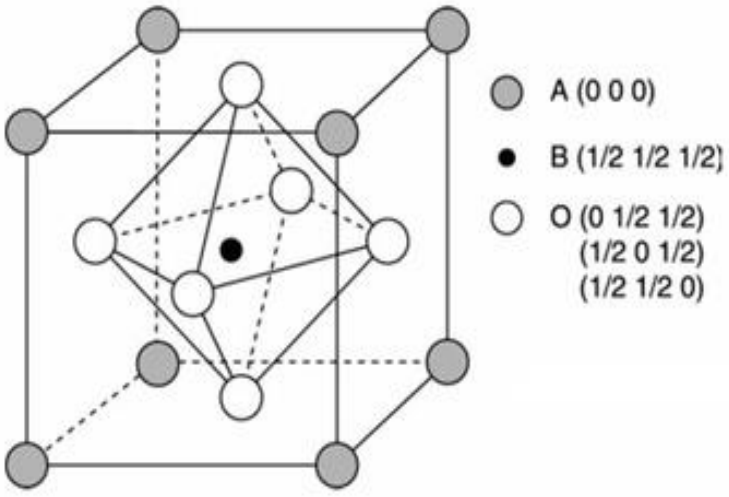

Figure 1.1: ABO_3 perovskite structure [8].

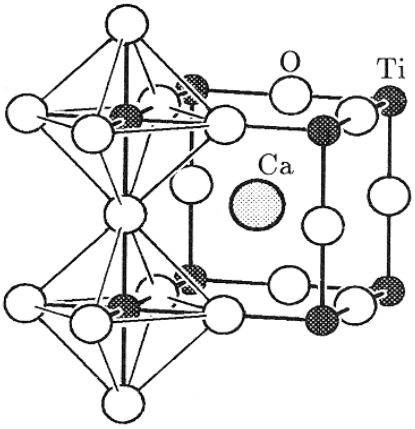

Figure 1.2: Perovskite, $CaTiO_3$ [8].

The feature of this structure is a primitive cube with formula unit ABO_3 where, 'A' is the larger cation in the corner may be a monovalent, divalent and trivalent metal, 'B' is the smaller cation at the centre of the cube may be a pentavalent, tetravalent and trivalent element respectively and Oxygen atom occupies the centre of the faces. The material which crystallised in perovskite structure can be viewed as a repetition of the formula unit ABO_3, or the repetition of a three dimensional frame work of BO_6 octahedra or the repetition of AO_{12} dodecahedra which are shown in the Figure1. It can be detected that the coordination number of cation A is 12 and for cation B is 6.

Perovskite structure also has its different manifestation such as: (a) double perovskite ($A_2BB'O_6$) or ($AA'B_2O_6$) and (b) layered perovskite which is of three types given by (i) DionJacobson($A[A'_nB_nO_{3n+1}]$),(ii)RuddlesdenPopper($A_2[An1BnO_{3n+1}][AO][ABO_3]_n$) & (iii) Aurivillius ($[BiO_2][A_{n-1}MnO_{3n+1}]$) [1-5].

1.1.1 Characteristics of Perovskite structure

(a) The structure shows a great stability which allowed variation in tolerance factor (t) that leads to little distortion in the structure without disturbing the basic framework.

(b) The cations at A and B sites can be a suitable combination of (I, V), (II, IV) and (III, III) oxidation states and hence can be considered as insensitive to the charge distributions.

(c) The structure can withstand although a considerable departure from ideal stoichiometry will occur like: (i) oxygen vacancies and (ii) A-site cation vacancies.

1.2 Dielectric and Ferroelectric Perovskite

Modern age electronic equipment is reducing its size for its easy access and communication purpose but without compromising with the efficiency and durability of the gadgets. Capacitor is a must element which takes maximum space in the electronic appliances and therefore, miniaturisation of electronic equipment means miniaturising the size of the capacitor by retaining the energy storing capacity. This drives the material scientist to design ceramics of high dielectric constant or improve the existing dielectric value of some good performer material to the required value by suitable modification. Therefore, it is very much essential to understand the underlying science for the

mechanisms of dielectric, ferroelectric and several other parameters relating to electric transport properties [9].

1.2.1 What is a dielectric?

A dielectric is a class of material that gets polarised when interacts with the external fields like electric field, magnetic field, thermal field, mechanical field, electromagnetic wave etc. Four basic polarisation mechanisms have been identified in a dielectric material: (a) electronic, (b) atomic/ionic, (c) dipolar/orientational and (d) space charge polarisation. Electronic polarisation is due to the shifting of charge centres of bound negative charge clouds of electron and positive nucleus due to the application of an electric field. A second source of polarisation is observed in molecules which are formed by atoms from different elements. The electrons displaces towards the stronger binding atoms in the absence of an electric field. But, the presence of an external field shifts the equilibrium position of the atoms which creates a dipole moment. This is known as atomic/ionic polarisation. The third kind of polarisation arises due to the asymmetric charge distribution in molecules which results in the development of permanent dipole moment. This dipole reorients according to the applied external field. This is known as dipolar/orientational polarisation. The source of the fourth type of polarisation is due to the free charge carriers which are restricted in their motion. This is known as space charge polarisation. These polarisation mechanisms are microscopic in nature which related to the macroscopic measurable parameter of the material is known as permittivity [9].

Nature occurring dielectric materials are found with very less permittivity ranges from 1 to 5 ex: air (1), amber (2.6), glass (3.8) etc. There is a significant effect of the structure of the compound on its dielectric property. Non centrosymmetric structure has a possibility of generating permanent dipole moment to give a polar behaviour to the compounds crystallised in this manner. It's not always that non-centrosymmetric structure associate with polar behaviour as rare combination of non-centrosymmetric and non-polar material also exists. Ferroelectric materials are a subclass of dielectric material which possesses non-centrosymmetric structure show unusual high permittivity near their transition (Curie) temperatures about which their polar structure changes to non-polar one [9-12].

1.2.2 What is a ferroelectric?

Ferroelectric ceramics are categorical dielectrics of single crystal or polycrystalline solids composed of crystallites which possess the peculiar reversible spontaneous polarisation i.e. they possess permanent electric dipole which reorients in responding to the changing electric field. The word spontaneous may mean that the polarization has a nonzero value in the absence of an applied electric field. The word reversible refers to the direction of the spontaneous polarization that can be reversed by an applied field in opposite direction. The most prominent features of ferroelectric properties are hysteresis and nonlinearity in the relation between the polarization (P) and the applied electric field (E). This is because there are some materials with spontaneous polarisation due to their non-symmetry and polar structure but cannot be reversed by changing the direction of the applied field. Therefore, hysteresis loop is the fingerprint of a material to be recognised as a ferroelectric material. With increase in temperature the non-centrosymmetric, polar character of the structure vanishes and stabilise with the increases free energy by adopting a centrosymmetric, non-polar structure. The temperature at which this polar phase shifts to the non-polar phase is known as Curie temperature (T_C) which associates with the structural transition from lower symmetry to higher symmetry [1-5, 9-18].

1.2.3. What causes ferroelectric distortion?

Several theories were developed with time to explain the origin of ferroelectricity with its discovery in different type of materials. Order-disorder theory was formulated for the early ferroelectric materials like Rochelle salt ($KNaC_4H_4O_6 \cdot 4H_2O$), mono potassium phosphate (KH_2PO_4) in which hydrogen bond was supposed to be the essential part in order to exhibit ferroelectricity. Then displacive transition theory was formulated to explain the ferroelectricity in perovskite oxides ($BaTiO_3$, $LiNbO_3$ etc.) in which octahedral displacement or cation displacement is an essential feature. Then with the discovery of ferroelectricity in several complex oxides, a more generalised soft phonon mode theory was conceptualised to explain its origin. But, the common feature in all the cases is that the centre of symmetry or inversion symmetry must break due to which centers of positive and negative charge clouds must shift from each other. This creates a dipole and as a result net spontaneous polarisation will develop in the unit cell. Therefore, distortion of the structure to reduce the symmetry is necessary in order to bring ferroelectric instabilities in a compound system [9-18].

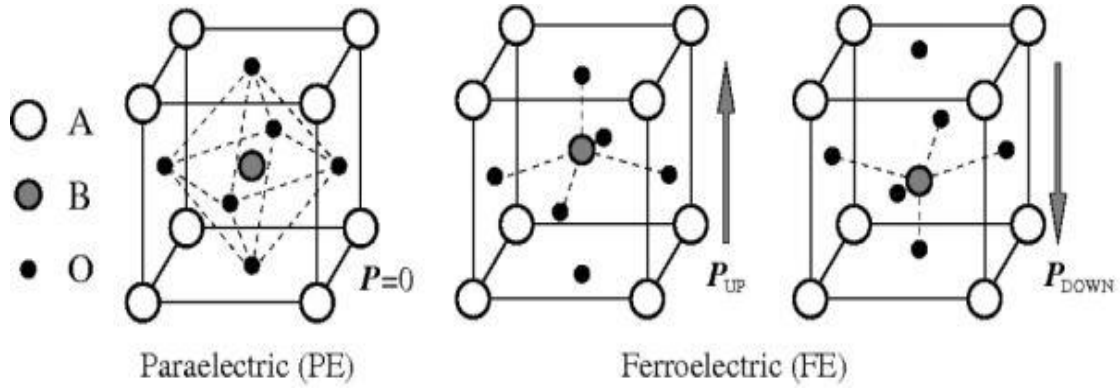

Figure 1.3: Showing the cation and anion positions in the paraelectric phase and their displacement in the ferroelectric phase [9].

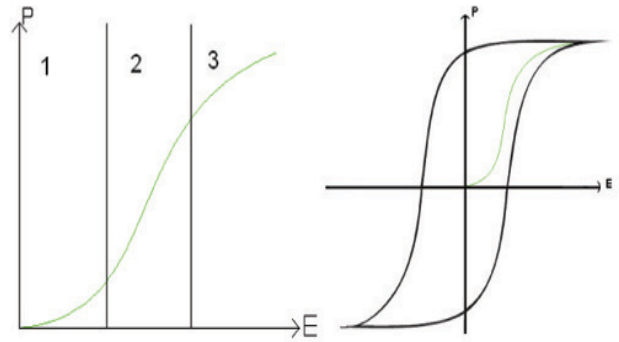

Figure 1.4: P-E hysteresis loop showing non-linear growth of polarisation vector and its reversibility [10].

1.2.4. Distortion in a perovskite structure:

In a perovskite structure distortion can be generated most favourably by three types: (i) octahedral tilting, (ii) cation/anion displacements and (iii) Jahn-Teller distortion. All these distortions are meant to bring a structure from its higher symmetry to a lower symmetry.

When the arrangement of the ions makes the system unstable at high energy then it rearranges the ions in accordingly to create a stable low energy state [1-6, 12-21].

1.2.5. Octahedral tilting/Cation displacement:

A perovskite structure can be considered as a repetition of BO_6 octahedra in a regular manner. This B-cation undergoes a strong hybridisation with the Oxygen anion and hence develops a bond of both ionic and covalent in nature. Depending upon the nature of orbit for B-cation electron exchange takes place between the anion and cation. This develops a strong coulomb interaction and increases the energy of the system. In order to reduce the excess energy the B-cation slightly displaces from the center of the octahedra. Due to this asymmetry in different B-O bond length occurs and symmetry lowers [22-27].

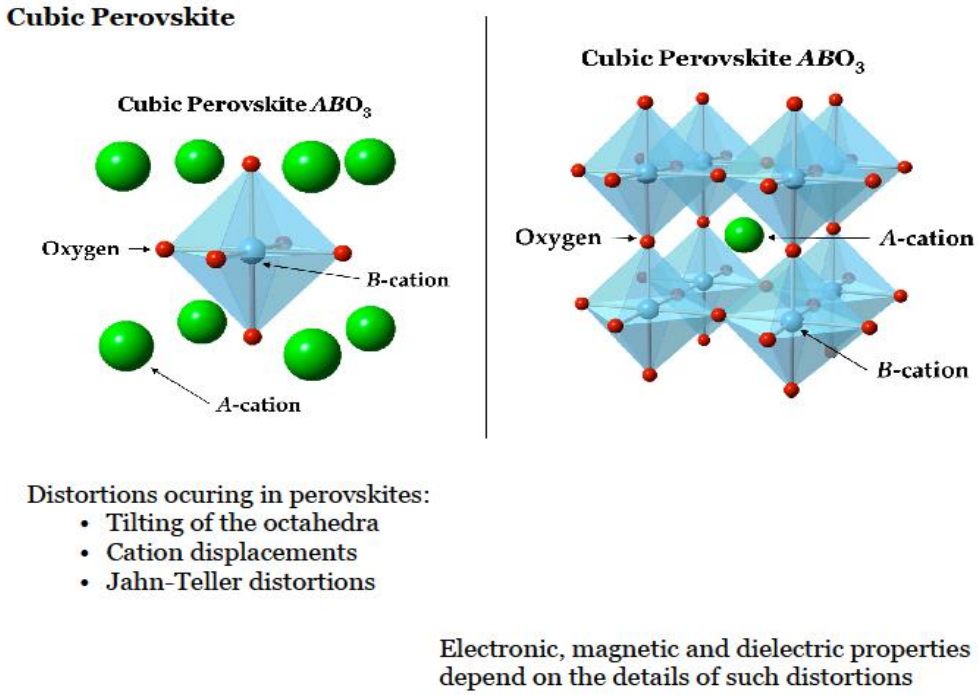

Figure 1.5: Cations position in cubic perovskite [11].

The oxygen octahedra as a basic unit are seen to be tilted or rotated form in some of the materials crystallised in perovskite structures. The tilting or rotation of these BO_6 octahedra in particular crystals is explained in terms of a mathematical tool known as tolerance factor.

1.2.6. Tolerance factor

The tolerance factor is proposed by Goldschmidt in 1923 which is number that provides a provisional idea about the stability of perovskite structure. Mathematically, it is given by, $t = (r_A + r_O)/\sqrt{2}(r_B + r_O)$,where, r_A – ionic radius of A cation, r_B – ionic radius of B cation and r_O – ionic radius of oxygen anion [28-29].

For ideal cubic perovskite t = 1, in which the size of A- cation matches approximately to O- anion to form a perfect closed cubic structure and the size of the B- cation matches to the interstitial space of oxygen's to form BO_6 octahedra, ex: $SrTiO_3$. For mismatch of the size of the anion and cations, the tolerance factor may take the value either $t < 1$ or $t > 1$ ex: $CaTiO_3$ or $BaTiO_3$ respectively. This leads to tilting or rotation of BO_6 octahedra in

order to occupy the available volume for A- cation which lowers the symmetry of the system by assuming hexagonal, tetragonal, rhombohedra or orthorhombic structure though basic framework remains intact. This mechanism associated with displacement of B cation which may exhibits ferroelectric distortion [1-3, 13-29].

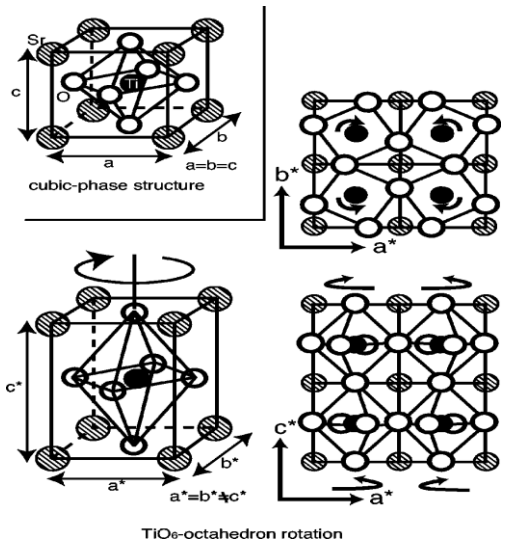

Figure1.6: Showing octahedral rotation and the cation displacement [32].

1.2.7. Perovskite structure containing d^0 transition metal

It is observed that the d-orbital energy is very sensitive to distortion and covalency which mostly affects octahedral rotation. It is calculated that when a d^0 transition metal will occupy the octahedral site the Jahn–Teller distortion further favours after crystal field splitting. Due to the existence small energy gap between the HOMO (valence band) and LUMO (conduction band) symmetry distortion occur which is known as Jahn-Teller distortion of second order in order to stabilise HOMO and destabilise LUMO. As an effect, it reduces the crystal symmetry and widens the energy band gap [3, 22-25]. It is observed that for the high valent d^0 cations like Ti^{4+}, Nb^{5+},W^{6+} etc. when occupies the octahedral centre, it favours the decreasing HOMO-LUMO splitting and increases the Cation–Oxygen bonding. Again, for the cations of filled valent 's' orbit like Pb^{2+}, Bi^{3+}, Sb^{3+}, Sn^{2+} etc., the second order Jahn-Teller distortion leads to a stereoactive electron lone pair [30-31].

Due to this distortion, the d^0 cation displaces from its centre which mismatches the anionic and cation centre. This leads to the generation of a dipole and polarisation within a unit cell. The ordering of the displaced cation in the perovskite structure depends upon the valence requirements of the anion and cation – cation repulsion. The spectacular properties shown by such d^0 transition metal perovskites are: dielectric, piezoelectric, ferroelectric and insulating etc. [1-3, 30].

The stabilisation of the HOMO will disappear as soon as the d–orbital starts occupying electrons. The spin–spin interaction of unpaired electrons in the d–orbitals develops in addition to charge – charge interaction which gives rise to magnetic behaviour. This interaction may be direct or indirect through overlapped oxygen orbital. Such perovskite material exhibits both electric as well magnetic properties which combination ranges from (insulating, diamagnetic), (metallic Pauli magnetism), (semiconductor,

antiferromagnetism), (colossal magnetoresistance, antiferromagnetism) (metallic, spiral antiferromagnetism) etc. [2, 3, 30, 31].

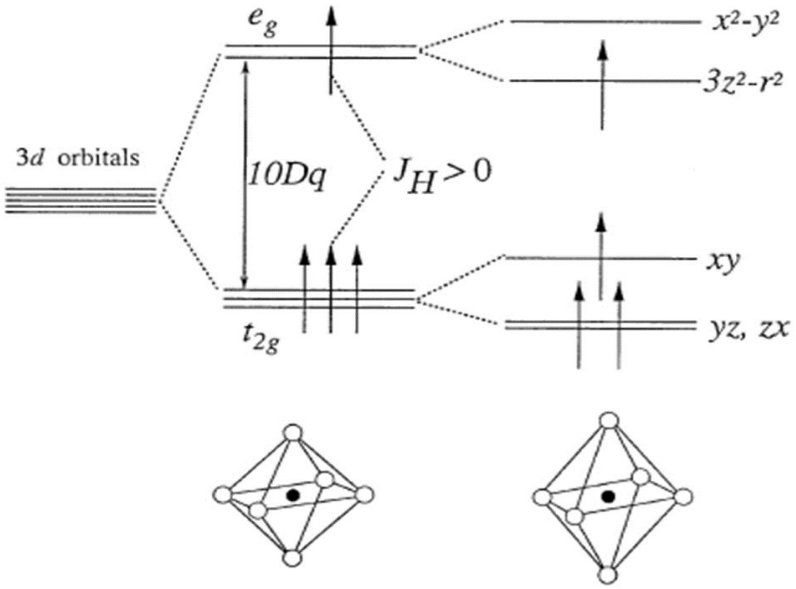

Figure 1.7: Cation orbital splitting due to crystal field effect and Jahn-Teller distortion [11].

1.2.8. Jahn – Teller transition of the second order:

In an electronically degenerate state, if the orbitals are asymmetrically occupied then the energy of the system will be increased. This forces the system to lower its symmetry in order to get rid of the excess energy which leads towards distortion and is known as Jahn-Teller distortion as per the due who proposed and explain this mechanism. This distortion lifts the degeneracy of the system [32]. Unlike other distortions, the off-centering of cations is of less probability in Jahn-Teller type. It is observed that the population of electrons in t_{2g} states also affects the octahedral rotation. The higher the population in the t_{2g} state or the low spin state experiences less octahedral rotation. The high spin configuration associates with larger octahedral rotation and hence blocks the cation displacement [32-34].

The ferroelectric hysteresis loop finds its application in data storage. At Curie point, a small electric field can generate a large polarisation which can concentrate electric flux density and results high dielectric constant. This can be used in capacitor for high energy storage. In ferroelectric materials, change in electric polarisation also accompanies with change in shape and hence can be used as electromechanical transducers and actuators. Ferroelectric thin films is now an attracting field of interest for the application of non-volatile computer application as the current static and dynamic memory chips lose data which they contain as soon as the power supplied to the memory chips is interrupted and is not retrievable. Another application currently under investigation is the use of ferroelectric materials as electro optic switching devices for optical computers. This idea is based upon the ability of a ferroelectric material to change its refractive index under an applied field.

Uchida et al. investigated the effect of charge carrier doping by theoretically and matched with the previous experimental result for confirmation. In their report, "First-principles calculations of carrier-doping effects in $SrTiO_3$" they explained the ferroelectric instabilities after the doping of charge carriers (electron/hole) by photoinduced method. It

is theoretically calculated and investigated that due to the charge carrier doping the ionic radii of the constituent elements varies and hence also the tolerance factor. From the first principle calculation it is observed that the conduction band mostly consists the d-orbital of the B-cation centred at oxygen octahedra and valence band consists the 2p orbital of the oxygen anion. When electron as a charge carrier is doped into a system it occupies the orbital of the B-cation and hence increases its effective radii. This lowers the tolerance factor and promotes octahedral rotation. When a hole is doped into a system it occupies the orbital of the oxygen and if (r_A- r_B) is positive then net tolerance factor increases. This suppresses the octahedral rotation [35].

Wang et al. reported "Ferroelectric Instability under Screened Coulomb Interactions" in which they explained that the ferroelectric instability in a system requires only a short-range portion of the Coulomb force with an interaction range of the order of the lattice constant. The doping of electrons screens the long range coulomb interaction and at a critical charge carrier density the ferroelectric instability vanishes due to the domination of short range repulsive force over the coulomb interaction [36].

Till date, materials crystallised with perovskite structure possessing ferroelectric property has been rigorously investigated and reported by a large numbers. Perovskite titanates particularly $BaTiO_3$ opens the window for investigation to search the origin of ferroelectricity first time without any hydrogen bond, which was supposed to be the essential parameter for earlier natural occurring ferroelectric materials. Perovskite niobates like $LiNbO_3$, $KNbO_3$ were discovered with ferroelectric nature. But, the superior properties were found in $PbTiO_3$ and its modified systems. Perovskite niobates such as $LiNbO_3$, $KNbO_3$ etc. were discovered with their ferroelectricity in 1949 also provide an equal opportunity to investigate them to unravel the mystery of ferroelectricity in parallel with the titanates and keeps enormous importance as electro-ceramics for electronics and engineering. But, the most versatile one is the lead zirconium titanate (PZT) as well as the other lead based ceramics which exhibit extremely good properties which dominate in its application as smart materials. But, the toxic nature of lead is not proper and suitable for large scale consumption as it deteriorate the quality of soil, water and air which threatens the safety and tranquillity of environment and nature. There is a huge uproar worldwide to reduce the use of lead (Pb) which dominates in its application as smart materials. Hence, material scientists have shifted their focus to develop lead free ferroelectric materials with comparable functional properties [1, 7, 12].

Among the several classes of lead free ferroelectric material, perovskite niobates like $LiNbO_3$ (LN), $KNbO_3$ (KN), $NaNbO_3$ (NN) and their solid solutions like KLN, KNN, and LNN are also investigated in large scale. These perovskite niobates also contains $5d^0$ (Nb^{5+}) at their octahedral cage which is supposed to be an essential feature to be good ferroelectric material. These ferroelectric niobates with their large spontaneous polarisation are becoming promising materials for laser technologies, holographic techniques, integrated optics, surface acoustic wave devices and high frequency telecommunication signal processing techniques.

Silver niobate ($AgNbO_3$) also crystallised in perovskite structure of $Pmc2_1$ symmetry at room temperature. Ag^{1+} with its effective ionic radius of 1.28Å at A-site of eight coordination numbers and Nb^{5+} with its effective ionic radii of 0.69Å at B-site of six coordination numbers within ABO_3 formula unit assume a distorted perovskite unit due to its low tolerance factor of 0.956. The room temperature polarisation versus electric field (P-E) loop is very slim giving an impression of antiferroelectric order, shown in Fig. 1.9.

But, the presence of small remnant polarisation (P_r ~0.046 μC/cm^2) draws argument in favour of weak ferroelectricity. This material came into limelight with the discovery of an extreme large spontaneous polarisation (52μC/cm^2) in its polycrystalline form at sufficient high field (220kV/cm). This value is higher than the polycrystalline $PbTiO_3$ (~ 50μC/cm^2) and single crystal of $BaTiO_3$ (26μC/cm^2) and also from the polarisation values of all polycrystalline perovskite niobates. This attracts to choose this material for the research programme [12, 49].

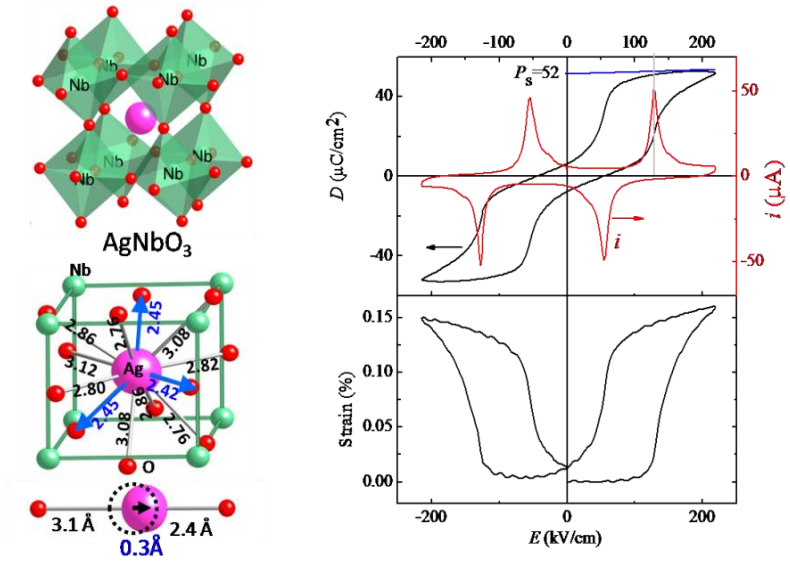

Figure 1.8: Showing Ag cation in the AgO_{12} cage, off-centering of Ag, P-E loop and butterfly strain loop [49, 76].

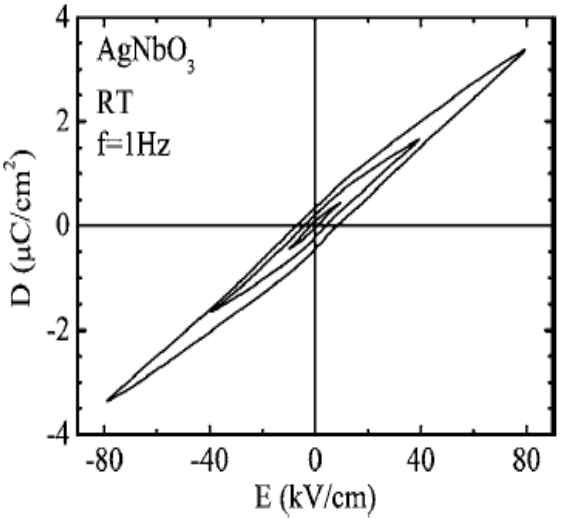

Figure 1.9: P-E loop at room temperature [49].

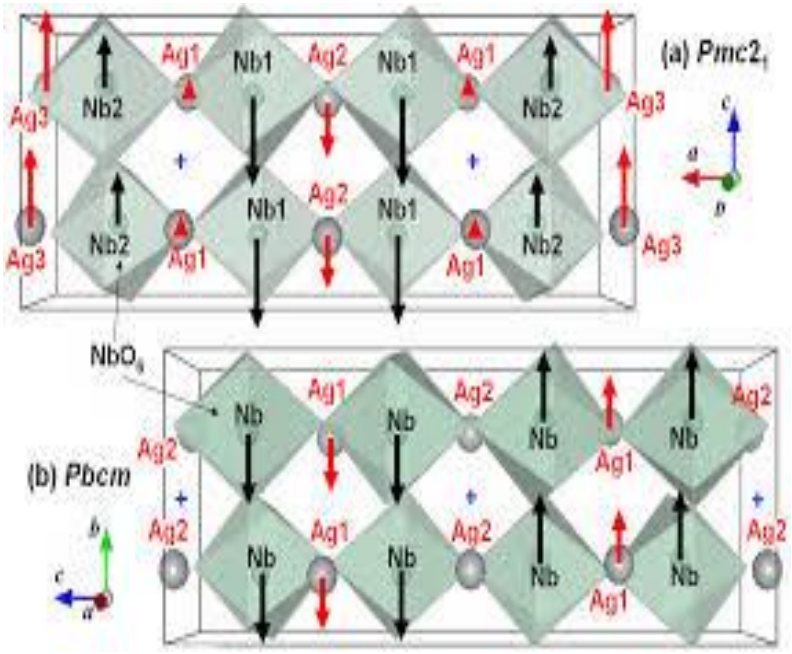

Figure 1.10: The atomic displacements along the *c*-axis lead to the spontaneous polarization in the crystal. (b) For comparison, the patterns for the previously reported *Pbcm* (Sciau et al., 2004) are also given. A cross (+) stands for the center of symmetry in the *Pbcm* structure (Yashima et al., 2011) [57].

1.3 Brief discussion about the literatures on Perovskite$AgNbO_3$.

Silver Niobate ($AgNbO_3$) was first discovered by Francombe and Lewis in 1958. Since then, several research groups have been working on this material to explain the basic mechanism related to the multiple dielectric anomalies in temperature dependent permittivity plot, weak ferroelectricity, structural transformations etc. and reported the results in various journals of repute. Some of the groups whose works are very vital in understanding the intrinsic behaviour of the materials are listed as: Nalbandyan et al. 1980; Lukaszewski et al. 1983; Kania, 1983, 1998; Kania et al. 1984, 1986; Pisarski&Dmytrow 1987; Paweczyk 1987; Verweft et al. 1989; Hafid et al. 1992; Volkov et al. 1995; Fortin et al. 1996; Petzelt et al. 1999; Valant et al. 1999 (I & II); Ratuszna et al. 2003; Grinberg et al. 2004; Sciau et al., 2004; Saito et al. 2005; Fu et al.2007, 2008(a, b); Levin et al. 2009, 2010; Yashima et al. 2011; Miga et al. 2011; Chang et al 2012; Niranjan et al., 2012 etc.

1.3.1. Synthesis of $AgNbO_3$ system:

Silver niobate can be prepared by conventional solid state route by taking Ag_2O and Nb_2O_5 as raw precursors. This method is mostly approached by the researchers due to the easy availability of metal oxides and is particularly niobium oxide. For chemical route, water/acid soluble metal nitrates are required and preparing niobium nitrate salt is impossible. Still niobium oxalates ($C_{10}H_5NbO_{20}\cdot 6H_2O$) are used to prepare the compound by chemical method. Silver faces volatility problem and hence to maintain stoichiometry calculated extra (3wt %) silver oxide is added. Presence of negligibly minute secondary phases continues to present along with the $AgNbO_3$ phase irrespective to the synthesis process and condition of preparing. Metallic silver precipitates during high temperature processing like calcination and sintering and is easily introduced in solid state synthesis route. This is confirmed from the high resolution transmission electron microscopy (HRTEM), X-ray photoelectron spectroscopy (XPS) etc. [39-41].

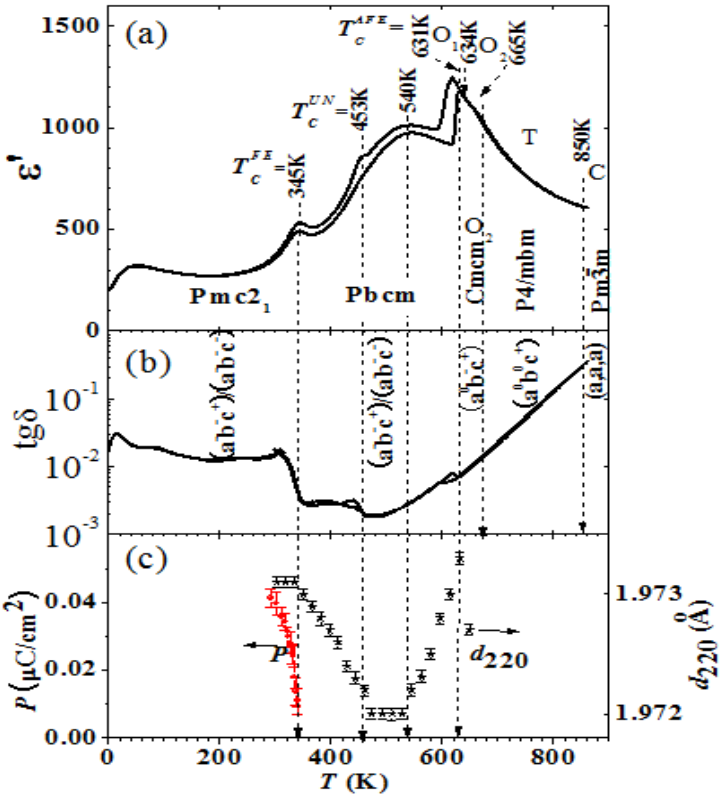

Figure 1.11: Temperature dependence of (a) dielectric constant, (b) dielectric loss, and (c) polarization (Kania et al., 1984) and 220_0 *d*-spacing of the lattice (Levin et al., 2009) [49].

1.3.2. Temperature dependent relative permittivity study of $AgNbO_3$ system:

Six successive dielectric anomalies appear in the temperature dependent relative permittivity {ε(T)}of $AgNbO_3$ compound in a wide range of temperature, shown in Fig. 1.11. Each dielectric anomaly is associated with particular structural transformation that brings several phase transitions. These anomalies are assigned as M_1, M_2, M_3, O_1, O_2, T, and C: at 67 ^oC– from orthorhombic M_1 to the orthorhombic M_2, at 260 ^oC–from orthorhombic M_2 to the orthorhombic M_3, at 350 ^oC– from orthorhombic M_3 to the orthorhombic O_1, 364 ^oC– from orthorhombic O_1 to the orthorhombic O_2, 387 ^oC – from orthorhombic O_2 to the tetragonal T, 579 ^oC–from tetragonal T to the cubic C phase [39-49]. The low temperature dielectric anomaly $M_1 \leftrightarrow M_2$ is of relaxor nature, $M_2 \leftrightarrow M_3$ is a broad phase transition and $M_3 \leftrightarrow O_1$ is a sharp phase transition. The dielectric loss also shows related peaks at corresponding temperatures. Recently, *Zhang et al.* reported the appearance of a phase transition in ε (T) at sufficient low temperature ~ 250K (-23^oC) and they assigned it as M_0 phase [46]. *Kania et al.* reported that the $M_1 \leftrightarrow M_2$ phase transition depends upon the concentration of the Ag^{1+} cation. The shifting of sharp phase transition and low temperature dielectric anomaly in a modified system of $AgNbO_3$ depends upon the nature of dopants as in Lithium (Li^{1+}) modified system the sharp ($M_3 \leftrightarrow O_1$) transition shifts to higher temperature and $M_1 \leftrightarrow M_2$ transition shifts towards lower temperature [56]. However, in potassium (K^{1+}) modified system all the transition points shift towards lower temperature. The nature of each phase, structure and the related cation dynamics have been rigorously investigated through theoretical first principle method as well as several experimental techniques and the most important are discussed below.

1.3.3. Ferroelectric study of $AgNbO_3$ system:

A narrow slim polarisation vs. electric field (P-E) loop appears at room temperature (RT). A very small value of remnant polarisation ($0.041\mu C/cm^2$ at~11kV/cm, $0.095\mu C/cm^2$ at 2.95kV/cm) is found in the polycrystalline and single crystal of $AgNbO_3$ respectively, shown in Fig. 1.9[47, 48]. The debate over its nature whether antiferroelectricity or ferroelectricity was continued a long time. This came to an end with the acceptance of the weak ferroelectricity at RT. Fu *et al.* reported a large spontaneous polarisation $52\mu C/cm^2$ in its polycrystalline form but at sufficient high field of 220kV/cm, shown in Fig. 1.8(b) [50]. The narrow shape of P-E loop continues with increasing field and suddenly evolves to saturate to $52\mu C/cm^2$ at 220kV/cm. This discovery confirms that the $AgNbO_3$ is a potentially ferroelectric material in nature. The temperature dependent ferroelectric study of the compound confirms that M_1 phase is ferroelectric nature, M_2 & M_3 are antiferroelectric whereas O, T & C-phases are paraelectric nature [47, 48].

1.3.4. Structural study of $AgNbO_3$ system:

Ratuszna et al., Weirauch et al., M. Pawelczyk and *Verweft et al.* at first suggested that like $NaNbO_3$, the phase transitions of $AgNbO_3$ are associated with two basic mechanisms of phase transitions i.e. octahedral tilting and cation displacements. The high temperature paraelectric phase transitions between O_1, O_2, T and C are mostly due to the octahedral tilting. Down to room temperature, the phase transitions from O_1 to M_3 polymorphs is due to octahedral tilting and the Nb^{5+} cation displacement from the center of the NbO_6 octahedra. This off-centering of Nb^{5+} cation forms dipole and hence the antiferroelectric orders in the M-polymorphs [50-53].

X-ray photoelectron spectroscopy study by *Kruczek et al.* also supported the covalent characters of the chemical bonds between Ag and O as well as Nb and O ions. This result also supported by the report of *Fu et al.* in which bond-length analysis was theoretically predicted. It is found that the bond length of Ag-O is ~2.43 Å in the structure which is significantly smaller than the sum of Ag^+ (1.28 Å) and O^{2-} (1.40 Å) ionic radii [54].

It was after the advancement of the first-principles calculations as well as modern techniques of synchrotron radiation it is revealed that chemical bonding in the perovskite oxides is not purely ionic as it was supposed rather it possesses covalent character which plays a crucial role in the occurrence of ferroelectricity in the perovskite oxides. Theoretical investigations by *Grinberg et al.* and *Shigemi et al.* suggest that a strong hybridization exists between Ag and O due to which a large off-center of Ag at the A-site of perovskite $AgNbO_3$ compound is observed like Pb ion in lead based materials. But, the excess NbO_6 octahedral rotation of ~ 14.5^o occupies the available space for Ag^{1+} cation within AgO_{12} chamber. This blocks the proper off-centering of Ag^{1+} cation and results poor polarisation at low applied field [55, 56].

Sciau et al. in their report, "structural investigation of $AgNbO_3$ phases using X-ray and neutron diffraction" confirmed the existence of sequence of phase transitions. They successfully revealed the essential structural changes related to the $M_3 \leftrightarrow O_1$, $O_2 \leftrightarrow T$ and $T \leftrightarrow C$ phases but failed to provide much information about $M_1 \leftrightarrow M_2$ and $M_2 \leftrightarrow M_3$ phases. They postulated the co-existence of ordered and disordered subsystems in $AgNbO_3$: the ordered system leads to sharp ($M_3 \leftrightarrow O_1$) phase transition and the disordered system leads to broad ($M_2 \leftrightarrow M_3$) phase transitions. All the M–phases have orthorhombic symmetry

with rhombic orientation and lattice parameters whereas O-phase acquires orthorhombic symmetry (Cmcm) with parallel orientation, T– phase has P4/mbm symmetry and C–phase has Pm3m symmetry, shown in Fig. 1.11. Octahedral tilting is found responsible for high temperature transitions such as O↔T and T↔C phase whereas M phase transitions are ascribed to cation displacements. Their study revealed that a strong structural disorder dominates in the paraelectric O and T phases due to the NbO_6 octahedral tilting whereas the low temperature non-paraelectric distortions are dominated by Ag^{1+} and Nb^{5+} cation displacements [57].

Levin et al. investigated the structural changes underlying the diffuse dielectric response in $AgNbO_3$, using high resolution x-ray diffraction, neutron total scattering, electron diffraction and x-ray absorption fine structure measurement. They reported the Pbcm space group in which all the M-polymorphs are crystallised having lattice parameters$\sqrt{2}a_c\times\sqrt{2}a_c\times4a_c$, where a_c=4Å corresponds to the lattice parameters of ideal cubic perovskite. Their results confirmed the existence of a complicated coupling between octahedral tilting and local displacements of both Ag^{1+} and Nb^{5+} ion sub lattice. The coupling becomes stronger at low temperature dielectric anomaly ($M_1\leftrightarrow M_2$) which associated with a large NbO_6 octahedral tilting [58].

Yashima et al. in their report of "structure of ferroelectric silver niobate $AgNbO_3$" is to a large extent clarified some of the phenomenal problem. They used convergent-beam electron diffraction, electron diffraction, the neutron and synchrotron powder diffraction and first principle calculations to properly investigate the room temperature polar character. They found the rarest case of ferrielectric ordering of the lattice dipoles in $AgNbO_3$ systems and first time suggested the non-centrosymmetric $Pmc2_1$ space group to explain the polar M_1 phase. They explained the net polarisation in $AgNbO_3$ in polar M_1 phase is essentially due to cations displacements along the c-axis by lowering to $Pmc2_1$ non-centrosymmetric space group from Pbcm M_2 phase [59].

Niranjan et al. recently reported titled "First principle study of lead free piezoelectric AgNbO3 and $Ag_{1-x}K_xNbO_3$ solid solution". They suggested the coexistence of both non-centrosymmetric ($Pmc2_1$) and centrosymmetric (Pbcm) phases and therefore ferroelectric and antiferroelectric order at room temperature. The spontaneous polarisation in the $AgNbO_3$ system is enhanced due to the suppression of NbO_6 octahedral tilting due to potassium (K^{1+}) substitution of larger ionic radii which increases the tolerance factor [60].

While From all the above structural investigations, it is verified that both the displacive transition which accompanies with tilting of NbO_6 octahedra and the displacement of Ag^{1+}, Nb^{5+} cations are responsible for the phase transitions in $AgNbO_3$ compound. The excess octahedral rotation forces the cations in ferrielectric/antiferroelectric order and blocks the proper off-centering of Ag^{1+} cation [50-61].

1.3.5. High frequency dielectric spectra study of $AgNbO_3$ system:

Kugel et al., Hafid et al. and *Fortin et al.* studied the high frequency dielectric spectra by measuring the permittivity at radio wave, microwave, submillimeter wave and infrared regions for a $AgNbO_3$-$AgTaO_3$ mixed systems. They identified that a relaxation mode which is associated with the Nb^{5+} dynamics and that exists in the submillimeter range which is responsible for diffuse peak of dielectric constant observed in the vicinity of the $M_2\leftrightarrow M_3$ transition. The temperature dependence of the low frequency dielectric permittivity is related to the presence of this relaxation mode at high frequency range [62-64].

Volkov et al., Petzelt et al., reported that for non-ferroelectric phases, a negligible dielectric dispersion is observed with a broad frequency range from 1 kHz ~ 100MHz. Dispersion observed in the submillimeter region is related with one relaxation mode [65, 66].

Miga et al. studied the linear and nonlinear dielectric parameters in M-polymorphs of $AgNbO_3$ ceramics as well as single crystal. They reported that the linear dielectric response is dominated by the submillimeter relaxation mode related to the Nb^{5+} dynamics at ($M_2 \leftrightarrow M_3$). The non-linear dielectric response at lower temperature is due to the freezing of both Ag^{1+} and Nb^{5+} which led to polar weak relaxor ferroelectricity. The polar M_1 phase is moreover a glassy dipolar state arise due to the frustration of inter competition between antipolar and polar states [67].

The strength, relaxation frequency and temperature of its appearance depend strongly on Nb/Ta ratio and this phenomenon is particularly observed in pure $AgNbO_3$ ceramic. These studies also confirmed that the attractive high dielectric constant derives its origin from the contribution of the submillimeter relaxation mode to dielectric susceptibility [62-67].

1.3.6. Modifications on the $AgNbO_3$ systems:

Several modifications are carried out on the AgNbO3 system to enhance its electrical properties basically weak ferroelectricity at low applied field. Most of the modifications are carried out by monovalent alkali elements (Li, Na, K) by substituting in place of Ag^{1+} cation, at A-site of the ABO_3 perovskite structure and mostly these are carried out by *Kania et al.* and *Fu et al.* The most successful results appear in the Li-modified $AgNbO_3$ system with enhance ferroelectric parameters, large electromechanical coupling factor as well as improved dielectric values and hence numbers of published works by several other groups also based on Li-modified system [68-76].

Hu et al. also modified the Ag^{1+}-site by substituting with bismuth (Bi^{3+}) and mostly focus on the phase transitions and dielectric properties of the modified systems. They reported that with the increase in the content of bismuth the temperature stable dielectric constant in the vicinity of $M_2 \leftrightarrow M_3$ phase transition [77].

The B (Nb)-site is largely modified by substituting with tantalum (Ta^{5+}) which emerged as an excellent microwave dielectric material. $AgTa_xNb_{1-x}O_3$ solid solution shows a rare combination of high dielectric constants with moderate dielectric losses in a wide range of temperature. *Valant et al.* have reported high permittivity ($\varepsilon = 375 - 414$), high quality factor ($Q \times f = 711GHz - 860GHz$, $-40^oC \leq T \leq 60^oC$) in the $AgNb_{1-x}Ta_xO_3$ ($0.46 \leq x \leq 0.6$), system which created hope on silver niobate ($AgNbO_3$) as a parent material for microwave applications [82-86]. Most of the high frequency dielectric spectroscopic studies have been carried on the $AgNbO_3$-$AgTaO_3$ solid solution system to understand the physical mechanism of the broad phase transition ($M_2 \leftrightarrow M_3$). It is reported that the increase in Ta concentration lowers the temperature for $M_2 \leftrightarrow M_3$ phase transition [78-86].

Khan et al and Guo et al. modified the $AgNbO_3$ system by combined substituting with Li^{1+} at Ag^{1+}-site and Ta^{5+} at Nb^{5+}-site. They mostly observed the phase transitions during M-polymorphs and reported the convergence of M_1, M_2 and M_3 transitions into a single broad frequency dependent maximum with increasing content of lithium [87, 88].

Some progress also proceeded in fabricating the thin film of the $AgNbO_3$ on different substrates. The substrate also found in controlling the ferroelectric, piezoelectric and dielectric properties of the compound. Better ferroelectric properties are observed in the $AgNbO_3$ thin film grown on $SrTiO_3$ substrate [89, 91].

Silver niobate also shows good photocatalytic property at visible range. This is due to the acceptable band gap and the presence of metallic silver that precipitates during high temperature thermal processing of calcination and sintering. Lots of modifications are carried out on this compound to improve its efficiency [92-95].

1.4. Motivation of Thesis

Reviewing the above literatures it is concluded that silver niobate is a versatile material having a wide range of applications ranging from high frequency capacitors, dielectric resonators, phase shifters, transducers, and actuators to suitable material for photovoltaic and visible range photocatalyst. The poor polarisation at low applied field is not an attractive figure to use it in ferroelectric memory applications. According to literatures, there exists a strong structural similarity of $AgNbO_3$ with the Pb-based compounds such as: (i) a strong hybridisation between Pb-O as well as Ag-O, (ii) both A (Pb, Ag)- and B-(Nb, transition metal ion) site cation off-centering are present, (iii) a high value of A-site distortion for both i.e. Pb (~0.05Å) and Ag (~0.03Å) and (iv) a strong coupling with the external applied field. These features of the Pb-based materials are the key factors for their superior ferroelectric property. But, disappointed 0.046 $\mu C/cm^2$ value of polarisation is observed at low applied field is not acceptable to satisfy the above structural features. However, the material recovers suddenly to an extreme large spontaneous polarisation to attain saturation ($52\mu C/cm^2$) at a sufficient high field of 220kV/cm, which is even higher than the spontaneous polarisation of polycrystalline $PbTiO_3$ (~ $50\mu C/cm^2$) and single crystal BaTiO3 ($26\mu C/cm^2$). This indicates that the material has the potential to be a good lead free ferroelectric material. Whereas, the unacceptable low polarisation value at low applied field must be related to the intrinsic complicated NbO_6 octahedral rotation and cations (Ag^{1+}, Nb^{5+}) dynamics. From the above systematic and efficient discussion on structural investigations it is established that $AgNbO_3$ system undergoes NbO_6 octahedral tilting in its high temperature (O, T and C) phase transitions. During lowering of temperature (M_3, M_2, M_1) this octahedral tilting associate with its rotation too to largely distort the structure of unit cell. This distortion also develops a complex coupling of cations (Ag^{1+}, Nb^{5+}) movement and ordering in the respective sub lattice of these cations. It is calculated that the excess octahedral rotation (~14.5^o) occupies the available space for Ag^{1+} cation and hence suppresses the proper polarisation. Though, structural distortion is an essential part in perovskite niobates/titanates to bring ferroelectric property within them but in silver niobate ($AgNbO_3$) excess distortion due to large octahedral rotation is the hurdle of being a good ferroelectric material. It is stressed that though structural and electrical studies showed that M_1 phase in principle antiferroelectric but ferroelectric properties can be appeared as a result of slight modification of this state. The appearance of the multiple dielectric anomalies in the ε (T) and their shifting according to the nature of dopants can be studied to bring the broad $M_2 \leftrightarrow M_3$ transition near the room temperature. This will help in designing a temperature stable high dielectric constant system like $AgTa_{1-x}Nb_xO_3$ system. The metallic silver particle that precipitates during synthesis and densification process has been traced in HRTEM, XPS etc. Apart from this, metallic silver nano particles precipitate during high temperature processing like calcination or sintering of $AgNbO_3$ ceramic. The role of the precipitated particles in the electrical properties of the compound is doubtful and has not been properly addressed.

1.5. Objective of Thesis:

Therefore, in this thesis it is targeted to improve the ferroelectric parameters by taking suitable measures which has the ability to reduce distortion. The selective measures are: (i) to increase the tolerance factor by substituting with suitable dopants, (ii) by charge carrier (hole/electron) doping and (iii) By incorporating the Jahn-Teller active cations at the octahedral site.

Considering the above measures for improving ferroelectric properties the suitable dopants are chosen by judging their ionic radii, electronegativity, oxidation states and potential to be Jahn-Teller active. In order to create the charge carriers we have chosen impurity doping method in which a foreign element of different valence (alieovalent) is to be substituted in place of a selected cation site. In the photoinduced method, charge carriers are created by photon energy without creating lattice distortion. But in impurity doping method the parameters of the dopant such as ionic radii, oxidation states, electronegativity, external orbital, nature of defects like vacancy or interstitial ions etc. will influence the electrical properties. Apart from this, also effect of isovalent dopant is studied. From the literatures, it is summarised that the dynamics of Nb cation is very crucial in bringing the multiphase transitions in $AgNbO_3$ as well as ferroelectric orders. Therefore, in this work we have modified the B (Nb) site within the NbO_6 octahedra of the ABO_3 perovskite. Low molar percentage doping is preferred to retain the identity of $AgNbO_3$ phase. The isovalent dopants (V_2O_5, Ta_2O_5 and Sb_2O_5) and alieovalent dopants (MnO_2, WO_3, TiO_2) are chosen to substitute Nb_2O_5 in molar fraction to bring necessary modifications. The overall objective is summarised as:

(i) To prepare the samples of bulk $AgNbO_3$ and its modified systems through conventional solid state route.

(ii) To characterize with X-ray diffraction (XRD), field emission scanning electron microscopy (FESEM)/scanning electron microscopy (SEM), X-ray photoelectron spectroscopy (XPS) and RAMAN spectroscopy to extract the structure and microstructure information.

(iii) To evaluate electrical properties by Impedance spectroscopic technique.

(iv) To evaluate polarisation vs. electric field (P-E) hysteresis loop.

(v) To examine the enhancement/deterioration of electrical properties due to modifications.

(vi) To correlate the structural and microstructural changes with the obtained results.

(vii) To correlate the parameters of dopants that influenced the results of the modified systems.

(viii) Overall, to investigate the underlying science that affects the dielectric, ferroelectric and other electric properties of the material to increase more fundamental understandings.

(ix) To sort out the role of the metallic silver particle on electrical properties through complex impedance spectroscopy.

Chapter 2

Experimental methodology

2.1. Introduction

This chapter contains the procedure for material preparation, experimental and characterization techniques. The collected data are properly analyzed and are presented in this thesis. All the experimental works are planned and executed in consultation with the supervisors' in order to get more reliable data and analysis which can be contributed to the fundamental physics throughout this work. The $AgNbO_3$ ceramic and its modified systems are prepared by solid state synthesis route. Analytical techniques like X-ray Diffraction (XRD), Raman spectroscopy, X-ray Photoelectron Spectroscopy (XPS), Scanning Electron Microscopy (SEM), Field Emission Scanning Electron Microscopy (FESEM) are used for phase confirmation and structural analysis, examining existing oxidation states of elements in the compounds and surface morphology of the prepared samples etc. Dielectric and ferroelectric properties are studied by Impedance analyzer and P-E loop tracer [96-105].

2.2. Samples preparation

$AgNbO_3$ is prepared by following the solid state synthesis route. Solid state method is one of the oldest synthesis techniques which is used to prepare the polycrystalline materials. In this method the powder is usually prepared from the raw mineral oxides or carbonates by crushing, grinding and milling. There are the various steps for the preparation of $AgNbO_3$ sample which involve solid state route are shown in the flow chart. The various steps involved in solid state method to prepare the $AgNbO_3$ are shown in the flow chart. Ag_2O and Nb_2O_5 are mixed in a stoichiometry proportions and grinded for 2 hours using agate mortar. The mixed powder was calcined at required temperature. Then the calcined powder was compacted or pelletized using uniaxial press using tungsten carbide die and finally the samples are subjected for sintering. A detail about calcination and sintering temperature is given in the respected chapters.

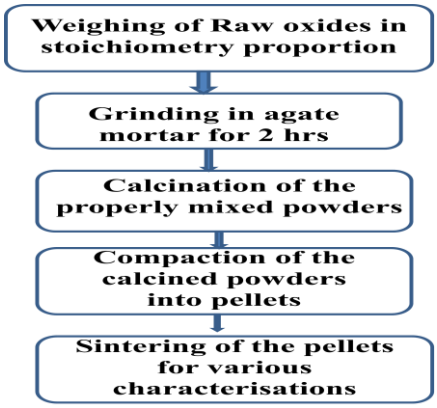

Figure 2.1: Flow chart for solid state reaction method for preparation of bulk silver niobate.

2.3. Characterization techniques

There are several techniques which is used to characterize a Material to have fundamental knowledge about its basic features. We employ these techniques according to the necessity of information about the material to unravel. In ceramic type of compounds mostly use as functional materials researchers are interested to know about the structure, composition, chemical state, electrical and magnetic properties etc. To gather this information characterization techniques such as X-ray diffraction, Raman spectroscopy, X-ray Photoelectron Spectroscopy, Scanning Electron Microscopy, Field Emission Scanning Electron Microscopy are very necessary. We are briefing under the utility and the principle of operation for some of the important technique that are availed during our research.

2.3.1. Structural and microstructural characterization

X-ray diffraction

The structure of a compound in which it is crystallized keeps much significance in governing the physical properties such as electrical, magnetic, optical etc. Therefore, it is essential to have a basic idea of the position of the cations and anions at the crystal matrix, the nature of bonding, the surrounding of each ion and its distance from close neighbour. X-ray diffraction is a significant and non-destructive technique to obtain a pattern which is the finger print of a material. The position of the peaks will provide the first information about the phase of the targeted compound. Apart from this, we can derive lattice constant, bond angles, bond length, crystallite/particle/grain size and strain etc. [99, 100].

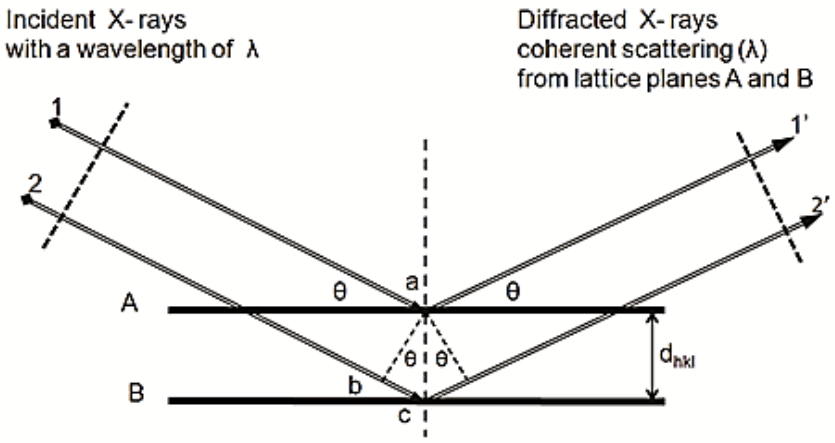

Figure.2.2: Constructive interference from the parallel planes.

The working principle of the instrument based upon the Bragg's law. Mostly the lattice plane separation comes in the range of wavelength of X-ray and hence able to scatter the radiation. The constructive interference of the diffracted X-radiation gives the interference pattern which depends upon the lattice inter planer spacing obeying the law given by Bragg i.e.

$$2d \sin \theta = n\lambda \qquad (2.1)$$

Where d is the inter-planar distance, θ is the Bragg angle, n is the order of the diffraction and λ is the wavelength of the incident wave. Figure 2.3 shows Bragg's diffraction from

parallel planes. This law indicates that the constructive interference of diffracted waves takes place only when the inter-planar path difference is integral multiple of the incident wave length [99-100].

Figure 2.3: X-Ray Diffraction unit (**RIGAKU JAPAN/ULTIMA-IV)**

Raman spectroscopy

Raman shift depends upon the nature of the substance and independent of the exciting radiation. Therefore, it can provide the characteristic feature of a material. Raman shift can be measured by obtaining Raman spectroscopy which is based on the phenomenon called Raman scattering, named after the Indian scientist Sir C.V. Raman who first discovered it in 1928.In Raman scattering measurement, a single frequency light, usually from a single mode laser source, is made to incident on the sample and scattered light is collected at an angle with respect to the incident light to minimize Rayleigh's scattering. The inelastically scattered light with lower {stokes scattering} or higher {anti-stokes scattering} frequencies can be measured with photo detector. The energy difference between the scattered and incident light is known as Raman shift (usually given in a wave number $cm^{-1} = 1/\lambda$ with wavelength λ expressed in cm), which equals to the vibrational or phonon frequency of the sample, as long as selection rule is allowed. The spectrum is usually presented in terms of the intensity of the Raman scattered light as a function of Raman shift [101, 102].

X-ray photoelectron spectroscopy (XPS)

XPS is based on the measurement of the kinetic energy of photoelectrons generated when the sample is illuminated with soft (1.5 kV) x-ray radiation in an ultra-high vaccum. If one x-ray photon with energy $h\nu$ is used to excite an atom in its initial state with energy

E_i and to eject an electron with kinetic energy, KE, with the atom resulting in a final state with energy E_f, one would have the following equation based on total energy conservation

$$h\nu + E_i = KE + E_f \qquad (2.2)$$

The difference between the photon energy and electron kinetic energy is called binding energy of the orbital from which the electron is ejected and the ejected electrons are equal to $E_f - E_i$ which is shown in above equation. Since the photon energy is known from X-ray radiation source and the electron

Figure 2.4: X-Ray photoelectron spectroscopy (**XPS**)

KE can be measured, the binding energy can be determined, which gives the energy difference between final and initial state of the atom involved in transition. This binding energy is characteristics for different orbitals of specific elements and is roughly equal to the Hartree-Fock energy of the electron orbital. Therefore, peaks in the photoelectron spectrum can be identified with the specific atoms and surface composition can be analysed. Because the photoelectrons are strongly attenuated by passage through the sample of material itself, the information obtained comes from the sample surface, with a sampling depth on the order of 5 nm. Chemical bonding in molecules will cause binding energy shifts, which can be used to extract the information of a chemical nature {such as atomic oxidation state} from the sample surface [101-103].

Scanning Electron Microscope (SEM) and Field Emission Scanning Electron Microscope (FESEM)

Optical microscopes have limited spatial resolution, usually on the order of a few hundred nm in the best case scenario, due to the diffraction limit of light. Higher resolution, a few nm or even sub nm, is needed for many applications, especially in the study of nano-materials. Scanning electron microscopy is a powerful and popular technique for imaging the surfaces of almost any materials with a resolution down to about few nm. The image resolution offered by SEM depends not only on the property of the electron probe, but also on the interaction of the electron probe with the specimen. The interaction of an incident electron beam with the specimen produces secondary electrons, with energy typically smaller than 50eV, the emission efficiency of which sensitively depends on surface geometry, surface chemical characteristics and bulk chemical composition. SEM can thus provide information about the surface topology, morphology and chemical composition. FESEM gives clearer and less distorted pictures with spatial resolution to 1

½ nm which is 3-6 times better than the conventional SEM. In addition to that it produces high quality and low voltages images with negligible electrical charging of samples [104-105].

Figure 2.5: Scanning Electron Microscopy (JEOL JSM-6084LV)

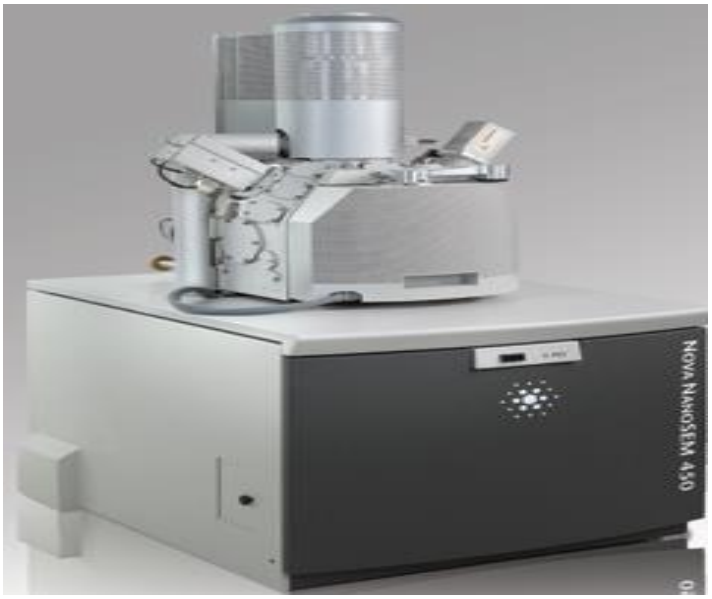

Figure 2.6: Field Emission Scanning Electron Microscopy (Nova NanoSEM/ FEI)

2.3.2. Electric characterization

Impedance measurement (AC Resistance)

AC resistance measured by the HIOKI impedance analyzer model IM3570 using two probe method. The data was collected by using the software supplied by the HIOKI Company which connects computer the impedance analyzer. Impedance is a complex resistance experienced by the current when it passes through the circuit consists of resistors, capacitors and inductors. Similar to the resistance is the ratio of voltage to the current. Impedance has real and imaginary parts. Real part demonstrates the ability of

circuit to resist the current and imaginary part relate to ability of circuit to store electrical energy. When AC voltage V of amplitude V_A and frequency f applied then it can be explained in terms of time t is

$$V(t) = V_A \sin(2\pi ft) = V_A \sin(\omega t) \quad (2.3)$$

where ω is radial frequency and is equal to 2πf. The current of the signal is, if it is a linear system [9],

$$I(t) = I_A \sin(\omega t + \varphi) \quad (2.4)$$

Then the impedance will be $Z^* = \frac{V(t)}{I(t)} = \frac{V_A \sin(\omega t)}{I_A \sin(\omega t+\varphi)} = Z_A \frac{\sin(\omega t)}{\sin(\omega t+\varphi)}$ (2.5)

The voltage and current functions can also described as $V(t) = V_A e^{-i\omega t}$ and $I(t) = I_A e^{-i\omega t - i\varphi}$

$$Z^* = \frac{V(t)}{I(t)} = Z_A e^{-i\varphi} = Z_A (\cos\varphi + i\sin\varphi) = Z_{real} + jZ_{im} \quad (2.6)$$

Real part of the impedance $Z_{real} = Z' = Z_A \cos\varphi$

Imaginary part of the impedance $Z_{im} = Z'' = Z_A \sin\varphi$

Cole-Cole plots

If any signal is applied to pure resistor then Z*= R (resistance) or applied to the pure capacitor then $Z^* = -j(\omega c)^{-1}$ where C is capacitance. Real life systems cannot be represented by the neither pure resistor nor pure capacitor rather than the combination of resistor and capacitor. Let us consider an AC signal is applied to the parallel combination of the resistor and capacitor the impedance can be written as:

$$Z^* = \frac{R}{1+(\omega RC)^2} - j\frac{\omega R^2 C}{1+(\omega RC)^2} \quad (2.7)$$

$$Z_{real} = \frac{R}{1+(\omega RC)^2} \quad (2.8)$$

$$Z_{im} = -\frac{\omega R^2 C}{1+(\omega RC)^2} \quad (2.9)$$

If real impedance plotted on the x axis and imaginary impedance plotted on the y axis then the pot is known as Cole-Cole plot [104-105].

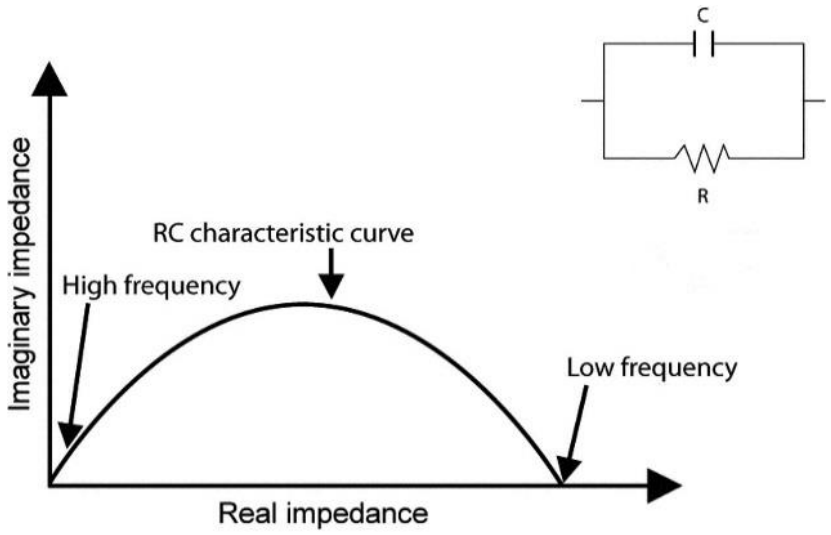

Figure 2.7: Cole-Cole plot.

Low frequency data is right side of the plot and higher frequencies are left is shown in Fig 2.7**.** The impedance spectra often appear as single or multiple arcs in the complex plane. Cole Cole plots have great importance to study the electrical properties because the shape of the plot yields insight into possible conduction mechanisms [104-105].

Dielectric analysis

The dielectric analysis explains the permittivity and conductivity of material properties as a combined complex permittivity ϵ* which is analogues to the complex impedance. Just like complex impedance it is also represented by its real and imaginary components

$$\epsilon^* = \epsilon' - j\epsilon'' \qquad (2.10)$$

where ϵ' is real permittivity and often is called dielectric constant and ϵ" is imaginary permittivity and referred as loss factor. The real permittivity can be calculated from the capacitance measured through the two probe method using impedance analyzer. Relation between capacitance and real permittivity is

$$\epsilon' = \frac{Cd}{A\epsilon_o} \qquad (2.11)$$

Where d is the distance between the two electrodes and A is the area of the sample and ϵ_o is the permittivity of the free space [84].

Electric modulus

The modulus is the inverse of complex permittivity ϵ* and can also be expressed as a derivative of complex impedance.

$$M^* = \frac{1}{\epsilon^*} = M' - jM'' \qquad (2.13)$$

Where M' is Real part of the modulus and M" is imaginary part of the modulus. Fundamentally, complex electrochemical impedance (Z*), modulus *(M*)* and permittivity (ϵ*) parameters are all determined by applying an AC potential at a variable frequency and measuring output current through the sample. In a broader sense dielectric, modulus,

and impedance analysis represent the same operational principles and can be referred to as subsets of a universal broadband electrochemical impedance spectroscopy.

P-E Hysteresis Loop Measurement

Polarizations vs. electric field (P-E) measurements were performed using precision premier II, a standard ferroelectric testing machine (Radiant Technology). The sample is coated with metallic silver paste which will act as conducting layer. It is then set for heating for a good adhesion [12].

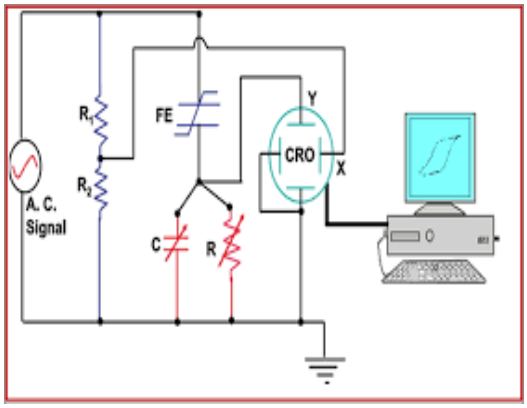

Figure 2.8: Schematic circuit of P-E hysteresis loop.

Fig. 2.8 shows the modified Sawyer-Tower circuit designed and fabricated for the investigations on ferroelectric hysteresis (P-E) and J-E loops in the composite films. The AC signal in a frequency range, 10 Hz-1 kHz from the function generator (Scientific SM 5060) was used to obtain the hysteresis loops for a ferroelectric material. The voltage lying across the ferroelectric sample is put on the horizontal plates of the digital storage oscilloscope, thus plotting, a quantity which is proportional to the field across the sample on the horizontal axis. The parallel RC circuit is connected in series with the sample, which allows compensation for any phase shift due to conductivity or dielectric loss in the sample. The value of capacitance, C is chosen to be large enough so that most of voltage drops in the circuit occurs across the ferroelectric material. The voltage, V developed across C is proportional to the charge flowing through the polar materials. Thus, the polarization $P = q/A = CV/A$ (where A is area of sample) is plotted on vertical axis. The Sawyer-Tower circuit not only displays the hysteresis loop on the oscilloscope screen but also measures the important quantities such as P_r and E_c.

Chapter 3

Dielectric, ferroelectric and impedance spectroscopic studies of $AgNbO_3$ ceramic

3.1 Introduction

Recently, a family of Ag-based oxides Ag_3PO_4, Ag_2CO_3, $AgVO_3$, $AgGaO_2$, Ag_2CrO_4, $AgNbO_3$ etc. has attracted particular interests due to their ability to split water, as well as decompose organic contaminants both in air and aqueous solution. Among them, $AgNbO_3$ was a highly studied material for visible light driven photocatalytic activity [107, 108]. But, the discovery of a strong field induced double hysteresis loop having saturation polarisation of 52 μC/ cm^2 in its polycrystalline form and revelation of high permittivity (ε_r> 400) in microwave/radio frequency range for $AgNb_{1-x}Ta_xO_3$ (x = 0.5) solid solution, has also diversified its application in semiconductor industries [82-86]. The compound also exhibits multiphase transition in its temperature dependent permittivity plot which is also very much informative for fundamental research to understand cation movements. The compound assumes distorted perovskite ABO_3 structure at room temperature. The recent group of researchers assigned the non-centrosymmetric $Pmc2_1$ space group to explain its weak ferroelectricity which brings to an end of the earlier assigned centrosymmetric Pbcm space group which was meant for antiferroelectric behaviour [57-61].

Silver based compound prepared from Ag_2O, $AgCO_3$ etc. as raw materials, faces a problem of precipitation of metallic silver nanoparticles during high temperature processing of the compound [107, 108]. Though, these precipitated particles were reported to enhance the photocatalytic properties but, whether the various electrical properties like permittivity, conductivity, ferroelectricity etc. are influenced or not, yet to be investigated. This precipitated particles deposits near various interfaces like grain boundary or surface of the sample, is also previously reported by the TEM and HRTEM images [85, 86]. What we are assuming that, the precipitated metallic silver nano particles will affect the electrical properties if any extrinsic conduction (interfacial conduction like grain boundary or surface-electrode contact) will contribute to the total conductivity. The study of ε(T) cannot provide any information about the role of these precipitated particles, as contribution of microstructure cannot be distinguished. In this context, impedance spectroscopy is an appropriate technique to analyse the conduction mechanism and differentiate the role and contribution of different microstructures. The charge carrier movement within grain contributes to intrinsic conduction and that of along any interfaces like grain boundary or sample surface contributes to extrinsic conduction. The activation of charge carrier in these regions depends upon the temperature as well as frequencies and they will remain relax when unable to follow to the changing cycle of electric field. At this stage, a peak will appear in the impedance spectrum and the appearance of number of relaxation peaks with their sequence will inform about the activated region. By distinguishing the activated regions whether intrinsic and extrinsic one can assert the role

of the precipitated metallic silver nano particles [109-111]. Some of the earlier works also reported the frequency dependent permittivity and susceptibility study in a wide range of frequency which mostly explained the dynamics of different cations which affects dielectric behaviour. There is no report regarding the contribution of surface microstructures like grain, grain boundary, sample surface, defects etc. [62-67].

In the present work, we have systematically and successfully investigated the electric transport properties of $AgNbO_3$ (AN) and distinguished the intrinsic and extrinsic conduction in the material. We have carried the impedance measurement within frequency domain of 100Hz to 1MHz and within the temperature range (25 ^oC to 450 ^oC) containing its major dielectric anomalies.

3.2 Experimental details

We prepared $AgNbO_3$ by standard solid state reactions. Starting materials Ag_2O and Nb_2O_5 were mixed stochiometrically for respective compound and 3wt% extra Ag_2O was added to meet the silver loss due to its volatility [41, 58]. After two hours of manual grinding, the properly mixed powders were kept in an alumina crucible for calcination at 830 °C for 6h in air. The calcined powders were mixed with 3 wt% polyvinyl alcohol (PVA) solution with proper milling and uniaxially pressed into disks of diameter ~10 mm and a thickness ~ 1 mm using hydraulic press under ~70 MPa pressure. The prepared pellets were kept over an alumina plate for sintering at 1030 °C for 3h in normal atmospheric condition. The pale yellow colour pellet of AN system was collected after sintering. X-ray diffractograms of all the compositions were investigated by using the XRD (Rigaku Ultima-IV) using nickel filter with Cu K_α radiation issuing from a 1.6 kW Rigaku rotating anode generator. Measurements were taken on reflection mode of oriented crystal pellets for step size 0.025^o at scanning rate 10^o per minute. The microstructures of sintered pellets were observed using a Nova Nano SEM/FEI field emission scanning electron microscope (FESEM) as well as the mapping images of the samples was taken. The pellets were allowed for Au coating on the targeted surface by a sputtering unit up to two minutes. This was intended to avoid the accumulation of electrons on the surface of the samples due to electron irradiation during image. The dielectric data at four selected frequencies in a temperature range 25 ^oC – 450 ^oC were taken by using HIOKI IMPEDANCE ANALYZER IM3570 during heating as well as during cooling processes. For electrical measurements, the sintered pellets were coated with silver electrodes and fired at 400°C for 30 min for good adhesion. The furnace was controlled with 2^oC rise per minute during the collection of dielectric data. Polarizations vs. electric field (P-E) measurements were performed using precision premier II, a standard ferroelectric testing machine (Radiant Technology).

3.3 Data analysis

The impedance can be expressed as, $Z = Z' + i\,Z''$, where Z' and Z'' are the real and imaginary impedance values which are derived as $Z' = Z\cos\theta$, and $Z'' = Z\sin\theta$. The value of real (ε') and imaginary part (ε'') of permittivity are derived from the relation $\varepsilon' = \frac{Z''}{Z'^2+Z''^2} \times \frac{1}{\omega C_o}$ and $\varepsilon'' = \frac{Z'}{Z'^2+Z''^2} \times \frac{1}{\omega C_o}$ where, ω is the angular frequency, C_o is the capacitance of free space and ε_0 is the permittivity of free space (8.854×10^{-12} F/m). The electric modulus can be expressed as $M = M'+iM''$ where $M' = M\cos\theta$ ($= \omega C_o Z''$) and $M'' = M\sin\theta$ ($= \omega C_o Z'$).

3.4 Results and Discussion

3.4.1 XRD, SEM, XPS and RAMAN spectrum studies

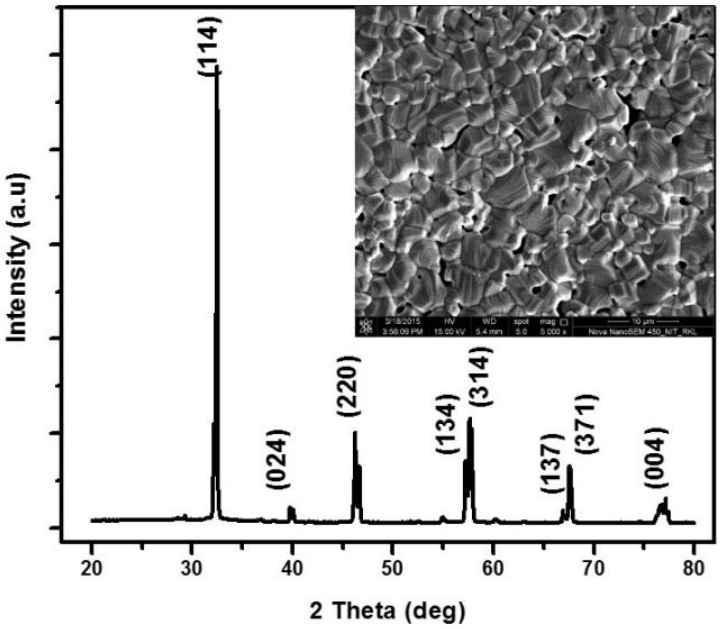

Figure 3.1: XRD and FESEM of $AgNbO_3$ system

The XRD pattern of the prepared sample is shown in Fig. 3.1, and its inset shows the corresponding FESEM image. Positions of all the diffraction peaks are well indexed to orthorhombic $AgNbO_3$ (JCPDS Card No. 070-4738/ 052-0405) [93-95]. Minute traces of secondary phases are unavoidable irrespective of synthesis conditions [41]. FESEM image of AN system shows little varied size of grains having average size of 2µm. Small traces of pores present in the samples. Experimental density ~91% of theoretical density is obtained of the sintered AN ceramic sample.

Raman spectra provide important information regarding the internal vibration in the crystal lattice. Fig. 3.2 shows the different vibrational modes obtained in our prepared sample of the parent AN and its modified system which agrees well with the previous reported data. It is observed that all the internal vibrations related to NbO_6 octahedra lies within 160 cm^{-1} to 900 cm^{-1}. Around the region 170 cm^{-1} to 325 cm^{-1}, the first intense mode is observed which is splitted and corresponds to the degenerated modes assigned as υ6 and υ5 respectively. The modes ~ 360 cm^{-1} and ~ 420 cm^{-1} are of low intensity which are assigned as υ4 and is supposed to be the associate bending modes of Nb-O-Nb bonds. The possible cause for this low intensity is due to the low tilting angle between the adjacent NbO_6 octahedra. The second intense mode appears ~ 575 cm^{-1} – 610 cm^{-1} with a shoulder ~ 525 cm^{-1} – 575 $cm^{-1}$are assigned as υ_1 and υ_2 respectively. These modes are supposed to be arised due to the symmetric stretching of The NbO_6 octahedra which corresponds to different Nb-O bond lengths [114, 115].

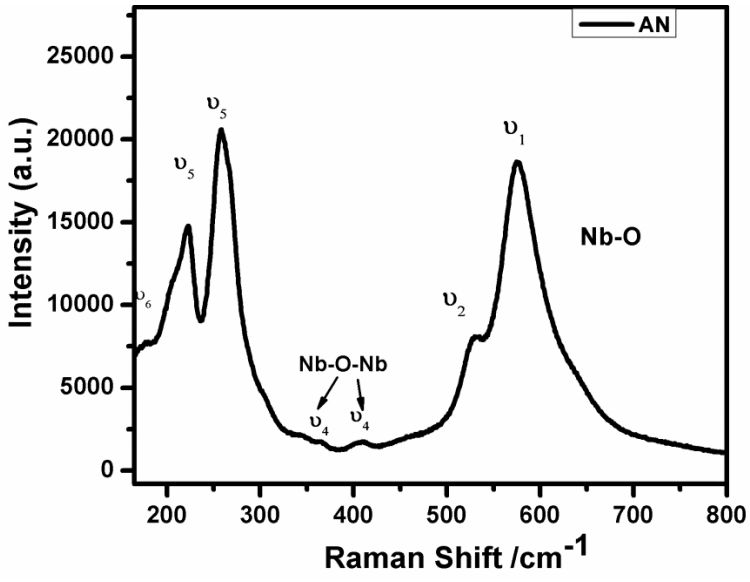

Figure 3.2: Raman vibrational modes of $AgNbO_3$ system

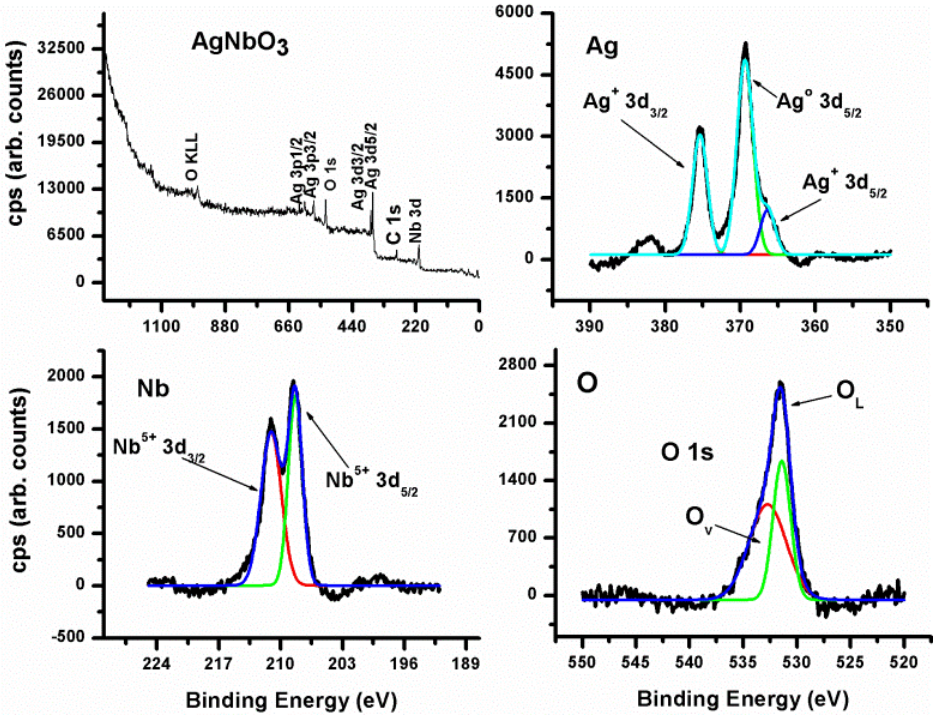

Figure 3.3: XPS spectra of $AgNbO_3$ system

Fig. 3.3 illustrates the XPS results of the $AgNbO_3$ systems. The appeared peaks are deconvoluted and the binding energy corresponding to the peaks indicate that silver exists in Ag^{+1}state; niobium exists in Nb^{5+} state. But the position of the peak ~ 368ev indicates the presence of $3d_{5/2}$ (Ag^0) related to metallic silver particles. In addition with oxygen O^{2-} state a small trace of oxygen vacancy peak is also identified [54, 115].

3.5 Dielectric study

Fig. 3.4 exhibits the temperature dependent permittivity (ε) at different frequencies for AN system. Four dielectric anomalies at $T_C^{FE} \approx 85°C$ ($M_1 \leftrightarrow M_2$), 270°C ($M_2 \leftrightarrow M_3$), $T_C^{AFE} \approx 350$ °C ($M_3 \leftrightarrow O_1$) and 386°C ($O_1 \leftrightarrow O_2$) are observed in our prepared sample which matches mostly to the earlier reports where M_1 region is ferroelectric (FE), M_2 and M_3 regions are antiferroelectric (AFE) and finally O_1, O_2 are in paraelectric state (PE) [42-44].

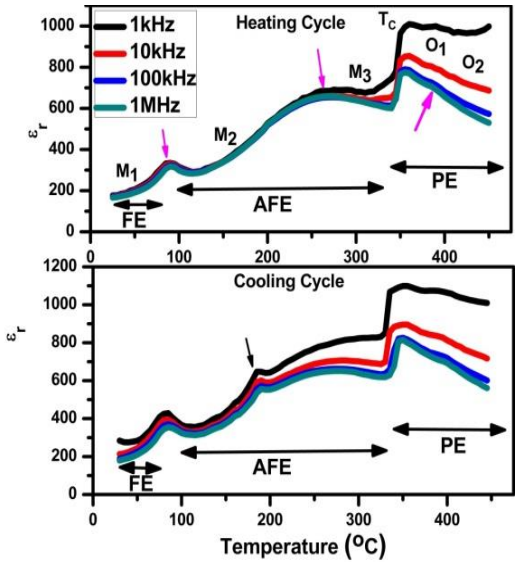

Figure 3.4: Temperature dependent relative permittivity of $AgNbO_3$ system

However, the transition temperature for T_C^{FE} is reported to be around 67°C to 70°C is somehow appears at little higher. In a recent study, Kania et al. reported that particularly, T_C^{FE} peak varies with the concentration of Ag^{1+} ion [45]. The nature of the shape of ε (T) and the position of all the dielectric anomalies which confirmed the good quality of polycrystalline $AgNbO_3$ prepared in normal condition and can suitably studied for electrical investigation.

3.6 Impedance and Electric modulus study

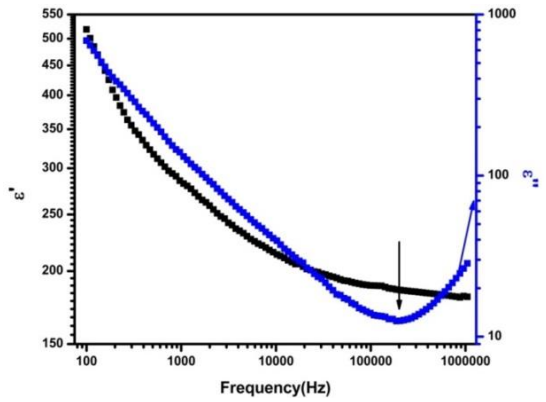

Figure 3.5: Real and imaginary part of relative permittivity of $AgNbO_3$ system at room temperature

Fig.3.5shows the combined plot of real (ε') and imaginary (ε") parts of effective complex permittivity of AN system as a function of frequency at RT. At frequency less than 1 kHz, the figure shows strong dispersive nature of real part of permittivity (ε'), swift variation occurs below 100 kHz and nearly frequency independent feature appears while approaching high frequency window. No relaxation peak appears in the imaginary part (ε") within the frequency windows but a U-turn region appears above 100 kHz which marks the increasing value in both the cases. It is observed that the high frequency U-turn in (ε") corresponds to the nearly frequency independent region of (ε') which signals the arrival of dipolar relaxation state [116-118].

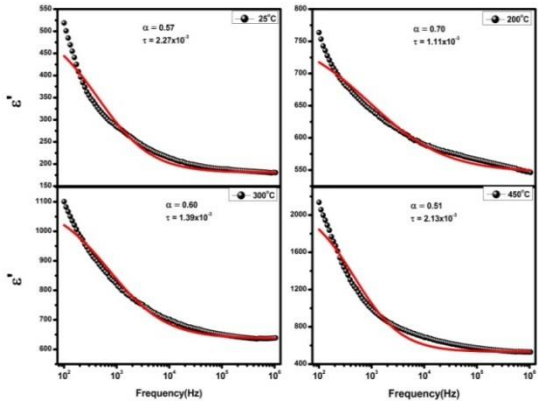

Figure 3.6: Real part of relative permittivity Simulated with modified Debye equation $AgNbO_3$ system at room temperature

In order to calculate the activation energy of the dipolar relaxations, we follow the modified Debye relaxation model, given by eq (1) [117].

$$\varepsilon' - \varepsilon_\infty = \frac{\varepsilon'_0 - \varepsilon'_\infty}{[1+(\omega\tau)^{2(1-\alpha)}]} \qquad (3.1)$$

Where, ε'_o – static permittivity, ε'_∞ - very high frequency permittivity, ω - angular frequency, τ – relaxation time and α - a parameter to describe the extent of difference from standard Debye relaxation. Fig.3.6 shows the mathematically simulated with experimental data for some selected temperatures. From the best fitted plots we derive a series of relaxation times and it is found that they follow the Arrhenius law shown fig. 3.7

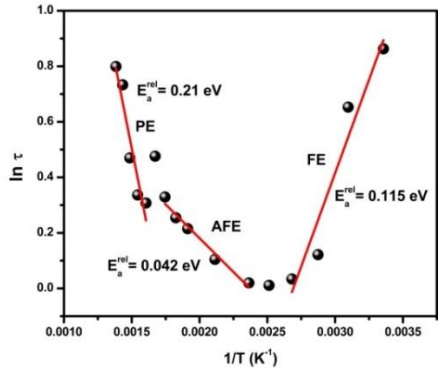

Figure 3.7: Activation energies of domain wall motion $AgNbO_3$ system at room temperature

$\tau = \tau_o \exp(E_a^{rel}/ k_B T))$, where τ_o- relaxation time at infinite temperature, E_a - relaxation activation energy, k_B- Boltzmann constant, and T is the temperature. Three distinct

Arrhenius regions are found out having activation energy $E_a \approx 0.115$ev in FE region, $E_a \approx 0.042$eV in AFE region, and $E_a \approx 0.21$eV in PE region. The small value of activation energies explains the domain wall motion and its high mobility. This may be associated with n or p type hopping of charge or small polaron conduction mechanism [116-118].

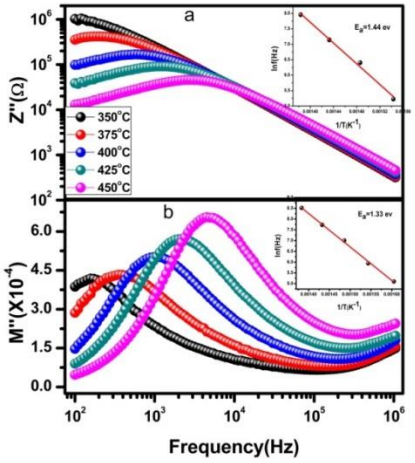

Figure 3.8: Imaginary part of impedance and electric modulus of $AgNbO_3$ system at selected temperatures. In set shows the activation energies.

Studying the imaginary part of impedance (Z") and electrical modulus (M") helps a lot to examine the low frequency relaxations. The inability of resolving the multiple relaxations properly within low frequency regime in Z" can be solved in better way in M" as the latter one scales inversely to capacitances. Fig. 3.8(a) and (b) shows selective plots of the impedance (Z"(f)) and electrical modulus (M"(f)) respectively which exhibits relaxation process. A feeble, not properly defined relaxation peak enters through the low frequency window of M"(f) around 345^{o}C which becomes prominent and shifts towards higher frequency side with elevated temperature. The low frequency relaxation also appears in Z"(f) but in a later stage around 375^{o}C and in similar manner shifts towards higher frequency with rising temperature. The existing dipoles contribute their maximum electrical response at the frequency corresponding to the relaxation peak and beyond which they remain in relaxed state. The inset of Fig.3.8 plots the log f_{max} vs. 1/T separately for Z"(f) and M"(f) which indicates the relaxation process is characterised by Arrhenius type behaviour ($f = f_0 \exp(E_a^{rel}/ k_B T)$), where f_0 is the pre-exponential factor and E_a^{rel} represents the activation energy of dielectric relaxations. We found the value of E_a^{rel} to be of 1.36eV and 1.38eV from electric modulus and impedance data respectively which is a bigger enough to be assigned with possible grain conduction only [116].

To verify the presence of multiple relaxation processes such as grain, grain boundary or surface conduction etc., we have investigated the AN bulk system through studying Cole-Cole of impedance (Z" vs. Z') and electric modulus (M" vs. M'). The spike form of Cole-Cole of impedance continues up to 270^{o}C and that indicates the strong insulating nature of the compound. Thereafter, it bends towards abscissa to take the shape of a semi-circular arc around 350^{o}C which signals the beginning of relaxation process. Fig, 3.9 illustrates the Cole-Cole semicircles at selected temperatures. In the diagram, it is observed that only one semicircle appears within frequency domain.

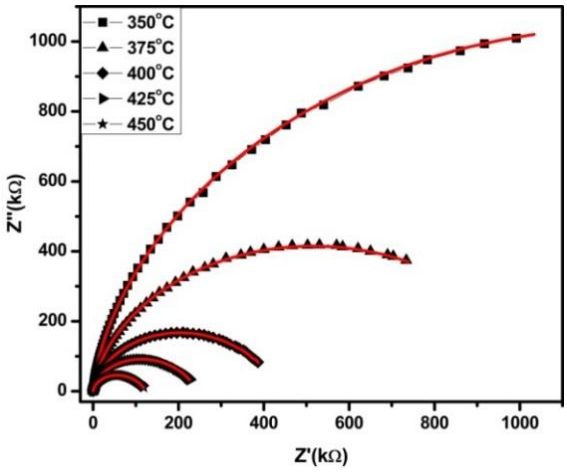

Figure 3.9: Cole-Cole of impedance of $AgNbO_3$ system at selected temperatures, simulated with equivalent electric circuit model of R_S (RCQ).

The radii of the semicircles decrease and their centres seem to be lie below the abscissa with elevation of temperature. This suggests for a non-Debye type conduction process. In a similar manner, only a single semi-circular arc appears in the Cole-Cole of modulus, shown in Fig.3.10. This confirms that a single relaxation process dominates over the conduction mechanism which can be identified as grain effect.

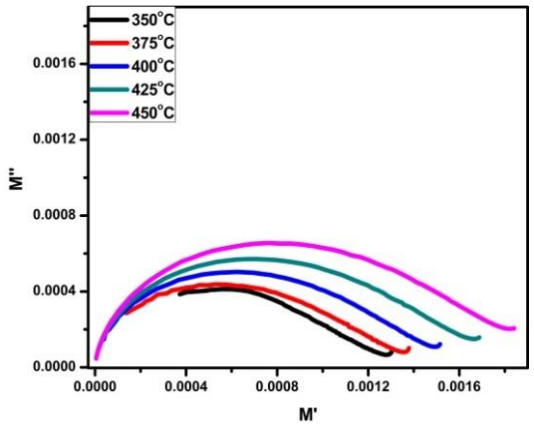

Figure 3.10: Cole-Cole of electric modulus of $AgNbO_3$ system at selected temperatures.

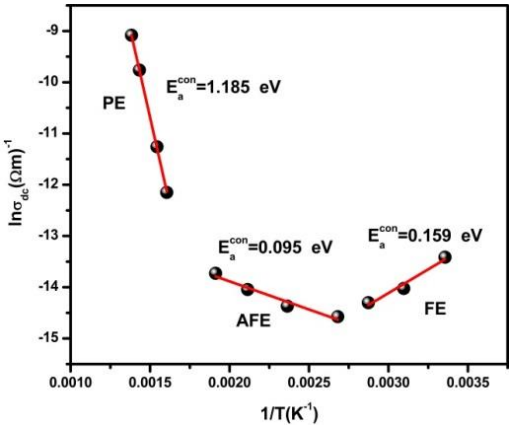

Figure 3.11: Activation energies derived from Arrhenius regions of DC conductivity.

Again, to make out the correlation between the charged defects and the observed electrical properties an equivalent electric circuit is modelled. It is found that the observed electrical properties fit properly to the equivalent circuit of R_s(RCQ), where R_s is the resistance contributed from electrode, 'R' stands for grain resistance, 'C' for grain capacitance. The parameter 'Q' is the constant phase element (CPE) which also signifies as modified capacitance of the AN bulk system. The equivalent impedance of CPE is given by $Z^* = [B(j\omega)^n]^{-1}$, which is the modified version of Jonscher's "universal dielectric response" behaviour of disorder systems. Here, 'B' and 'n' are constants and the value of 'n' which determines the degree of departure from the ideal capacitor behaviour lies between 0 to 1. For n = 0, Q behaves as a perfectly resistor and for n = 1, it acts as a capacitor. The well fitted curve proves the close agreement between the experimental result and the simulated electric model containing single (RCQ) element. Such accuracy in fitting of experimental curve with single element (RCQ) confirms the single relaxation process which attributes to grain. Therefore, the macroscopic relaxation process is moreover due to the microscopic conduction which occurs inside the grain and the grain boundary conduction is neglected as the possibility of ionic diffusion along the boundary has been ruled out. We have extracted the value of 'R' from the best fitted curve and estimated the dc conductivity by putting formula $\sigma = d/AR$, where d- thickness of sample, A- area of cross-section. The estimated conductivity data is plotted as a function of temperature as shown in Fig.3.11 and is found to obey the Arrhenius behaviour of $\sigma = \sigma_o * \exp(E_a^{con}/ k_B T)$, where E_a^{con}- activation energy for the relevant conduction process. The plot of Fig. 3.11 shows three distinct regimes: (i) FE region, T< 100^{o}C, E_a^{con} =0.159eV, (ii) AFE region, 100^{o}C < T < 350^{o}C, E_a^{con} = 0.095eV and (iii) PE region, T > 350^{o}C, E_a^{con} = 1.185eV.

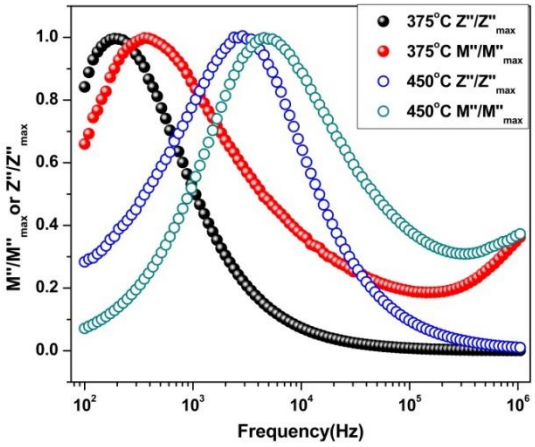

Figure 3.12: Normalized functions M''/M''_{max} and Z''/Z''_{max} of $AgNbO_3$ system at selected temperatures.

In order to differentiate the long range or short range migration of charged defects, we have plotted the normalized functions M''/M''_{max} and Z''/Z''_{max} as a function of frequency at selected temperatures which is shown in fig. 3.12. If the peaks of Z" and M" coincide with each other then it indicates for the domination of long range migration of charge carriers in the conduction process. If the peaks have a significant gap then localized or short range migration of charge defects takes part in conduction. In our case, the marginal gap between the peaks at 350 ^{o}C reduces to narrow gap at 450^{o}C. This suggests for an electrical response mostly dominated by localized or short range migration of charge defects. But, as soon as temperature elevates long range hopping of charge defects evolves. And hence at end studied temperature, a mixed conduction mechanism of both

short range and long range hopping of charge carriers dominates. This long range hopping of charge carriers contributes to dc conductivity [109-112].

In order to identify the nature of charge defects participated in the observed relaxation and conduction mechanism, we searched the previous literature which have reported the activation energies of approximately equal the value we have obtained. The activation energy observed in ferroelectric region is of 0.159 eV and thereafter, throughout the antiferroelectric region, this value reduces to 0.0946 eV. Such a low value of activation energy has been mentioned in perovskite oxide and in several complex oxide systems which is attributed to the migration of localized charge carriers such as polaron. High temperature sintering creates a possibility for presence of oxygen vacancies in metal oxide systems which forces electrons to occupy the site as charge compensators. The lattice distortions somehow accompanied with the compensating electrons to form bound states which often act as effective dipoles. When the electrons hop in association with the lattice distortion in response to the applied ac field that generates short range polaronic hopping as well and hence, dipole reorientation takes place. Again, the obtained activation energy of 1.185 eV in paraelectric region is very much similar to the value of ionic conduction or migration of oxygen vacancies. It is reported that small polarons play a vital role in the high polarisation whereas the migration of oxygen vacancies has its importance during relaxation processes [119-120].

It is established that only the intrinsic grain conduction has the dominant role within the selected frequency domain and described temperature range which contains the most important dielectric anomalies at proper positions. The contribution of interfacial conduction of any kind such as grain boundary or surface polarisation are found absent or may have any negligible presence to affect the conduction process. The effect of unavoidable precipitation of metallic silver particles in the electrical properties of $AgNbO_3$ is a grave concern, which is supposed to be deposited along the various interfaces like grain boundary or the sample-electrode surface. The absence of any interfacial relaxation within the study range suggests that the charge carriers along these regions have not activated or negligible participated in the conduction process. Therefore, in the prescribed frequency and temperature ranges, the precipitated silver nano particles have no significant role in the conductivity as well as permittivity of the titled compounds.

3.7 Conclusion

The $AgNbO_3$ sample was prepared by standard solid state technique at normal conditions and its quality of the crystal was verified after finding proper shape and dielectric anomalies at appropriate positions. Relaxation mechanism was studied from real part of permittivity and imaginary part of both impedance and electric modulus. Only single relaxation process attributed to grain was addressed within the prescribed frequency and temperature zones as well as nature of different charged defects contributing towards conduction were sorted out. The much doubtful role of precipitated silver nano particles in electrical properties were ruled out within the temperature range containing major dielectric anomalies, as they were supposed to be deposited along various interfaces like grain boundaries.

Chapter 4

Dielectric, ferroelectric and impedance spectroscopic studies of Ta_2O_5, Sb_2O_5 and V_2O_5-doped $AgNbO_3$ ceramics

4.1. Introduction

Recently, $AgNbO_3$ based materials have attracted much attention of the researchers due to their unique microwave properties. It is revealed that, $AgNb_{1-x}Ta_xO_3$ solid solution, with $x = 0.5$, as a new high permittivity ($\varepsilon_r > 400$) microwave material that is applicable in the microwave- and radio-frequency region [82-86]. The compound assumes distorted perovskite ABO_3 structure at room temperature. The recent group of researchers assigned the non-centrosymmetric *Pmc2₁* space group to explain its weak ferroelectricity which brings to an end of the earlier assigned centrosymmetric *Pbcm* space group which was meant for antiferroelectric behaviour [57-61]. The compound suddenly dragged the attention when it is reported that a strong field induced double hysteresis loop having saturation polarisation of 52 μC/ cm^2 appears in its polycrystalline form at a high applied field of 220kV/cm [49]. Apart from this, $AgNbO_3$ is also an attractive material as a candidate of visible light photocatalyst for the organic pollutants degradation. The versatility of this material makes it a suitable candidate for fundamental research as well as modifies it to bring the potential for several electrical and electronic components. There exists a complicated coupling between NbO_6 octahedral tilting and local displacements of both Ag and Nb that mechanised a series of changes in the cation displacements off their sites which are the cause of ferroelectricity and dielectric property of the material [57-61]. Most of the literature based on enhancement of ferroelectricity and dielectric behaviour also figure out the role of excess octahedral rotation or tilting which locks the off-centering behaviour of Ag and to suppress that one by inducing chemical pressure in $AgNbO_3$. The strong dependence of dielectric and ferroelectric properties of $AgNbO_3$ on crystal structures and dynamics of cations are revealed through many works but still the role of microstructures on its electrical behaviour is not properly investigated. Like volatile problem of Bi in bismuth ferrite, in $AgNbO_3$, the volatility of silver left option for creation of oxygen vacancies and compositional inhomogeneity. But, unlike the leakage problem and high dielectric loss in former, moderate dielectric loss characteristic features in latter case.

To enlarge the fundamental idea we have modified the AN system by doping Ta_2O_5, Sb_2O_5 and V_2O_5 separately by low (10%) molar percentage. The purpose of modification is to bring the effect of minute substitution of isovalent dopant in the surface morphology and to observe the related effects on electric transport properties as well as dielectric and ferroelectric properties. By complex impedance analysis we have investigated the

role/effect of different microstructures on the electrical properties of the parent system which have been elaborated in the present report.

4.2. Experimental details

We prepared $AgNbO_3$ by standard solid state reactions by taking Ag_2O, Nb_2O_5 (Alfa Aesar grade) as the starting materials. Again, we add 10% molecular weight of dopants like Ta_2O_5, Sb_2O_5 and V_2O_5 to prepare $AgNbO_3/Ta_2O_5$ (ATN), $AgNbO_3/Sb_2O_5$ (ASN) and $AgNbO_3/V_2O_5$ (AVN) modified systems. Additional 3wt% of Ag_2O was added to compensate the loss of silver due to its nature of volatility [41, 58]. The weighed raw materials were grinded properly in order to bring a homogeneous presence of all the metal oxides to set for an easy thermal reaction. After two hours of manual grinding, the properly mixed powders were kept in an alumina crucible for calcination at 830 °C for 6h in air. The calcined powders were mixed with 3 wt% polyvinyl alcohol (PVA) solution with proper milling and uniaxially pressed into disks of diameter ~10 mm and a thickness ~ 1 mm using hydraulic press under ~70 MPa pressure. The prepared pellets were kept over an alumina plate for sintering at 1030 °C for 3h in normal atmospheric condition. The pale yellow colour pellet of AN system was collected after sintering. X-ray diffractograms of all the compositions were investigated by using the XRD (Rigaku Ultima-IV) using nickel filter with Cu Kα radiation issuing from a 1.6 kW Rigaku rotating anode generator. Measurements were taken on reflection mode of oriented crystal pellets for step size 0.025^o at scanning rate 10^o per minute. The experimental density (d_{ex}) of the sintered ceramic samples was calculated by the Archimedes method using kerosene oil as the liquid medium. The microstructures of sintered pellets were observed using a Nova Nano SEM/FEI field emission scanning electron microscope (FESEM) as well as the mapping images of the samples was taken. The pellets were allowed for Au coating on the targeted surface by a sputtering unit up to two minutes. This was intended to avoid the accumulation of electrons on the surface of the samples due to electron irradiation during image. The dielectric data at four selected frequencies in a temperature range 25 ^oC – 450 ^oC were taken by using HIOKI IMPEDANCE ANALYZER IM3570 during heating as well as during cooling processes. For electrical measurements, the sintered pellets were coated with silver electrodes and fired at 400°C for 30 min for good adhesion. The furnace was controlled with 2 ^oC rise per minute during the collection of dielectric data. Polarizations vs. electric field (P-E) measurements were performed using precision premier II, a standard ferroelectric testing machine (Radiant Technology). The mixtures were calcined at temperature of 830 °C for 6hrs. The prepared sample for various measurements was sintered at 1030 °C for 3hrs. XRD patterns of the samples were taken by using RIGAKU ULTIMA IV. The FESEM images were taken by Nova Nano SEM/FEI. The impedance data were taken by using HIOKI IMPEDANCE ANALYZER IM3570 within frequency domain of 100Hz and 1MHz and in a temperature range 25 ^oC to 450 ^oC.

4.3. Data analysis

The impedance can be expressed as, $Z = Z' + i\,Z''$, where Z' and Z'' are the real and imaginary impedance values which are derived as $Z' = Z\cos\theta$, and $Z'' = Z\sin\theta$. The value of real (ε') and imaginary part (ε'') of permittivity are derived from the relation $\varepsilon' = \frac{Z''}{Z'^2+Z''^2} \times \frac{1}{\omega Co}$ and $\varepsilon'' = \frac{Z'}{Z'^2+Z''^2} \times \frac{1}{\omega Co}$ where, ω is the angular frequency, C_o is the capacitance of free space and ε_0 is the permittivity of free space (8.854×10^{-12} F/m). The

electric modulus can be expressed as M=M'+iM'' where M'= M cosθ (= $\omega C_o Z''$) and M''= M sinθ (= $\omega C_o Z'$).

4.4. Results and Discussion

4.4.1. Structure and Microstructure analysis

The XRD patterns of all prepared samples are shown in Fig. 4.1. Positions of all the diffraction peaks matches and well indexed to orthorhombic $AgNbO_3$ (JCPDS Card No. 070-4738/ 052-0405) which confirms the formation of required phases. In the modified systems, the position of all the diffraction peaks also matches with the parent one. It is reported that minute traces of secondary phases in $AgNbO_3$ are unavoidable irrespective of synthesis conditions [41].

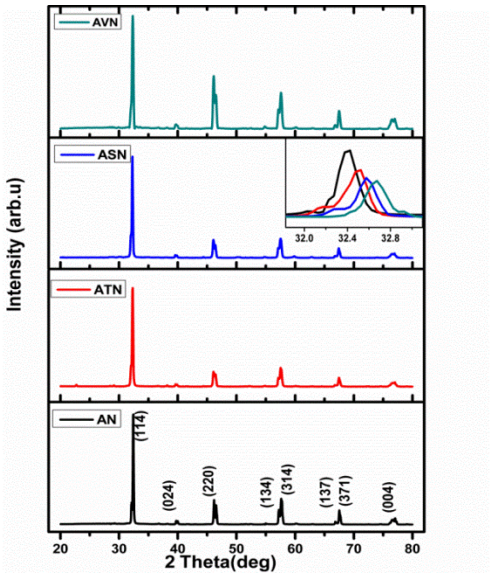

Figure 4.1: XRD images of AN and its modified systems. Inset shows the peak shifting of (114).

The shifting of XRD peak may be due to sintering effect as metal oxides aid in the sintering process or may be due to the fractional substitution of Ta^{5+}, Sb^{5+} and V^{5+} cations in place of Nb^{5+} of ABO_3 structure. But, the surface morphology of the modified systems and evolution of grains which will be discussed next indicates for the partial substitution of cations. The Field emission scanning electron microscopy (FESEM) image of the AN sample illustrated in Fig.4.2, shows distribution of grain size from 1.2µm to 5µm.In the ATN system, the grain size has reduced and the variation ranges from 2 µm to 3 µm. In the ASN system, the variation of grain size ranges from 3 µm to 1.5 nm.

There is no noticeable change in shape of polyhedron grains due to tantalum and antimony substitution in place of niobium in the AN system. But, substitution of vanadium in place of niobium has drastically change the shape and size of the parent system. The polyhedron grains in the AN system changes to cubic or rectangular brick shape with average size ranges from 9.5 µm to 3 µm with small traces of minute grains less than µm. Presence of pores also visible in all the samples with significantly less in the AVN system.

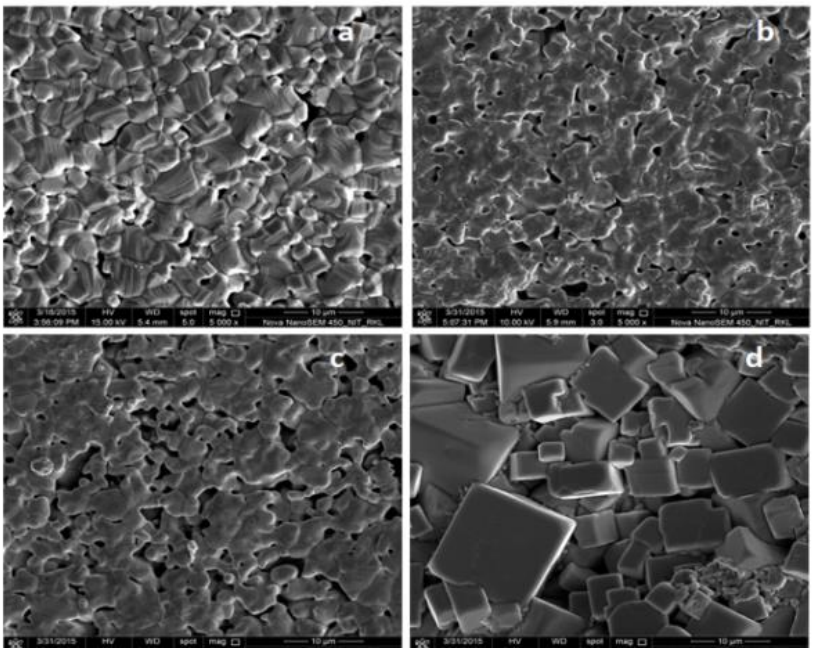

Figure 4.2: FESEM images of AN (a), ATN (b), ASN (c), and AVN (d).

4.4.2. Impedance and Electric modulus study

Complex impedance spectroscopy study is a technique to analyse the electric transport properties of the material. Basically the contribution of microstructures in the electrical properties can be understood. The surface structure contains grains and lattice defects like grain boundaries, pores, cracks, vacancies etc. The conduction of charge carriers, their nature and the activated regions can be assessed by studying the relaxation peaks appeared in different electrical parameters [109-111].

Studying the imaginary part of impedance (Z") and electrical modulus (M") helps a lot to examine the low frequency relaxations. The inability of resolving the multiple relaxations properly within low frequency regime in Z" can be solved in better way in M" as the latter one scales inversely to capacitances. Fig. 4.3 and Fig. 4.4 show selective plots of the (a) impedance (Z"(f)) and (b) electrical modulus (M"(f)) respectively which exhibits relaxation process. In the AN system, a feeble, not properly defined relaxation peak enters through the low frequency window of M"(f) around 345^{o}C which becomes prominent and shifts towards higher frequency side with elevated temperature. The low frequency relaxation also appears in Z"(f) but in a later stage around 375^{o}C and in similar manner shifts towards higher frequency with rising temperature. The relaxation peak enters through low frequency window around 375^{o}C in the ATN system, around 275^{o}C in the ASN system and an early arrival of relaxation appears around 175^{o}C in the AVN system. As temperature elevates, these peaks shift towards the higher frequency end with reduced height.

The dipoles generate due to the separation of cationic and anionic centres which occurs due to the migration of the charge carriers through hopping at vacant sites inside the lattice. The thermal energy possessed by the charge carriers determines the hopping distance as well as the range of frequency for following. Relaxation frequency is the maximum for the charge carriers to conduct in order to bring polarization and beyond which they remain in relaxed state which reduces polarization. This dielectric relaxation occurs at different frequencies for different materials which are dependent to the type of

defect related to the dipoles which may be a physical or chemical defect [90-92, 100-102].

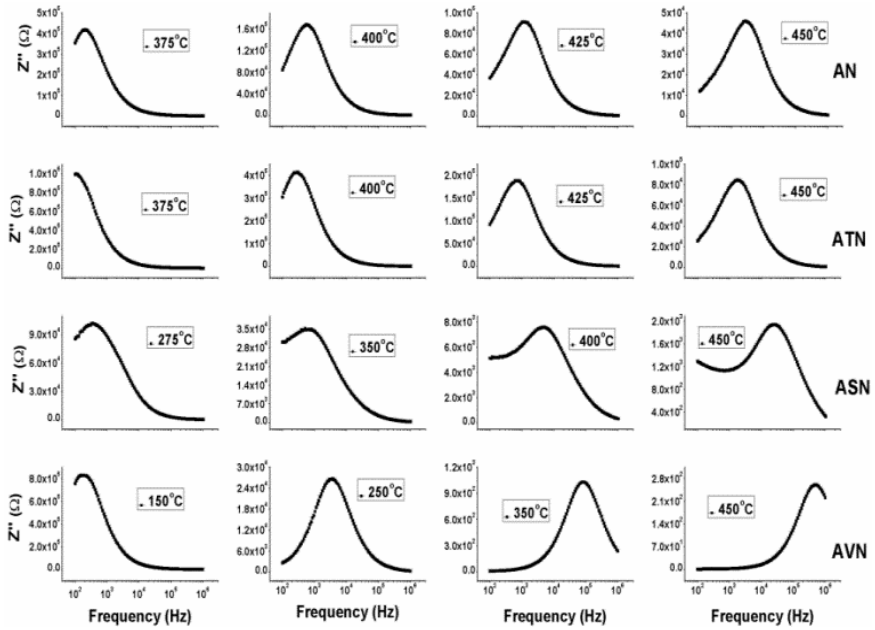

Figure 4.3: Imaginary part of impedance (Z''(f)) of AN, ATN, ASN and AVN systems at selected temperatures.

To verify the presence of multiple relaxation processes such as grain, grain boundary or surface conduction etc., we have investigated the AN bulk system through studying Cole-Cole of impedance (Z' vs. Z'') and electric modulus (M' vs. M'') which are shown in the Fig. 4.5 and Fig. 4.6 respectively. In the AN system, the spike form of Cole-Cole of impedance continues up to 270^{o}C and that indicates the strong insulating nature of the compound. Thereafter, it bends towards abscissa to take the shape of a semi-circular arc around 350^{o}C which signals the beginning of relaxation process [90-92]. Fig. 4.5 illustrates the Cole- Cole semicircles for AN and its modified systems. Within the chosen temperature range, only one semicircle appears. The distinct Cole-Cole semicircles indicate a unique electrical response of a particular region. Sometimes, the resistance of intrinsic and extrinsic conducting regions are not sufficient to resolute the individual conduction process which overlaps giving an asymmetric nature to semicircles. Therefore, Cole-Cole of modulus of all the systems are plotted in Fig. 4.6, which can resolve the electric response due to grain and grain boundary and suppresses the response due to electrode surface conduction effect. In a similar manner, only a single semi-circular arc appears in the Cole-Cole of modulus.

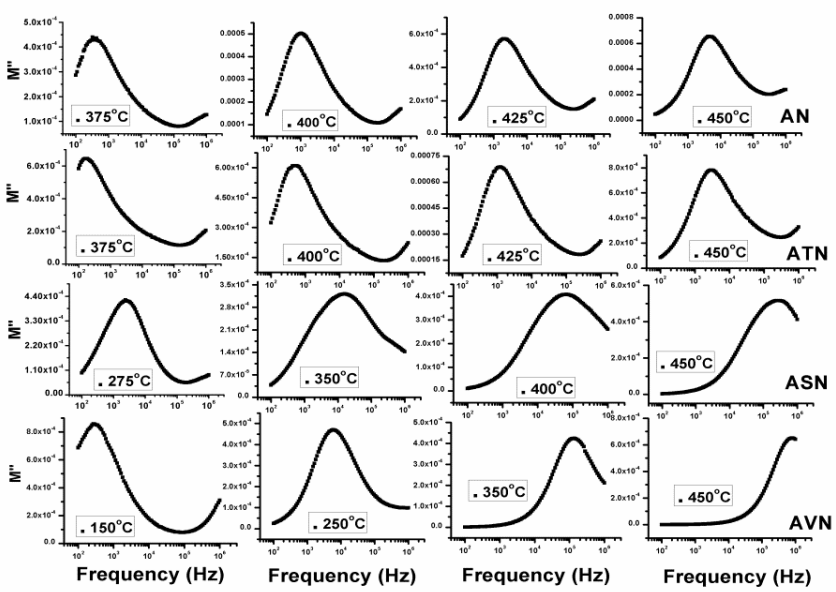

Figure 4.4: Imaginary part of electrical modulus (M''(f)) of AN, ATN, ASN and AVN systems at selected temperatures.

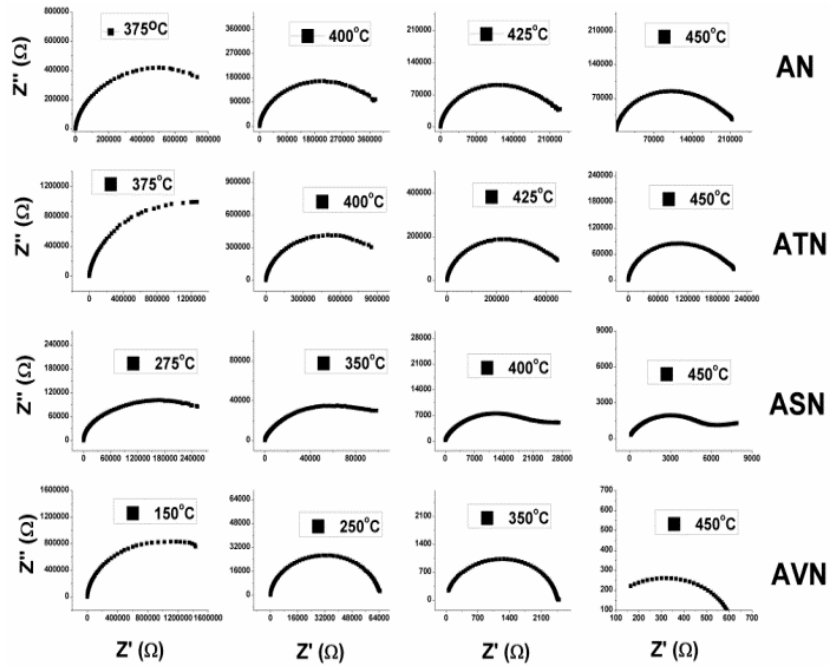

Figure 4.5: Cole-Cole (Z' vs. Z'') plot of AN, ATN, ASN and AVN systems at selected temperatures.

This confirms that a single relaxation process only dominates over the conduction mechanism in all the systems. In general, grain relaxation activates at first which follows by grain boundary and thereafter surface conduction effect. Therefore, we assign the relaxation process is due to the grain conduction effect [90-92]. The radius of the Cole-Cole semicircle which measures the resistance of the material decreases with the increasing temperature.

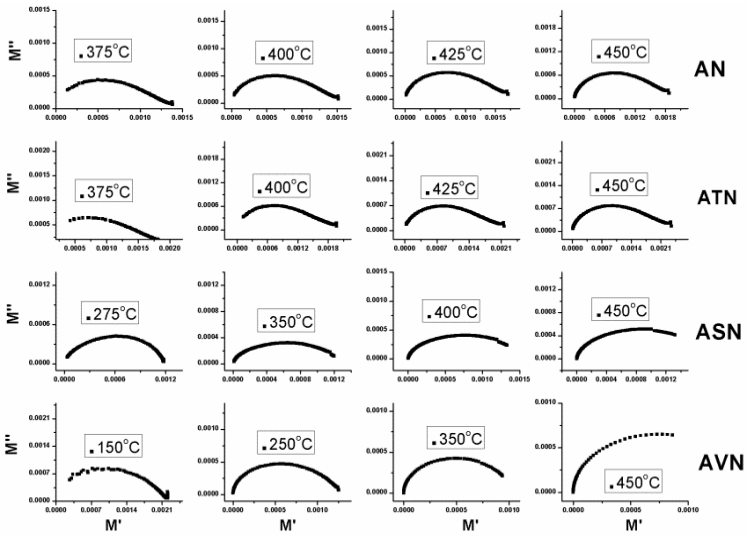

Figure 4.6: Cole-Cole (M' vs. M") plot of AN, ATN, ASN and AVN systems at selected temperatures.

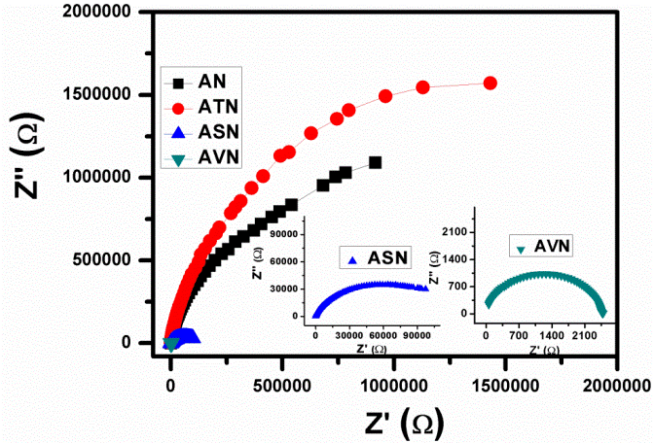

Figure 4.7: Cole-Cole (Z' vs. Z") plot of AN, ATN, ASN and AVN systems at 350 °C.

The centres of the semicircles seem to lie below the abscissa. This suggests for a non-Debye type conduction process [90-92]. Fig. 4.7 illustrates the Cole-Cole semicircle of all the modified systems for comparison at a single temperature (350^{o}C). It is observed that the resistivity of the ATN system has increased significantly. There is a decrease in resistivity in both the ASN and AVN system but a drastic reduction is observed in the latter system. Fig. 4.8 plots the log f_{max} vs. 1/T separately for Z"(f) and M"(f) which indicates the relaxation process is characterised by Arrhenius type behaviour ($f = f_0 \exp(E_a^{rel}/ k_B T)$), where f_0 is the pre-exponential factor and E_a^{rel} represents the activation energy of dielectric relaxations. The activation energies for the parent AN system was calculated to be of 1.36eV and 1.38eV from imaginary part of impedance and electric modulus data respectively. This value is bigger enough to be assigned with the possible grain conduction only [95]. It is observed that substitution of tantalum has enhanced the activation of energy (1.55eV and 1.53eV) whereas substitution of antimony and vanadium has reduced the activation energy given in the Fig. 4.8. It is claimed that such high value of activation energy is liable for the migration of oxygen vacancies.

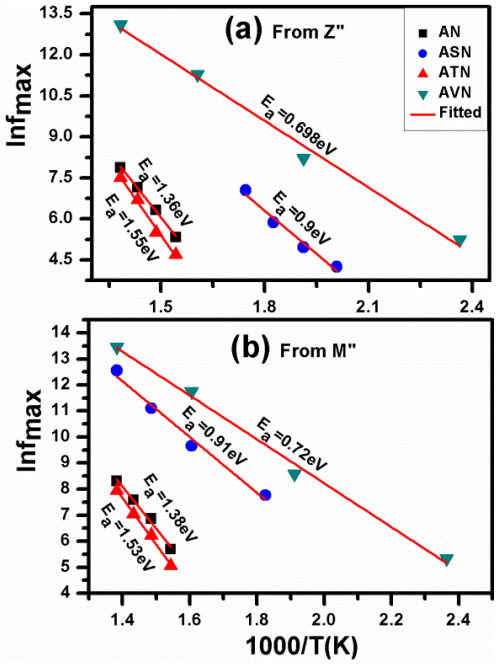

Figure 4.8: Activation energy calculated from the Arrhenius region of Z"(f) (a) and M"(f) (b).

It is established that oxygen vacancies plays a crucial role in the electrical relaxation of perovskite oxides and they affects the dielectric relaxations at high temperatures due to increase in the oxygen vacancy concentration. Tamilselvan *et al.* in their work on Eu-substituted $BiFeO_3$, reported that the decrease in activation energy is related to the suppression of oxygen vacancies [121]. Thus we can assume that tantalum substitution has enhanced the oxygen vacancies whereas antimony and vanadium substitution has suppressed the oxygen vacancies. The enhanced activation energy in the ATN system can be explained due to the increase in resistivity of the modified system. Similarly, decrease in resistivity of the ASN and the AVN system can be responsible for the reduced activation energy of the modified systems. Hence, the early arrival of relaxation behaviour in the AVN and the ASN systems can be related to the reduced activation energy due to the substitution effect.

Table 4.1: Dielectric constant of AN and its modified systems at specified temperatures.

Dielectric Constant (at 10kHz)	AN	ATN	ASN	AVN
At Room Temperature 30^{o}C	171.58	219	600	265.72
Temperature at FE-AFE	330.63 (85^{o}C)	310 (80^{o}C)		354.72 (75^{o}C)
Temperature at AFE-PARA	853.77 (355^{o}C)	645.23 (355^{o}C)		1527.57 (350^{o}C)

4.5. Dielectric and ferroelectric study

Fig. 4.9, Fig. 4.10 and Fig. 4.11 plot the temperature dependent permittivity (ε) at different frequencies for the AN system in comparison with the ATN, ASN and AVN systems respectively. Four major dielectric anomalies at $T_C^{FE} \approx 85°C$ ($M_1 \leftrightarrow M_2$), 270°C ($M_2 \leftrightarrow M_3$), $T_C^{AFE} \approx 350°C$ ($M_3 \leftrightarrow O_1$) and 386°C ($O_1 \leftrightarrow O_2$) are observed in our prepared sample which matches mostly to the earlier reports where M_1 region is ferroelectric (FE), M_2 and M_3 regions are antiferroelectric (AFE) and finally O_1, O_2 are in paraelectric state (PE) [42-44]. However, the transition temperature for T_C^{FE} is reported to be around 67°C to 70°C is somehow appears at little higher. In a recent study, *Kania et al.* reported that particularly, T_C^{FE} peak varies with the concentration of Ag^{1+} ion [45].

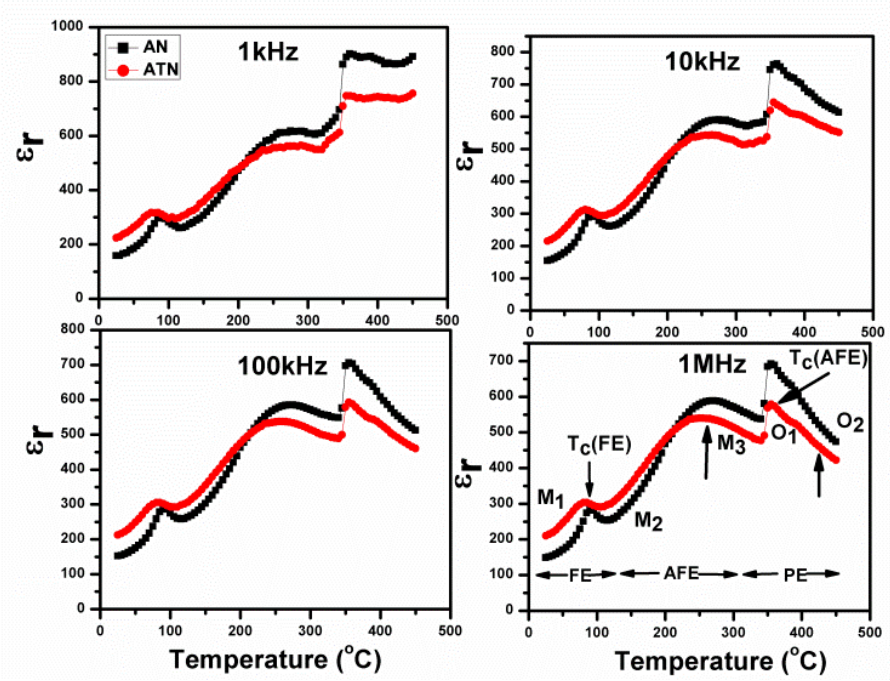

Figure 4.9: Temperature dependent relative permittivity plot of AN and ATN systems at different frequencies.

The plot shows that the nature and shape of the temperature dependent permittivity of ATN and AVN systems matches to that of the parent AN system where as in ASN system the feature has completely changed. The multiple dielectric anomalies appeared in the AN system also clearly visible in the ATN and AVN systems whereas in the ASN system, the corresponding transition points are not properly distinguished. The low temperature dielectric anomaly which is related to ferroelectric to antiferroelectric transition is disappeared in the ASN system. There is no such noticeable shift of the Curie temperature for AFE to PE transition point in ATN and AVN systems though low temperature dielectric anomaly slightly shifts to lower value. The increasing figure of real permittivity is observed in both the ASN and AVN systems but high enhanced value is seen in the former system. In the ATN system, the ε(T) divides into two regions: (i) below broad dielectric anomaly ($M_2 \leftrightarrow M_3$), the permittivity value of the ATN system is higher than the AN system, (ii) at and above the Curie temperature the permittivity of the ATN system is lesser than the parent system. The values of relative permittivity of the modified systems are listed in the table. 4.1. The variation of the dielectric loss with temperature of the systems under study at different frequencies is plotted in Fig. 4.12. Tantalum substitution

in place of niobium has reduced the dielectric loss value whereas substitution of antimony has marginally increased the figure of the modified systems in comparison to parent system. But, the vanadium substitution has resulted an unpredictable increase in dielectric loss and particularly, at low frequencies.

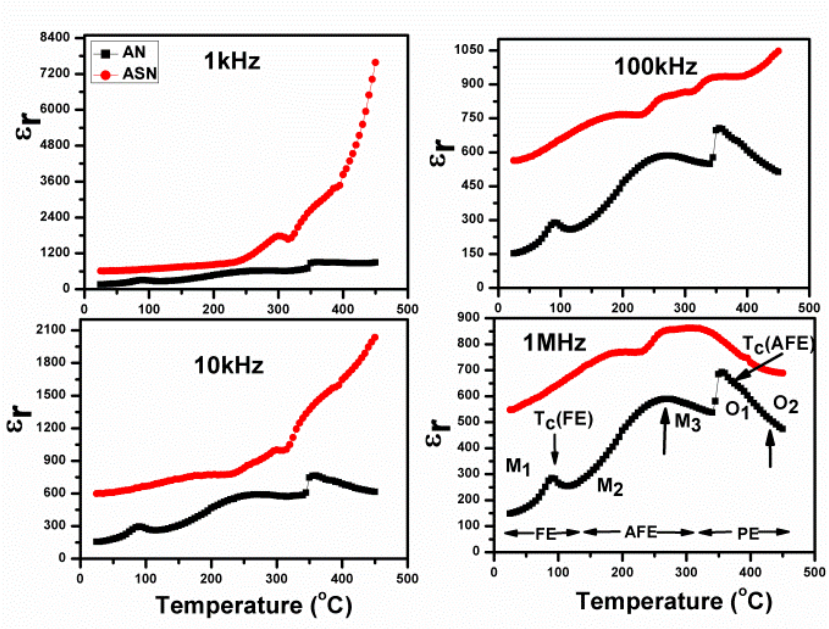

Figure 4.10: Temperature dependent relative permittivity plot of AN and ASN systems at different frequencies.

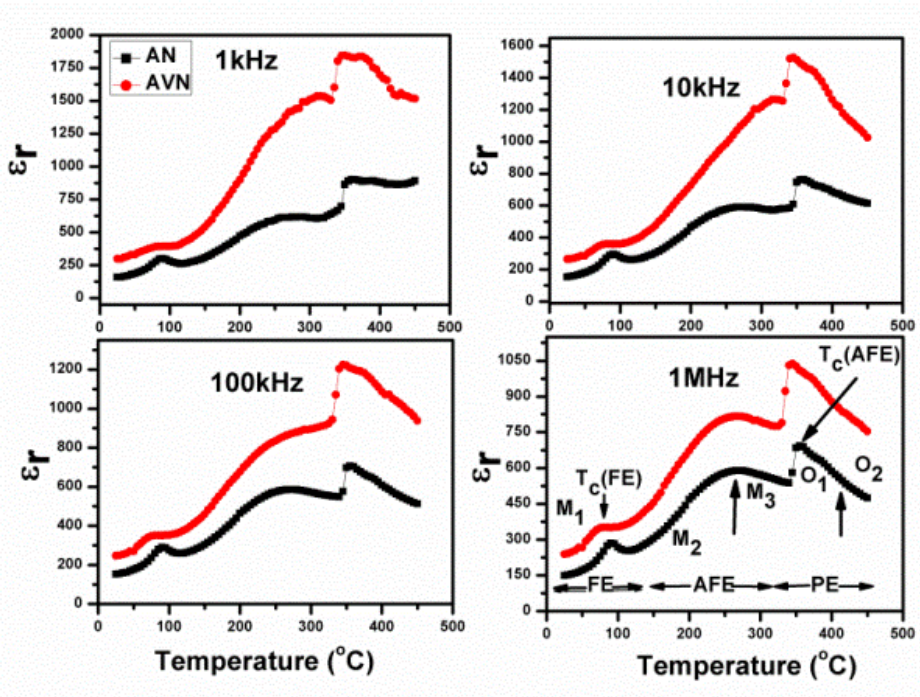

Figure 4.11: Temperature dependent relative permittivity plot of AN and AVN systems at different frequencies.

In addition with, the hysteresis loop plotted in Fig. 4.13 also shows the low remnant polarisation value which also matches to the earlier reports. All the samples shows P-E

hysteresis loop at room temperature. The value of saturation polarisation (P_s) and remnant polarisation (P_r) are provided in the table 4.2. A slim unsaturated hysteresis loop of small P_r and P_s values are observed in the parent AN system. In ATN system, the hysteresis loop appears with little change in polarisation values having utmost equal shape of loop. In ASN system, simply a loop appears for low applied voltage of 10kV and evolves to attain saturation for applied 20kV. In AVN system, a proper hysteresis loop with comparatively magnified polarisation value is observed.

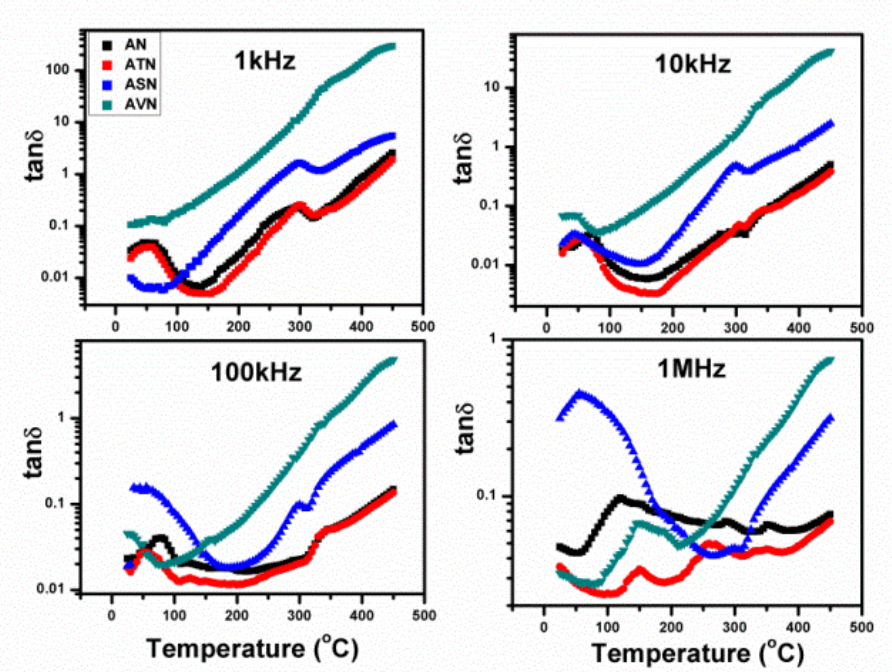

Figure 4.12: Temperature dependent dielectric loss of plot of AN, ATN, ASN and AVN system at different frequencies.

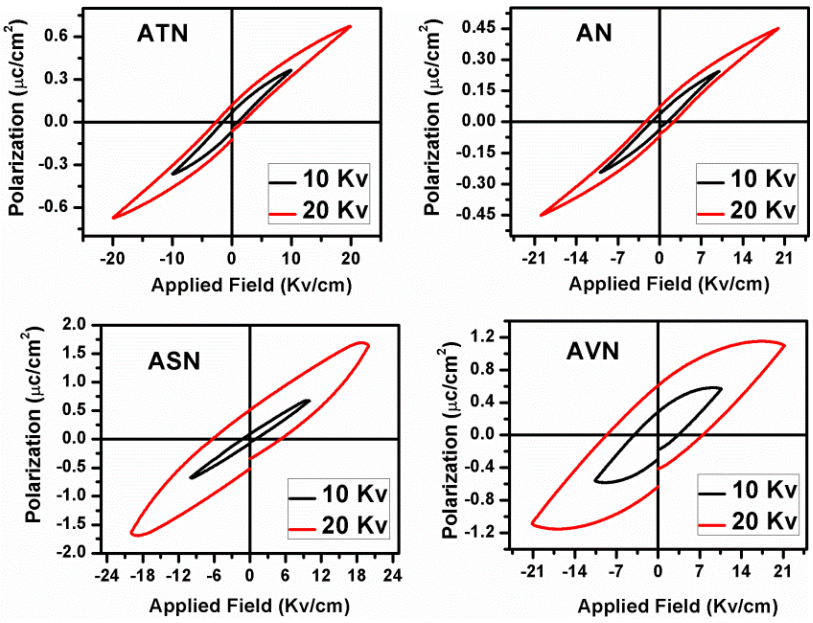

Figure 4.13: P-E hysteresis loop of AN, ATN, ASN and AVN system for 10kV & 20kV of applied field.

Table 4.2: Ferroelectric parameters of AN and its modified systems at room temperature.

Applied Filed	Saturation & Remnant Polarization (μC/cm^2)	AN	ATN	ASN	AVN
10Kv	P_{max}	0.24	0.36	0.68	0.57
	P_r	0.03	0.06	0.09	0.28
20Kv	P_{max}	0.44	0.67	1.69	1.14
	P_r	0.06	0.11	0.51	0.60

The increase in permittivity particularly at Curie temperature and saturation polarisation observed in ASN and AVN system suggests for the generation of any additional polarisation mechanism i.e. increase in any net dipole moment. It is well known that ferroelectric phase is essentially the cooperative phenomena which is stabilised by the long range coulomb interaction of electric dipole moments that appears spontaneously in each cell [63]. The most relevant microscopic parameters which influence the modifications are atomic or ionic radii, lattice parameters of the compound, ionicity and covalency of the bonds, local potentials, polarisabilities of the ions and bonds, nature and concentrations of the introduced defects [63]. It is established that the dielectric materials with high permittivity are linked to the BO_6 octahedra joined to each other at their top [88, 126-128]. The cation located at the centre of the octahedra plays the crucial role in dominating their dielectric properties. In our perovskite oxide $AgNbO_3$, for the radius Sb^{5+}(0.62Å) and V^{5+}(0.58Å) being smaller to Nb^{5+}(0.69Å), when a little of Nb cation at B-site is substituted by the Sb^{5+} and V^{5+} ions the correlation of NbO_6 is intensified and that results in the increase in permittivity of the modified ASN and AVN systems. Again, it is also verified that the incorporation of smaller cations in place of larger cation in BO_6 octahedra increases the rattling space for cation movement [126-128]. This leads to enhanced ferroelectricity in the ASN and AVN systems. The approximately equal ionic radius of Nb^{5+} (0.68Å) to that of Nb^{5+} may be failed in increasing the rattling space in the ATN system which leads to poor enhancement in polarisability. The Curie temperature mostly depends upon the bond strength of A-O/B-O ion pairs. If the substituted cation is of lower bond energy then the Curie temperature will shift towards lower values and vice versa. It is calculated by Ogawa *et al* that the covalent bond strength of Sb-O, Ta-O are comparatively higher to Nb-O bond strength [129, 130]. Hence minute substitution of Sb and Ta in place of Nb will not bring any significant change within NbO_6 octahedra and hence no changes in the Curie temperature are observed in the modified systems. In the previous literature on $AgNbO_3$ modified with Ta, it is reported that the Curie temperature for antiferro to paraelectric phase is not affected by the substitution however; the shifting of broad phase ($M_2 \leftrightarrow M_3$) transition point towards lower temperature is observed which is verified due to the lowering of Nb concentration which is also matching to our result [64, 67]. We can expect that the V-O bond is also strong covalent in nature which may be the reason for not shifting of Curie temperature in the AVN system.

There are several factors which are responsible for loss in dielectric materials can be classified into two classes: (a) intrinsic loss and (b) extrinsic loss. The intrinsic loss arises from the anharmonic phonon decay process in pure crystal lattice whereas the extrinsic loss finds its source from crystal defects, grain boundaries, secondary phases and pores [126-128]. As it is verified that in the chosen temperature and frequency range the intrinsic grain conduction dominates over the extrinsic interfacial conduction therefore, the behaviour of dielectric loss can be supposed to be of intrinsic *i.e.* intra grain in nature. In this respect we can relate the changing grain size to the dielectric loss of the modified

system. As there is no noticeable change in shape and size of grain size in ATN and ASN system therefore, the variation dielectric loss is very close to parent AN system. But, the drastic increase in grain size and change in shape of grains in the AVN system might have increased the dielectric loss to significantly high.

4.6. Conclusion

The 0.1 mole of isovalent (Ta_2O_5, Sb_2O_5 and V_2O_5) substituted $AgNbO_3$ systems were prepared by conventional solid state route. From the impedance spectroscopic analysis only intrinsic (grain) conduction was found to be the dominant feature in the modified systems. The appearance of low temperature relaxations were related to the reduced activation energy in the systems. The decrease in resistance by order in the modified systems was supposed to be the cause for reduced activation energy. The surface morphology of the AVN system was seen a drastic change in its shape and size and was related to its improved dielectric, ferroelectric as well as high dielectric loss.

Chapter 5

Dielectric, ferroelectric and impedance spectroscopic studies of MnO_2-doped $AgNbO_3$ ceramic

5.1 Introduction

Materials, used in the dielectric resonator applications, should have high dielectric constant (ε) and moderate loss (tanδ) in the microwave frequency range. Recent studies in AN based materials have shown the potential of this system for the dielectric resonator applications. AN system has distorted perovskite structure at room temperature (RT) and shows six reversible phase transitions, linked to structural transformation, and confirmed by the 'ε' vs. temperature study. In the AN system, there exists a complicated coupling between the NbO_6 octahedral tilting and the local displacements of both the Ag and Nb atoms. This lead to a series of changes in the cation displacements throughout the M – phases (M_1, M_2, M_3). Octahedral rotation is present for all the M - phase and influences transitions between them and evolution of polar state. Yashima *et al*. have successfully proposed the non-centrosymmetric $Pmc2_1$ space group over centrosymmetric Pbcm to explain the polar nature of M_1 phase [57-61]. Yashima *et al*. have verified the displacement of atoms in ferrielectric order in $AgNbO_3$ lattice, which is an extremely rare case in ferroelectric materials, that results net spontaneous polarisation [59]. M_1 is a polar phase in which cations are arranged along the observed ferroelectric (FE) order but the weak ferroelectricity is due to the blocking of Ag off-centering due to the excess octahedral rotation. $M_2 \leftrightarrow M_3$ is a broad phase transition in which the cations arrange in antiferroelectric (AFE) order and attributed to the dynamics of Nb atoms in the AN system. A sharp phase transition occurs at $M_3 \leftrightarrow O_1$ and is reported as the Curie point (T_C) as O_1 phase shows the paraelectric (PE) behaviour. The low tolerance factor (t = 0.956) in the AN system is responsible for the excess NbO_6 octahedral rotation during the phase transition. This obstructs the Ag atoms displacement as well as force its dynamic in antiferroelectric order in the AN system [55, 56]. By suitable modification in the AN system, a chemical pressure can be build up for suppressing the octahedral rotation by increasing the tolerance factor, which may recover the Ag atoms off centering behaviour and enhance ferroelectricity. *Kania et al.* have reported the enhanced ferroelectric behaviour at RT in the $Ag_{1-x}Li_xNbO_3$ for $x < 0.06$ mole [71]. But, *Fu et al.* `have reported reduced ferroelectricity as well as reduced dielectric behaviour in the $Ag_{1-x}K_xNbO_3$ system for $x \leq 0.07$ mole [74]. In first principle calculations, effects of carrier generated by photoinduced doping in $SrTiO_3$, *Uchida et al.* have reported that the doping of hole and electron can control the octahedral rotation, which affects ferroelectric instability [35]. In this present work, the effect of hole as charge carriers doping on the electrical properties of the $AgNbO_3$ system is carried out. Heterovalent Mn^{4+}(r = 0.53 Å) ions were incorporated at the Nb^{5+}(r = 0.69 Å) ions site to create hole in the modified AN system.

For this purpose, 0.02 and 0.04 moles of MnO_2were substituted in place of Nb_2O_5 to prepare $AgNbO_3$ modified with MnO_2 systems. The effect of hole doping (Mn^{4+}, Mn^{3+}), the presence of Jahn-Teller active cation Mn^{3+} ($3d^3$), electronegativity of Mn (1.55) on the dielectric and ferroelectric properties of the modified systems were observed, analysed and discussed in detail. Along with this, the contribution of microstructures like intrinsic (grain) or extrinsic (grain boundary, sample-electrode surface contact etc.) parameters to conduction mechanism also investigated by complex impedance spectroscopy technique.

5.2 Experimental Details

$AgNbO_3/MnO_2$ (AMN), and AN ceramic samples were synthesized by solid state reaction route. Ag_2O, Nb_2O_5 and MnO_2, were used as the starting raw precursors and mixed stochiometrically. The amount of MnO_2 was taken inlow molar concentration (0.02, 0.04) of Nb_2O_5 in order to incorporate Mn^{4+} in place of Nb^{5+} cation at B-site of the perovskite structure. The systems are named as AMN2 and AMN4 respectively. Extra 3 wt% Ag_2O was added to the mixture in order to meet the silver loss due to its volatility [41, 58]. After two hours of manual grinding, the properly mixed powders were kept in an alumina crucible for calcination at 830 °C for 6h in air. The calcined powders were mixed with 3 wt% polyvinyl alcohol (PVA) solution with proper milling and uniaxially pressed into disks of diameter ~10 mm and a thickness ~ 1 mm using hydraulic press under ~70 MPa pressure. The prepared pellets were kept over an alumina plate for sintering at 1030 °C for 3h in normal atmospheric condition. The pale yellow colour pellet of AN, dark brown colour pellet of AMN was collected after sintering. X-ray diffractograms of all the compositions were investigated by using the XRD (Rigaku Ultima-IV) using nickel filter with Cu Kα radiation issuing from a 1.6 kW Rigaku rotating anode generator. Measurements were taken on reflection mode of oriented crystal pellets for step size 0.025^o at scanning rate 10^o per minute. The microstructures of sintered pellets were observed using a Nova Nano SEM/FEI field emission scanning electron microscope (FESEM) as well as the mapping images of the samples was taken. The pellets were allowed for Au coating on the targeted surface by a sputtering unit up to two minutes. This was intended to avoid the accumulation of electrons on the surface of the samples due to electron irradiation during image. The impedance data were collected within 100 Hz to 1 MHz, in a temperature range 25 ^oC – 450 ^oC by using HIOKI IMPEDANCE ANALYZER IM3570. The data were collected during both heating as well as cooling processes. For electrical measurements, the sintered pellets were coated with silver electrodes and fired at 400°C for 30 min for good adhesion. The furnace was controlled with 2^oC rise per minute during the collection of dielectric data. Polarizations vs. electric field (P-E) measurements were performed using precision premier II, a standard ferroelectric testing machine (Radiant Technology). X-ray photo electron spectroscopy was taken to examine the oxidation states of the incorporated dopant *i.e.* manganese and other existing elements such as silver, niobium and oxygen. The data were obtained by using Thermo ESCALAB 250 physical electronics photoelectron spectrometer having Al Kα X-ray (1486.6 eV) as exciting radiation. The binding energy was determined by reference to the C 1s line at 284.8 eV.

5.3 Results

5.3.1 XRD, SEM, XPS and Raman spectroscopy Study

The XRD patterns of the AN and MnO_2–doped AN samples are shown in the Fig. 5.1. The position of the peaks is found to be matching to the orthorhombic structure of $AgNbO_3$ system as per the JCPDS Card No. 070-4738 and are indexed accordingly. Minute traces of impurity secondary phases are also identified in the diffraction pattern which is reported as unavoidable in the compound irrespective of synthesis route [41]. The little shifting of XRD peak position in the modified systems indicates the partial incorporation of Mn in place of Nb in $AgNbO_3$ ceramic. The lattice parameters of all the systems are calculated and put in the Table 5.1.

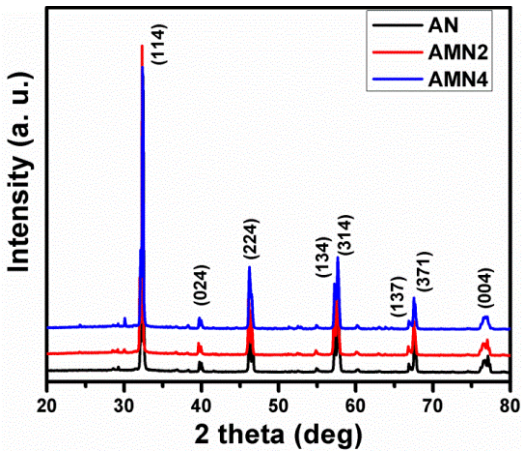

Figure 5.1:X-Ray diffraction pattern of the AN and its modified systems.

Table 5.1:Lattice parameters calculated by using check cell software.

Compound→ / Lattice Constant↓	AN	AMN2	AMN4
a (Å)	3.9541	3.9592	3.9523
b (Å)	3.9002	3.8988	3.8988
c (Å)	3.9331	3.9362	3.9362

Fig.5. 2 shows the FESEM images of the parent and its modified systems. It is observed that the non-uniformity of the grain size distribution increases in the modified systems. The size of the grains in the AN system is of ~2 µm. However, the size distribution ranges ~1.5 µm to ~5 µm. the polyhedron shape of the AN grain remains to some extent identical to that of the AMN systems. The amount of the surface pores appears in the AN system also reduces in the AMN systems. Experimental density ~91%, 91.35% and 92% of theoretical density are obtained of sintered AN, AMN2 and AMN4 ceramic samples, respectively.

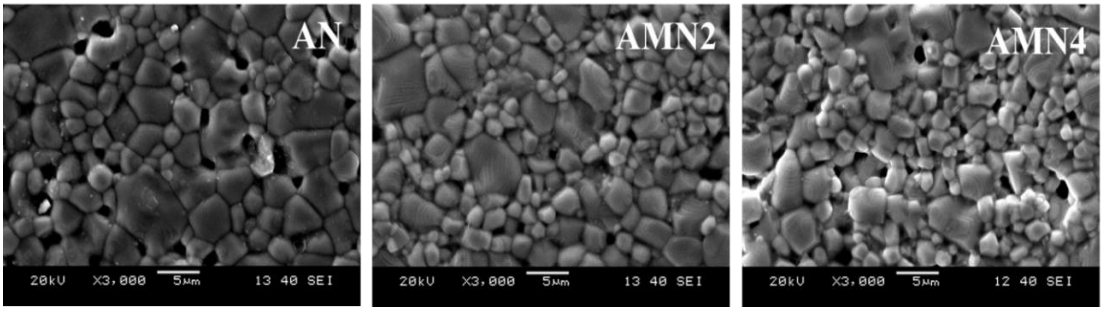

Figure 5.2 (a): FESEM images of the AN, AMN2 and AMN4 systems.

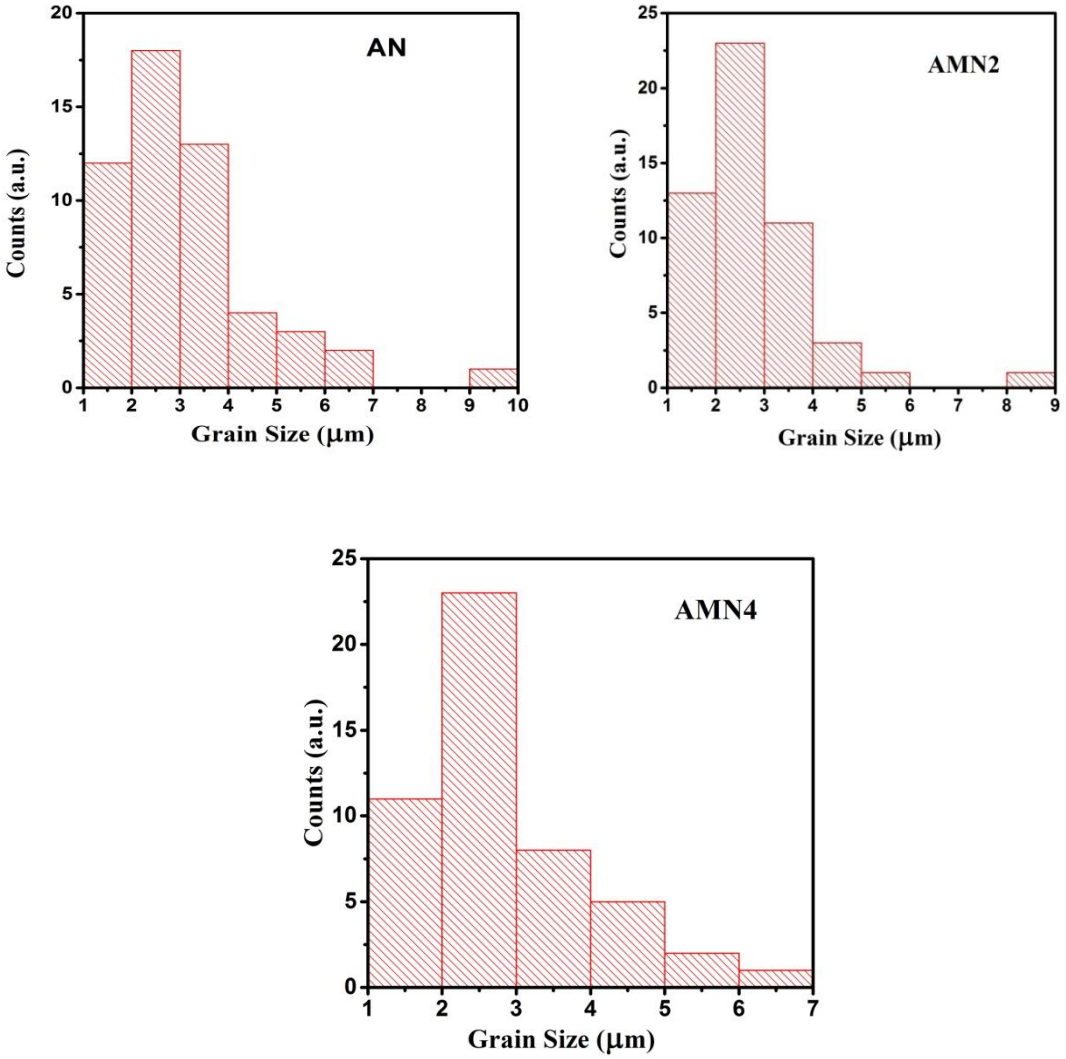

Figure 5.2 (b): histogram showing the particle size distribution of the systems.

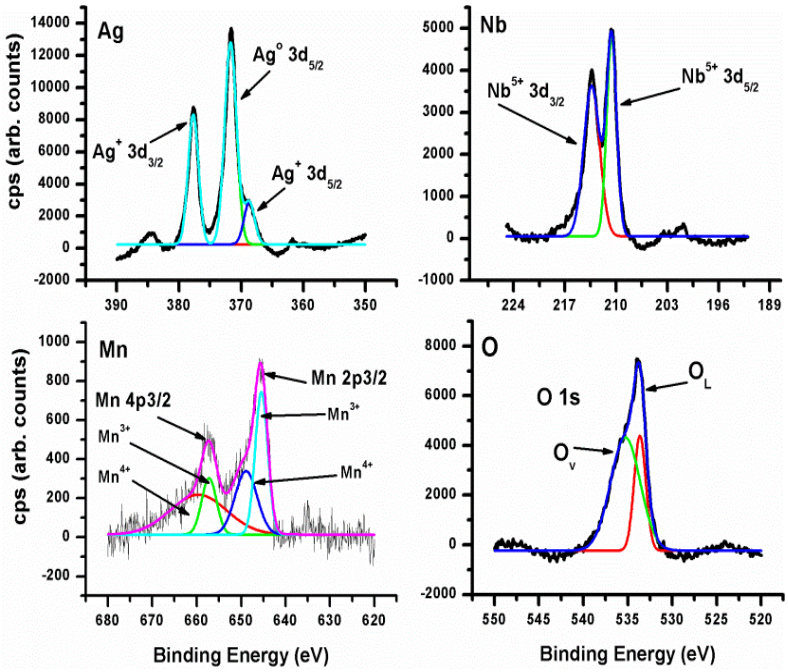

Figure 5.3: X-ray photoelectron spectroscopy images of the AMN system showing the possible oxidation states of the constituent elements.

XPS data is very much relevant to identify the oxidation states of the constituent elements in a compound. Fig. 5.3 illustrates the XPS data of the AN, AMN2 and AMN4 systems. The binding energy corresponds to the position of all identified peaks confirm the presence of major constituents like silver in Ag^{1+} state, niobium in Nb^{5+} state and oxygen in O^{2-} state. The peaks associated to the minute constituent element i.e. manganese is also examined to be existing in Mn^{3+}, Mn^{4+} states which confirms that hole doping was in the modified systems. In addition to this Mn^{3+} ($3d^3$) is a Jahn-Teller active ion which was confirmed to be present at the oxygen octahedral site. All the identifications are carried out by cross checking the previous literatures [54, 115, 131].

Raman spectra provide important information regarding the internal vibration in the crystal lattice. Fig. 5.4 shows the different vibrational modes obtained in our prepared sample of the parent AN and its modified system which agrees well with the previous reported data. It is observed that all the internal vibrations related to NbO_6 octahedra lies within 160 cm^{-1} to 900 cm^{-1}. Around the region 170 cm^{-1} to 325 cm^{-1}, the first intense mode is observed which is splitted and corresponds to the degenerated modes assigned as υ_6 and υ_5 respectively. The modes ~ 360 cm^{-1} and ~ 420 cm^{-1} are of low intensity which are assigned as υ_4 and is supposed to be the associate bending modes of Nb-O-Nb bonds. The possible cause for this low intensity is due to the low tilting angle between the adjacent NbO6 octahedra. The second intense mode appears ~ 575 cm^{-1} – 610 cm^{-1} with a shoulder ~ 525 cm^{-1} – 575 $cm^{-1}$are assigned as υ_1 and υ_2 respectively. These modes are supposed to be arised due to the symmetric stretching of The NbO_6 octahedra which corresponds to different Nb-O bond lengths. Due to the partial incorporation of manganese in place of niobium it is observed that the two intense modes have slightly shifted towards low wave number side [113, 114].

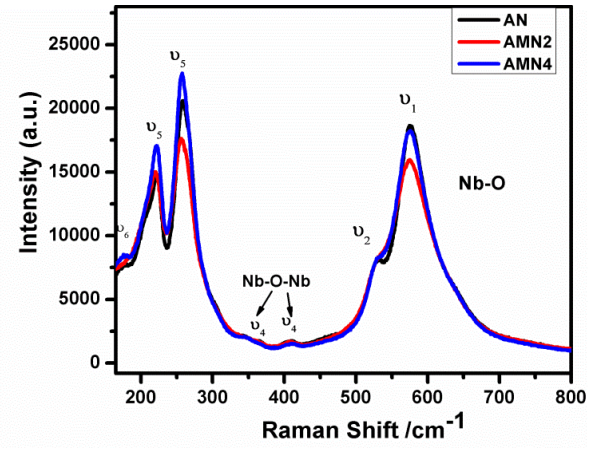

Figure 5.4: Raman spectra of the AN and modified systems showing the possible vibrational modes of the systems.

5.4 Dielectric study

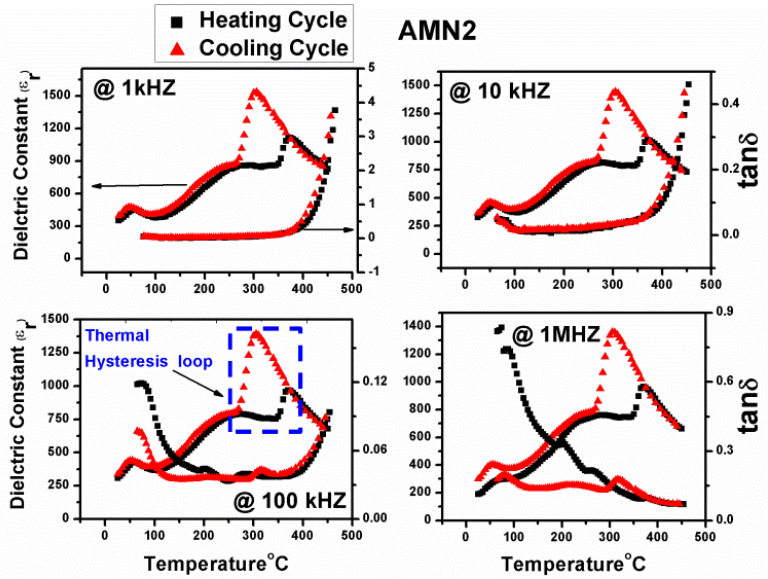

Figure 5.5: Temperature dependent relative permittivity and tangent loss of the AMN2 systems at selected frequency. The heating and cooling cycles with the thermal hysteresis are also shown at different layers.

Fig. 5.5 and Fig. 5.6 illustrate the diagram of the temperature dependent dielectric constant (ε) and loss (tanδ) at four selected frequencies during both the heating as well as cooling cycle for the AMN2 and AMN4 systems respectively. Three dielectric anomalies are clearly observable in both the modified systems. For the AMN2 system dielectric anomalies appears at T_C^{FE} ~ 62°C ($M_1 \leftrightarrow M_2$), ~277°C ($M_2 \leftrightarrow M_3$) and T_C^{AFE} ~369°C ($M_3 \leftrightarrow O_1$). Similarly for the AMN4 system, dielectric anomalies appears T_C^{FE} ~ 61°C ($M_1 \leftrightarrow M_2$), ~256°C ($M_2 \leftrightarrow M_3$) and T_C^{AFE} ~356°C ($M_3 \leftrightarrow O_1$). The small dielectric anomaly of ($O_1 \leftrightarrow O_2$) is not properly visible in both the systems. A minute hump type feature also appears in between$M_2 \leftrightarrow M_3$ during cooling cycle. The thermal hysteresis is also observed at T_C^{AFE} and the hysteresis region of AMN2 systems is found to be wider than AMN4 system. The position of all the dielectric anomalies, nature and shape of the above plots match to the earlier reported values and hence this confirms that the prepared samples are of good quality. It is observed that the doping of hole into the AN system by

incorporating Mn^{4+}, Mn^{3+} etc. has improved the dielectric values quite significantly. There is a little shifting of T_C^{FE} towards the low temperature whereas absolutely no shifting is observed in T_C^{AFE} value in the modified systems. In the AMN4 system, a new phase transition type picture appears in between broad and sharp dielectric anomaly. It is interesting to note that though dielectric constant has increased by a steady figure but there are no such big changes in the dielectric loss of the modified systems.

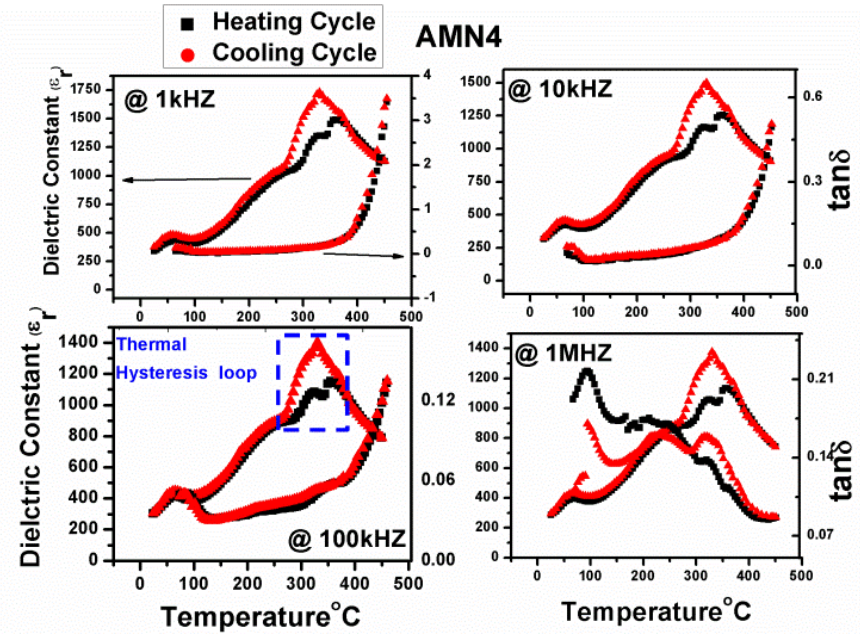

Figure 5.6: Temperature dependent relative permittivity and tangent loss of the AMN4 system at selected frequency. The heating and cooling cycles with the thermal hysteresis are also shown at different layers.

5.5 Ferroelectric study.

Fig. 5.7 shows the polarisation versus electric field (P-E) hysteresis loops at RT of the AN based ceramic samples. We observe an improvement in the ferroelectric parameters after the modification by hole doping into the AN systems. An unsaturated slim P-E hysteresis loop of P_r ~0.037 μC/cm^2, P_{max} ~ 0.24 μC/cm^2 is observed for the AN ceramic samples. For the AMN2 ceramic sample P_r ~0.04 μC/cm^2 and P_{max} ~ 0.41 μC/cm^2 and for the AMN4 ceramic sample, P_r ~0.16 μC/cm^2 and P_{max} ~ 0.52 μC/cm^2 were observed. In both the AMN2 and AMN4 ceramic samples an enhancement in saturation polarisation than the parent AN system is observed.

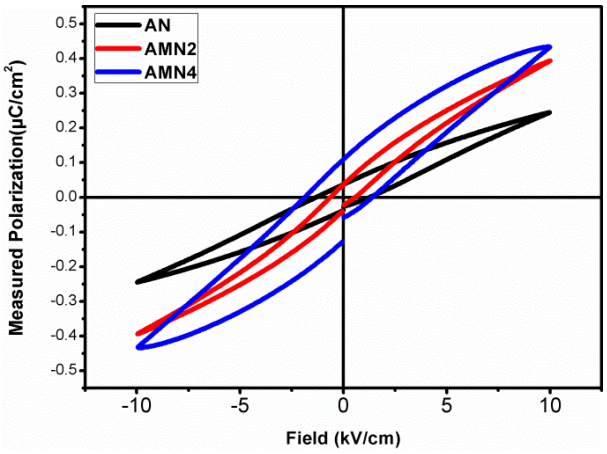

Figure 5.7: P-E hysteresis loop of the AN, AMN2 and AMN4 systems for 10kV of applied field.

Table 5.2: Ferroelectric parameters of the AN and its modified systems.

Applied Filed	Saturation & Remnant Polarization ($\mu C/cm^2$)	AN	AMN2	AMN4
10Kv	P_{max}	0.245	0.394	0.434
	P_r	0.035	0.036	0.109

5.6 Discussion of the results.

Porosity, grain size, impurities have a significant role in determining the electrical properties of ceramic samples. The reduced amount of pores in the AMN systems can be related with their enhanced dielectric and ferroelectric properties. But in the present study, charge carriers (holes in case of Mn^{4+} doping) are created in the AMN systems and its effect cannot be ignored. Though, theoretical work carried out by K. Uchida *et al.* relate with the $SrTiO_3$ system but the effect of carrier doping on BO_6 octahedral rotation may be considered as universal. Generally, carrier doping in an oxide system creates variation in ionic radii as well as in tolerance factor, which can control the octahedral rotation and it is theoretically verified that the doping of reduces the octahedral tilting [35]. Since, the doped holes in an oxide system occupies top of the valence band with oxygen 2p orbital, but in AN system, the top of the valence band consists mostly of oxygen 2p and to some extent 4d orbitals of Ag atoms [56, 132]. It is reported that the doping of holes in a perovskite system increases the tolerance factor, which can ultimately suppress the octahedral rotation [30]. Therefore, in the $AgNbO_3$ system, the bottom of the conduction band consists of 4d orbitals of the Nb atoms. Earlier it is reported that the doping of holes or electrons in a material suppresses the ferroelectricity [35]. However, in the present study an enhancement of ferroelectricity is observed in both the AMN systems. Manganese mostly exists in Mn^{3+}, Mn^{4+} oxidation states in a compound which is confirmed from the XPS data and hence may create holes when substituted at Nb sites in the AN system. In $AgNbO_3$ system, the excess octahedral tilting locks the Ag off-centering and is the main responsible cause for the weak ferroelectricity. As doping of holes suppresses the octahedral rotation this may unlock the off-centering behaviour of the Ag which may lead to an increase of the dipole moments and increase in ferroelectricity in AMN systems. Again, the most relevant microscopic parameters which

influence the modifications are atomic or ionic radii, lattice parameters of the compound, ionicity and covalency of the bonds, local potentials, polarisabilities of the ions and bonds, nature and concentrations of the introduced defects like vacancy and interstitial ions [63]. Variation in lattice parameters and shifting of the XRD peaks indicates the introduction of lattice distortion in the modified systems. These lattice distortions can create additional dipole moments in respective unit cell and help in enhancing the polarisation of the system. It is well known that ferroelectric phase is essentially the cooperative phenomena which is stabilised by the long range columbic interactions of the electric dipole moments and appears spontaneously in each unit cell [63]. In addition, another explanation can be given on the basis of electronegativity, ionicity and covalency of the bonds. According to Pauling scale, the electronegativity of Mn is 1.55 and that of Nb is 1.6 and therefore, when Mn is substituted in place of Nb, the electronegativity difference between the Nb and O (3.44) increases. The increasing difference in electronegativity between metal and oxygen also increases the ionicity of the bonds. It is an established fact that ionicity of a bond relates to its polar character whereas covalency of the bond relates to its non-polar character. The increasing ionicity of the bonds makes them more polar in nature. Again, from the XPS result, it is confirmed that manganese exists in Mn^{3+} ($3d^3$) and Mn^{4+} ($3d^4$) states. Between these two states, Mn^{3+} ($3d^3$) are a Jahn-Teller active ion and hence it can favour a Jahn-Teller type of distortion within its octahedral site. If we observe at the evolution of P-E loops in the modified systems then one can notice that the remnant polarisation (P_r, zero applied field) of AMN4 system is comparatively larger (~ twice that of AN) than that of AMN2 (P_r value is very close to AN). However, at highest applied field (10kV/cm), the improvement in polarisation value is well observed for both the modified systems. This indicates that the distortion due to octahedral tilting/rotation has reduced to some extent. Though several possible explanations are there but the significant improvement of P_r value for AMN4 system indicates that the Jahn-Teller distortion dominates over other factors with the increase in the concentration of Jahn-Teller active Mn^{3+} cation in the modified systems. Therefore, it can be argued that the incorporation of Mn into the $AgNbO_3$ system increases its ionicity due to which its polarisation increases, which completely matches with our experimental results.

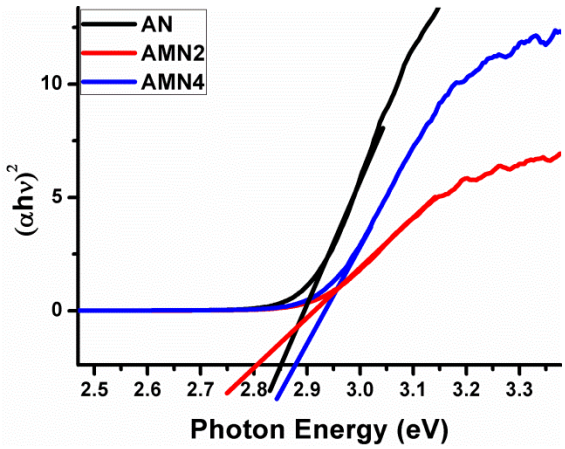

Figure 5.8: Band gap calculated from UV-spectra of AN and its modified systems.

It is earlier discussed in the introduction part that if the distortion in the perovskite structure reduces then it will widen the energy gap between valence band and conduction band [1, 30]. Fig. 5.8 illustrates the UV spectroscopy of the AN and AMN systems. It is observed that the band gap of AMN4 system has increased by some value than the AN system. This indicates that in the AMN4 system the structural distortion due to octahedral tilting/rotation is reduced and which is most probably due to the dominance of Jahn-Teller distortion over other possible factors.

The increase in dielectric constants in the AMN systems can be related to the net increase in polarisation of the systems. In the AMN systems, T_C^{FE} decreases but T_C^{AFE} increases slightly, which is similar to $Ag_{1-x}Li_xNbO_3$ system, reported earlier. This behaviour can be explained on the basis of development of internal and external stresses, arising due to the doping in the respective AN systems [113]. The wide thermal hysteresis loop indicates the presence of the internal and external stress arises due to the dipole orientation, clamping of dipole moment at grain boundary regions etc. [71, 77, 87].

There are several factors which are responsible for loss in dielectric materials can be classified into two classes: (a) intrinsic loss and (b) extrinsic loss. The intrinsic loss arises from the anharmonic phonon decay process in pure crystal lattice whereas the extrinsic loss finds its source from crystal defects, grain boundaries, pores and secondary phases. In the Chapter 4 of this thesis, the dielectric loss was related to the increase in grain size of the modified $AgNbO_3$ systems which is a published work in the journal. It was argued that the intrinsic grain conduction dominates over extrinsic one within the prescribed frequency and temperature range and therefore, hence the major source of dielectric loss must be of intrinsic in nature. In the present work also, the intrinsic grain conduction is observed to be dominating over the extrinsic interfacial conduction, which will be discussed in the next section. But, the most expected cause for the minimal variation of dielectric loss in the modified systems can be related to their non-noticeable variation in the shape and size of the grains. The little variation in tangent loss may be explained in terms of increasing non-uniformity in the distribution of the grains.

5.7 Complex Impedance Spectroscopy Study

The relaxation behaviour of the AN based systems was examined by the complex impedance spectroscopy study. Imaginary part of the impedance (Z") and imaginary part of the electrical modulus (M") vs. frequency study which can help to know about the low frequency relaxations present in a system. The inability of resolving the multiple relaxations in the low frequency region, present in a material, by the Z" study can be overcome by the M" study, which scale inversely to capacitance [109-112].

Fig. 5.9.(a, b) and Fig. 5.10(a, b) illustrate the selective plots of the impedance (Z"(f)) and electrical modulus (M"(f)) variations for the AMN2 and AMN4 systems respectively. It is observed that in all the systems, low frequency relaxation peak appears ~ 350 ^oC in the M"(f) plot and it shifts towards higher frequency region at further elevated temperatures. The low frequency relaxation peak also appears in the Z"(f) plot ~ 355 ^oC and shifts towards higher frequency region at further elevated temperatures. The existing dipoles in a material contribute their maximum electrical response at the frequency corresponding to the relaxation peak and beyond this they remain in relaxed state. The insets of all the figures show the log f_{max} vs. 1/T plots separately for the Z"(f) and M"(f) behaviours, which suggest that the relaxation process is of Arrhenius type. The Arrhenius type behaviour is given by $f = f_0 \exp(E_a^{rel}/ k_BT)$, where, f_0 is the pre-exponential factor and E_a^{rel}

represents the activation energy of the dielectric relaxations, present in the system. For all the systems, the activation energies are calculated and plotted in the inset of their respective figures. These high values of E_a^{rel} suggest the possibility of grain conduction in the AMN systems [116-118].

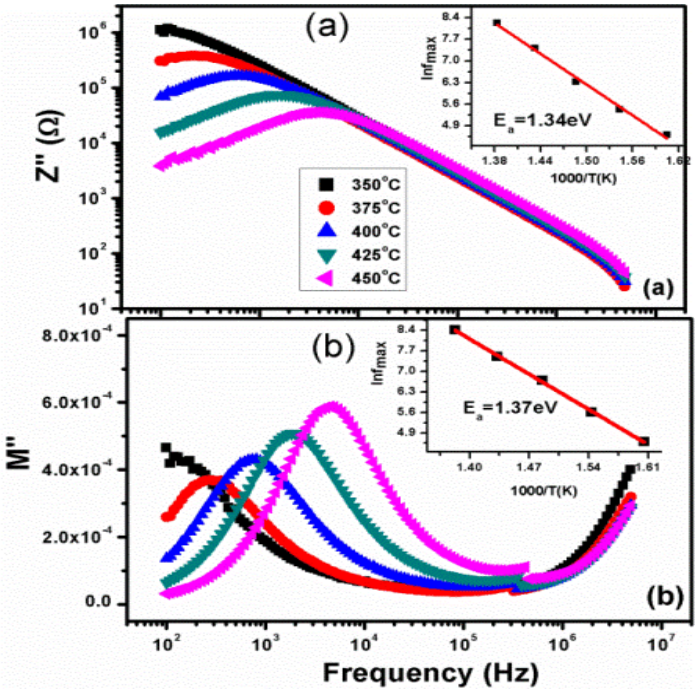

Figure 5.9: Imaginary part of electrical impedance (Z"(f)) plotted in log-log scale and modulus (M"(f)) plotted in linear scale of the AMN2 system at selected temperatures. The inset shows the activation energy derived from relaxation frequencies.

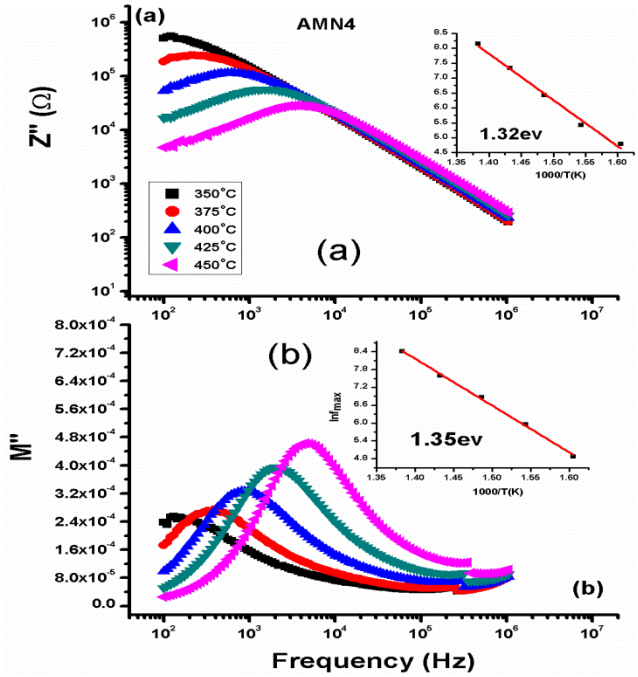

Figure 5.10: (a) Imaginary part of electrical impedance (Z"(f)) plotted in log-log scale and (b) modulus (M"(f)) plotted in linear scale of the AMN4 system at selected temperatures. The inset shows the activation energy derived from relaxation frequencies.

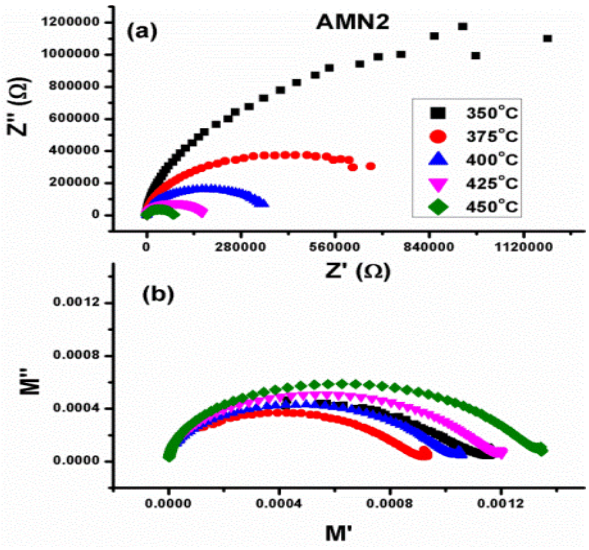

Figure5.11: (a) Cole-Cole (Z' vs. Z'') and (b)Cole-Cole (M' vs. M'') plots of the AMN2 system.

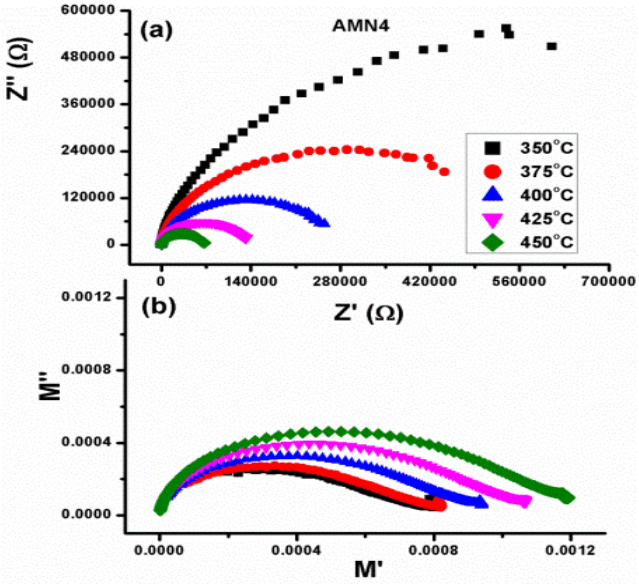

Figure 5.12: (a) Cole-Cole (Z' vs. Z'') and (b) Cole-Cole (M' vs. M'') plots of the AMN4 system.

We have also studied the Cole-Cole of impedance in which Z' is plotted against Z'' in the diagrams. The appearance of semicircle in the diagram indicates to a relaxation process. The number of semicircles appear in the diagram are related to different conducting sources. For three distinct semicircles appear in the diagram, the high frequency semicircle is identified due to the intrinsic grain conduction effect, the intermediate frequency semicircle is due to the interfacial grain boundary conduction effect and the low frequency semicircle is due to the electrode contact effect. Fig. 5.11a and Fig. 5.12a illustrate the Cole-Cole of impedance diagrams of the AMN2 and AMN4 systems. Only one semicircle appears for all the systems within the prescribed frequency and temperature range whose centres seem to be lie below the abscissa axis. Such depressed semicircles indicate non-Debye type of conduction process within the samples. The radius of the Cole-Cole semicircle equates approximately to the resistance of the material at the corresponding temperature. It is observed that the radii of the semicircles for all the systems of investigation decreases with increase in temperature.

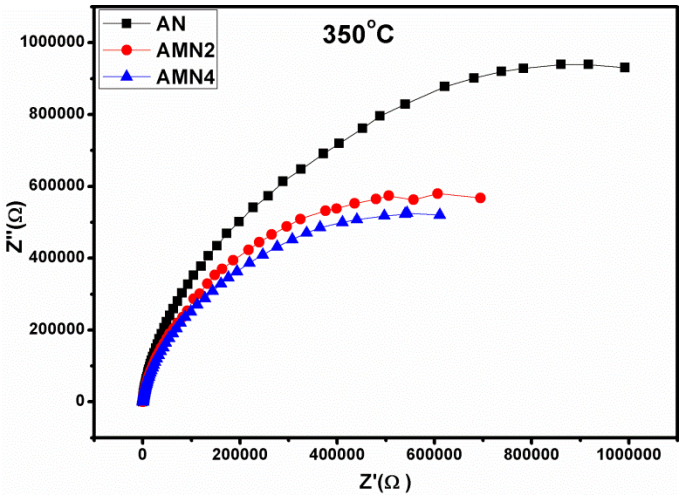

Figure 5.13: Comparison of resistance from Cole-Cole radius, at 350°C.

Again, in order to assess the effect of doping on resistances of the systems as well as its rate of degradation with temperature the combine plot of Cole-Cole semicircles of the AN, AMN2 and AMN4 systems at some selected temperatures are illustrated in Fig. 5.13.It is observed that the resistance of the modified systems reduces as an effect of doping but order of the resistance remains same at all the temperature. With elevated temperature, the rate of degradation of resistance also remains approximately uniform.

In the Chapter3, the increased/decreased activation energies of the modified systems are related to the increase/decrease in the resistance of the compounds. But the activation energies of the AMN2 and AMN4 are very close to that of AN system. It is also reported in earlier works that the activation energy depends upon the oxygen vacancies. But from the XPS data, the oxygen vacancy related peak is not that much prominent to surely ascertain their role in determining the behaviour of activation energies in this modified systems.

To sort out the multiple relaxations in a systems, the Cole-Cole of electric modulus is an important tool which plots M' against M" in the diagram. Sometime the superimposed effect of different conductions is not properly resolved in the Cole-Cole of impedance which appears distinct in the former method and provides more information regarding intrinsic and extrinsic conduction sources. Fig. 5.11b and Fig. 5.12b illustrate the Cole-Cole of modulus of the investigated systems in which only single semicircles appear in the diagrams. This confirms that a single relaxation process dominates over the total conduction mechanism, which can be related with the grain effect. Therefore, the macroscopic relaxation process present in the AMN systems may be due to the microscopic conduction, which occurs inside the grains.

5.8. Conclusion

$AgNbO_3$ systems modified with MnO_2 were prepared by conventional solid state route. Improved ferroelectric and dielectric properties in the modified systems were explained on the basis of hole doping, increase in difference of the electronegativity of cations and anions and Jahn-Teller distortion. However, double value of remnant polarisation of the AMN4 system than other systems indicates that Jahn-Teller distortion dominates over the other factors. Intrinsic (grain) conduction was identified in all the systems.

Chapter 6

Dielectric, ferroelectric and impedance spectroscopic studies of WO_3–doped $AgNbO_3$ ceramic

6.1. Introduction

$AgNbO_3$ is considered as a multifunctional material with microwave communication, micro technologies and as a visible light driven photocatalyst. The multi-phase transition in temperature dependent permittivity plot has made this material interesting for fundamental research. The compound assumes distorted perovskite ABO_3 structure at room temperature. The recent group of researchers assigned the non-centrosymmetric *Pmc2₁* space group to explain its weak ferroelectricity which brings to an end of the earlier assigned centrosymmetric *Pbcm* space group which was meant for antiferroelectric behaviour. But, the discovery of a strong field induced double hysteresis loop having saturation polarisation of 52 μC/cm^2 in its polycrystalline form and revelation of high permittivity (ε_r> 400) in microwave/radio frequency range for $AgNb_{1-x}Ta_xO_3$ (x=0.5) solid solution, has also diversified its application in semiconductor industries [49,85, 86]. There exists a complicated coupling between NbO_6 octahedral tilting and local displacements of both Ag and Nb which mechanised a series of changes in the cation displacements. Though, both the Ag and Nb cation possess the off-centering behaviour the material experiences weak ferroelectricity. The low tolerance factor (t = 0.956) is responsible for excess NbO_6 octahedral rotation during phase transition which obstructs Ag displacement as well as force its dynamic in antiferroelectric order. Suitable modification is proposed to induce chemical pressure to suppress the octahedral rotation by increasing the tolerance factor given by t = $\frac{r_{A-O}}{r_{B-O}\sqrt{2}}$ which may recover Ag off centering behaviour to enhance ferroelectricity [55]. Several modifications have been carried out by substituting monovalent cations (Li, Na, K) in place of Ag at A-site of the compound which reports interesting results which differs for one from another cations effect on dielectric and ferroelectric properties [70-88]. The B-site (Nb^{5+}) has been modified largely by Tantalum (Ta^{5+}) by several researchers which reports excellent microwave properties [62-66, 82-86]. The most exciting result came in the compound with separate Li and Ta substitution having number of published works and along with this a combine substitution effect of Li and Ta also has been reported recently. Apart from this, few works has been reported with Bi, Sb substitution to enhance the electric properties. However, the charge carrier (hole/electron) doping also controls the octahedral rotation that blocks the off-centering of Ag ion which has been theoretically investigated by *K.Uchida et.al*. and verified with the experimental findings [35]. According to them, the tolerance factor of a compound increases/decreases as per the nature of the charge carriers due to increase/decrease of the effective radius of the cation/anion in a compound.

In this chapter we want to investigate the effect of electron doping on the dielectric and ferroelectric properties of $AgNbO_3$ system. In the present work 0.02 and 0.04 moles of WO_3 were substituted in place of Nb_2O_5 to prepare $AgNbO_3$ modified with WO_3 systems. This was preferred so as to partially incorporate W^{6+} (r = 0.60Å) in place of Nb^{5+} (r = 0.69Å) in order to create electron in the AN system. The effect of electron doping (W^{6+}, W^{5+}), the presence of Jahn-Teller active cation W^{5+} ($5d^1$), and electronegativity of Mn (2.36) on the dielectric and ferroelectric properties of the modified systems were observed, analysed and discussed in detail. Along with this, the contribution of microstructures like intrinsic (grain) or extrinsic (grain boundary, sample-electrode surface contact etc.) parameters to conduction mechanism also investigated by complex impedance spectroscopy technique.

6.2. Experimental details

The $AgNbO_3$ and its modified systems were prepared by solid state route by taking Ag_2O, Nb_2O_5 and WO_3 as the starting materials. The amount of WO_3 was calculated in molecular weight fraction (x=0.02, 0.04) of Nb_2O_5 to design some modification. The modified systems are named as AWN2 and AWN4 systems. In each case 3wt% extra Ag_2O was added to meet the silver loss due to its volatility. After proper manual grinding to intersperse the oxides, the mixtures were set for calcination at temperature of 830°C for 6hrs. The calcined powders were mixed with 3 wt% polyvinyl alcohol (PVA) solution with proper milling and uniaxially pressed into disks of diameter ~10 mm and a thickness ~1 mm using hydraulic press under ~70 MPa pressure. The prepared samples for various measurements were sintered at 1030°C for 3hrs. XRD patterns of the samples were taken by using RIGAKU ULTIMA IV using nickel filter with Cu K_α radiation issuing from a 1.6 kW Rigaku rotating anode generator. Measurements were taken on reflection mode of oriented crystal pellets for step size 0.025^o at scanning rate 10^o per minute. The microstructures of sintered pellets were observed using a JEOL JSM-6084LV scanning electron microscope (SEM) as well as the mapping images of the samples was taken. The pellets were allowed for Au coating on the targeted surface by a sputtering unit up to two minutes. This was intended to avoid the accumulation of electrons on the surface of the samples due to electron irradiation during image. X-ray photo electron spectroscopy was taken to examine the oxidation states of the incorporated dopants *i.e.* tungsten and other constituent elements. The data were obtained by using Thermo ESCALAB 250 physical electronics photoelectron spectrometer having Al Kα X-ray (1486.6 eV) as exciting radiation. The binding energy was determined by reference to the C 1s line at 284.8 eV. The impedance data were taken by using HIOKI IMPEDANCE ANALYZER IM3570 within frequency domain of 100 Hz to 1 MHz in a temperature range 25^oC - 450^oC. Hysteresis loops were taken by Radiant precision ferroelectric characterisation system, a standard ferroelectric testing machine (Radiant Technology). Raman spectrum was measured using a laser Raman spectrometer (Horribba Scientific Instruments T6400) at room temperature. The power of the incident laser beam was 200 mW with monochromatic wavelength 514 nm.

6.3. Results and Discussion

6.3.1. XRD, SEM, XPS and RAMAN results

Fig. 6.1 illustrates the XRD patterns of the all prepared samples. Positions of all the diffraction peaks are well indexed to orthorhombic $AgNbO_3$ (JCPDS Card No. 070-

4738/052-0405). Presence of minute traces of secondary phases is observed in the pattern but which is reported to be unavoidable in the prepared compound irrespective of synthesis routes [41, 58]. The lattice parameters were calculated by check cell software by considering orthorhombic unit cell containing single formula unit which are provided in the table 6.1. The shifting in position of diffraction peaks may be related to the partial incorporation of tungsten in place of niobium.

Fig. 6.2 illustrates the SEM images of the AN and AWN systems from which we can observe the changes in its surface microstructures. The grains of the parent AN system appears to be polyhedron shaped having their size distributes from 1.5μm – 3μm and is very much similar to the earlier reports. But in the modified systems, the shape of the grains transforms gradually from apparently polyhedron in AWN2 to more alike cube/cuboid in AWN4 with overall increase in its dimension to ~ 5μm.

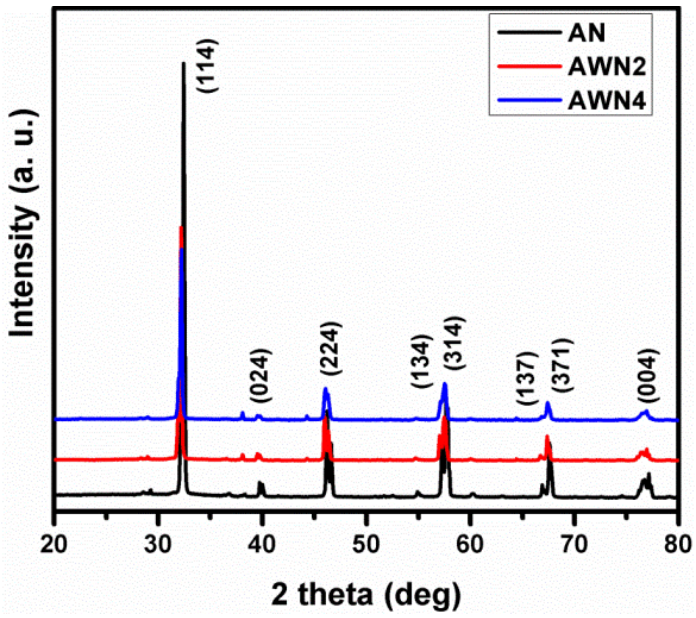

Figure 6.1: X-Ray diffraction pattern of the AN and its modified systems.

Table 6.1: Lattice parameters calculated by using check cell software.

Compound→ / Lattice Constant↓	AN	AWN2	AWN4
a (Å)	3.9541	3.9476	3.9570
b (Å)	3.9002	3.8140	3.8998
c (Å)	3.9331	3.9222	3.9314

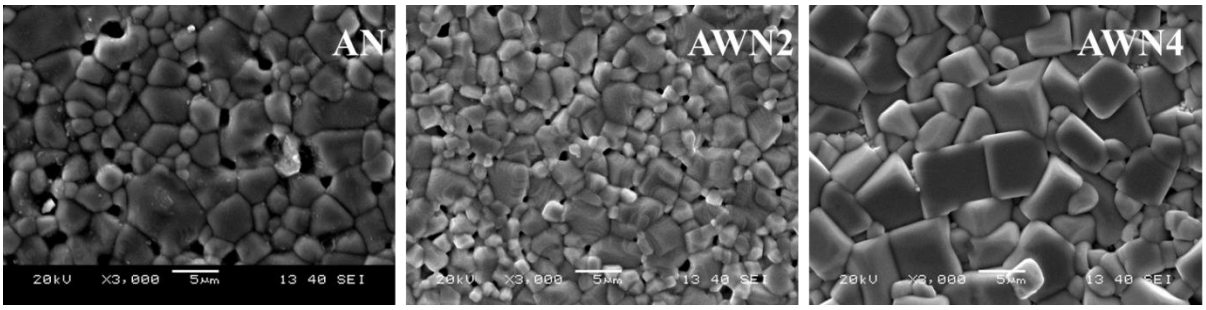

Figure 6.2: SEM images of the AN, AWN2 and AWN4 systems.

The presence of pores reduces comparatively to that of parent system. Experimental density ~91%, 91.7% and 92.5% of theoretical density are obtained of sintered AN, AWN2 and AWN4 ceramic samples, respectively. The transformation in shape and size of the grains in the modified systems also suggests the partial occupation of the tungsten in place of niobium. Fig. 6.3 illustrates the XPS data of the AWN systems which is helpful in identifying the oxidation states of the constituting elements present in the compound. The positions of the peaks for all the constituent elements are given separately in the figure sheet. The corresponding binding energies of all the peaks indicate the presence of silver in Ag^{1+} state, niobium in Nb^{5+} state and the minor element tungsten in W^{6+} and W^{5+} states [54, 133]. This confirms successful electron doping due to presence of W^{6+} ($5d^0$) and incorporation of Jahn-Teller active cation W^{5+} ($5d^1$) in the AN system [32, 33].

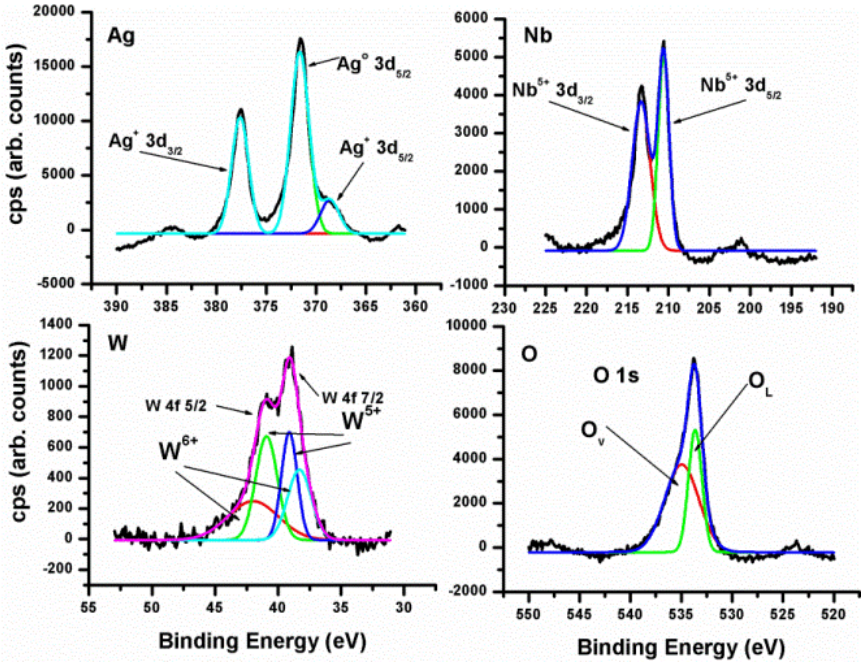

Figure 6.3: X-ray photoelectron spectroscopy images of the AWN system showing the possible oxidation states of the constituent elements.

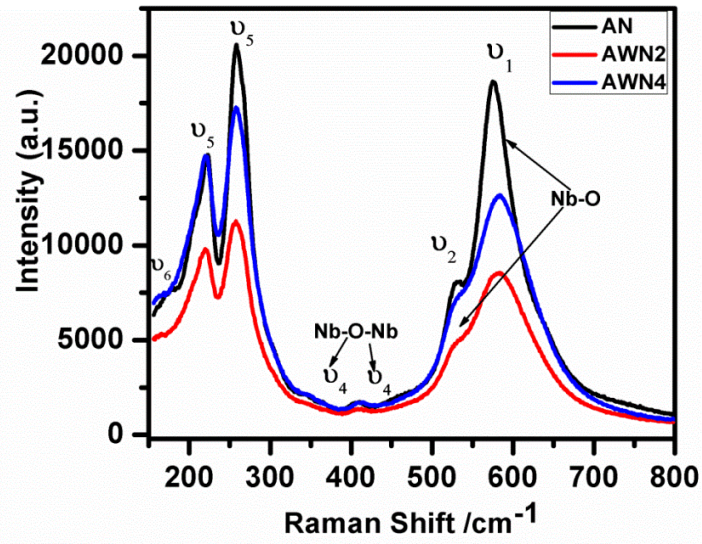

Figure 6.4: Raman spectra of the AN and AWN systems showing the possible vibrational modes of the systems.

Raman spectra provide important information regarding the internal vibration in the crystal lattice. Fig. 6.4 shows the different vibrational modes obtained in our prepared sample of the parent AN and its modified system which agrees well with the previous reported data. It is observed that all the internal vibrations related to NbO_6 octahedra lies within 160 cm^{-1} to 900 cm^{-1}. Around the region 170 cm^{-1} to 325 cm^{-1}, the first intense mode is observed which is splitted and corresponds to the degenerated modes assigned as υ_6 and υ_5 respectively. The modes ~ 360 cm^{-1} and ~ 420 cm^{-1} are of low intensity which are assigned as υ_4 and is supposed to be the associate bending modes of Nb-O-Nb bonds. The possible cause for this low intensity is due to the low tilting angle between the adjacent NbO_6 octahedra. The second intense mode appears ~ 575 cm^{-1} – 610 cm^{-1} with a shoulder ~ 525 cm^{-1} – 575 $cm^{-1}$are assigned as υ_1 and υ_2 respectively. These modes are supposed to be arised due to the symmetric stretching of The NbO_6 octahedra which corresponds to different Nb-O bond lengths. The vibrational modes appeared in the spectrum of the modified systems are also found to be identical to that of the parent system. But the intensity of the peaks reduces considerably in the modified systems which depend upon the content of tungsten in the compounds. The minimal shifting of vibrational modes and reduction in its intensity confirms that W^{6+} has successfully occupied the sites of Nb^{5+} in the $AgNbO_3$ ceramic [114, 115].

6.3.2. Dielectric and ferroelectric results

Fig. 6.5 illustrates the temperature dependent relative permittivity (ε) for AWN2 and its modified systems during heating as well as cooling cycles at four selected frequencies. Four major dielectric anomalies at $T_C^{FE} \approx 72°C$ ($M_1 \leftrightarrow M_2$), 263^oC ($M_2 \leftrightarrow M_3$), $T_C^{AFE} \approx 327^oC$ ($M_3 \leftrightarrow O_1$) and 370^oC ($O_1 \leftrightarrow O_2$) are observed in our prepared sample. Similarly, the appearance of dielectric anomalies in the AWN4 systems are observed at $T_C^{FE} \approx 33°C$ ($M_1 \leftrightarrow M_2$), 248^oC ($M_2 \leftrightarrow M_3$), $T_C^{AFE} \approx 310^oC$ ($M_3 \leftrightarrow O_1$) and 356^oC ($O_1 \leftrightarrow O_2$), which is shown in Fig. 6.6. A hump like feature appears within $M_2 \leftrightarrow M_3$ during cooling cycle which matches mostly to the earlier reports. The thermal hysteresis also clearly observed at the T_C^{AFE} which is a basic feature of ferroelectric systems.

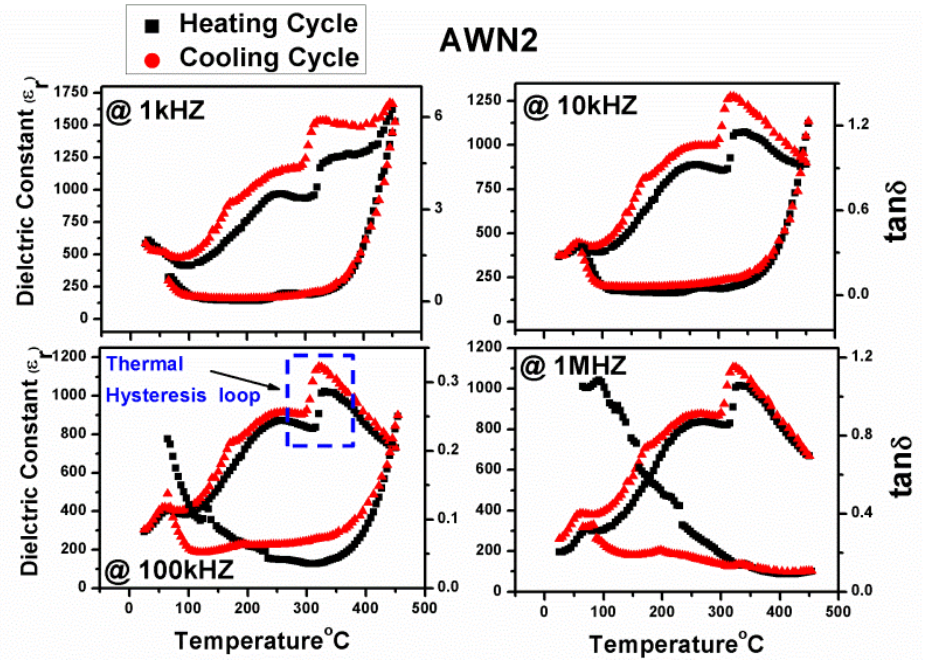

Figure 6.5: Temperature dependent relative permittivity and tangent loss of the AWN2 systems at selected frequencies. The heating and cooling cycles with the thermal hysteresis are also shown at different layers.

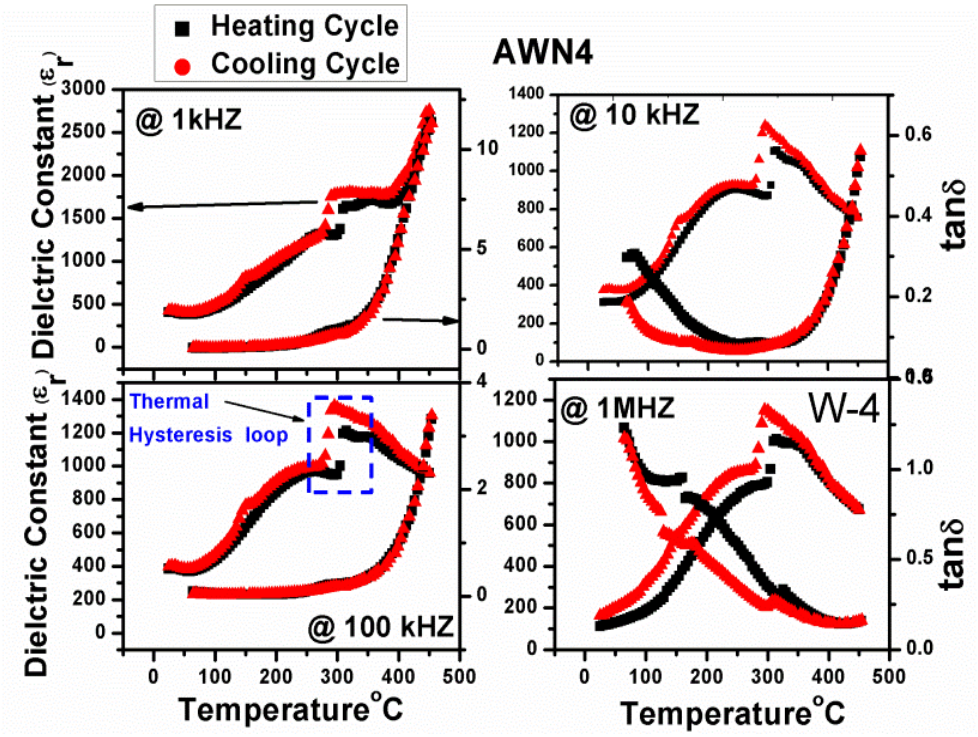

Figure 6.6: Temperature dependent relative permittivity and tangent loss of the AWN4 systems at selected frequencies. The heating and cooling cycles with the thermal hysteresis are also shown at different layers.

It is observed that all the transition points shifts towards lower temperature in WO_3 modified AN systems which is contrast to the result of MnO_2 modified AN systems. The

thermal hysteresis at the T_C^{AFE} is also shown in the figure and it is observed that the region of thermal hysteresis widens with the dopant concentration. The modification also increases the dielectric loss which increases with the concentration of the dopant.

Fig. 6.7 illustrates the P-E hysteresis loop of the investigated systems which shows interesting results in the modified systems. From table 6.2, It is observed that the ferroelectric parameters of AWN2 systems reduce to lower value in comparison to the parent AN system. However, in the AWN4 system, the value of the above parameters improve and is found even more to that of the AN system.

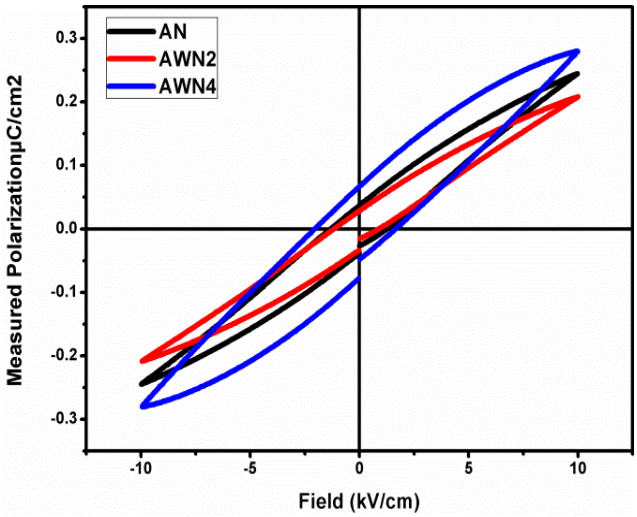

Figure 6.7: P-E hysteresis loop of the AN, AWN2 and AWN4 systems for 10kV of applied field.

Table 6.2: Ferroelectric parameters of the AN and AWN systems.

Applied Filed	Saturation & Remnant Polarization ($\mu C/cm^2$)	AN	AWN2	AWN4
10Kv	P_{max}	0.245	0.207	0.280
	P_r	0.035	0.028	0.066

6.3.3. Discussion

The microscopic parameters such as atomic or ionic radii, lattice parameters of the compound, ionicity and covalency of the bonds, local potentials, polarisabilities of the ions and bonds, nature and concentrations of the introduced defects influence the electric behaviour of the compound. Though, theoretical work carried out by K. Uchida *et al.* relate with the $SrTiO_3$ system but the effect of carrier doping on BO_6 octahedral rotation may be considered as universal. Generally, carrier doping in an oxide system creates variation in ionic radii as well as in tolerance factor, which can control the octahedral rotation. Theoretically it is calculated that the doped electrons occupy the bottom of the conduction band that is mostly contributed by the B site cation orbitals of the ABO_3 perovskite system [35]. In the $AgNbO_3$ system, the bottom of the conduction band consists of 4d orbitals of the Nb atoms [56, 132]. With the electron doping in the AWN

system, the effective radius of Nb increases and therefore, the tolerance factor decreases which ultimately promotes the octahedral rotation. Theoretically it is predicted that the promotion in octahedral rotation will suppress the ferroelectric instability. Experimentally it is also verified that electron doping will deteriorate the ferroelectric property in a compound. *Wang et.al.* verified their theoretical simulated work with the experimental results and reported that the doping electrons cascade the long range coulomb interaction which impedes the ferroelectricity due to over domination of short range repulsive forces [36]. Again, according to Pauling scale of electronegativity, when W (2.36) is partially substituted in place of Nb (1.6) the overall difference of electronegativity from O (3.44) decreases. The decrease in difference of electronegativity between the cation and anion reduces the ionic character of the bonds. The overall reduced ionic character of Nb-O bond reduces its polar nature and hence may reduce the ferroelectric properties.

From the XPS result, it is confirmed that tungsten exists in W^{5+} ($5d^1$) and W^{6+} ($5d^0$) states. Between these two oxidation states, W^{5+} ($5d^1$) are Jahn-Teller active ion and can expect of favouring a distortion within its octahedra which will reduce the octahedral tilting/rotation [1-3, 32]. If we observe at the evolution of P-E loop of the modified systems then one can notice that the ferroelectric parameters for the AWN2 systems are reduced. However, for AWN4 system the ferroelectric parameters are improved in comparison to the AN system which we can expect due to reduction in octahedral tilting/rotation. The inter competition of different mechanism for octahedral distortion can be expected from the above results. The doping of electron and the presence of W^{6+} ($5d^0$) promote octahedral rotation and hence will suppress the ferroelectric instability in $AgNbO_3$ system. The reduction in the difference of electronegativity between cation and anion due to incorporation of tungsten also reduces the polar nature of the bond. These three factors favour for the reduced ferroelectricity as we have found in AWN2 system. It is established that the Jahn-Teller distortion dominates over the all possible distortions. Therefore, the probable increase in concentration of Jahn-Teller active W^{5+} ($5d^1$) in AWN4 system led the dominance of Jahn-Teller distortion over the other possible mechanisms. This suppresses the octahedral tilting/rotation to some extent and recovers ferroelectricity in AWN4 system.

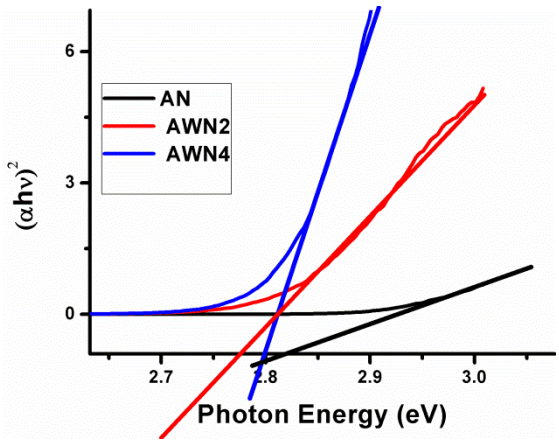

Figure 6.8: Band gap calculated from the UV spectra of AN and its modified systems.

It is earlier discussed in the introduction part that if the distortion in the perovskite structure reduces then it will widen the energy gap between the conduction band and the valence band. Fig. 6.8 illustrates the UV spectroscopy of the AN and AWN systems. It is observed that though the band gap of AWN2 and AWN4 system has decreased but the band gap of AWN4 system is more than that of AWN2 system. This indicates that in the

AWN4 system the structural distortion due to octahedral tilting/rotation is reduced and which is most probably due to the dominance of Jahn-Teller distortion over other possible factors.

It is established that in the high dielectric materials the BO_6 octahedra are joined to each other at their top which are the source of polarisation leading to high permittivity [126-127]. The cation located at the centre of the octahedra plays the crucial role in dominating their dielectric properties. In our perovskite oxide $AgNbO_3$, when the comparatively smaller cation W^{6+}(0.6Å) is substituted in place of Nb^{5+}(0.69Å) it intensifies the correlation among NbO_6 octahedra. This results the increase in permittivity of the AWN systems. The shifting of Curie temperature depends upon the bond strength. The reduced intensity of Raman vibrational modes indicates the decrease of bond strength. Therefore, in the AWN systems all the transition points shift towards lower temperature.

There are several factors which are responsible for loss in dielectric materials which can be classified into two classes: (a) intrinsic loss and (b) extrinsic loss. The intrinsic loss arises from the anharmonic phonon decay process in pure crystal lattice whereas the extrinsic loss finds its source from crystal defects, grain boundaries, secondary phases and pores. In the chapter-4 of this thesis, it is concluded that the increase in dielectric loss in the modified systems in which intrinsic grain conduction is a dominating figure, depends upon the increased grain size [136]. Therefore in AWN systems the enhance dielectric loss can be related to the increased grain size as it is confirmed from SEM images as in the subsequent section it will be verified that the intrinsic grain conduction is the major contributing part in the total conductivity of the AWN systems.

6.4. Complex impedance spectroscopy

Complex impedance spectroscopy is a technique to investigate the relaxation mechanism shown in a ceramic compound. This will provide the information regarding the conducting regions (intrinsic or extrinsic) and the limit of temperature when charge carriers activate and the nature of the activated charge carriers within a prescribed frequency and temperature range. For the application purpose of any material this information provides the suitable area and range for the better efficiency of the concerned material [109-112, 123-125]. This relaxation behaviour can be observed by studying the spectrum of imaginary part of impedance (Z") and imaginary part of electric modulus (M"). Fig. 6.9(a, b) and Fig 6.10(a, b) illustrate the relaxation peaks of imaginary part of impedance (Z") and imaginary part of electric modulus (M") at selective temperatures. The low frequency relaxation appears ~350^oC in the AN system whereas in the AWN2 system it appears ~250^oC and in the AWN4 system it appears ~225^oC. The relaxation peaks in all the systems behave in the same manner with temperature. As the temperature elevates, the relaxation peaks shift towards the higher frequency belt with reduced height. The frequency corresponding to the relaxation peak is the maximum frequency that can be followed by the charge carriers associated with dipoles. Beyond this frequency, the carriers are unable to follow the changing applied field and hence remain relax without in stress. With increase in temperature, the thermal energy enables the dipoles to follow the frequency of higher order and hence the reason for shifting of relaxation frequency. The insets of all the figures show the log f_{max} vs. 1/T plots separately for the Z"(f) and M"(f) behaviours, which suggest that the relaxation process is of Arrhenius type. The Arrhenius type behaviour is given by $f = f_0 \exp(E_a^{rel}/ k_BT)$, where, f_0 is the pre-exponential factor and

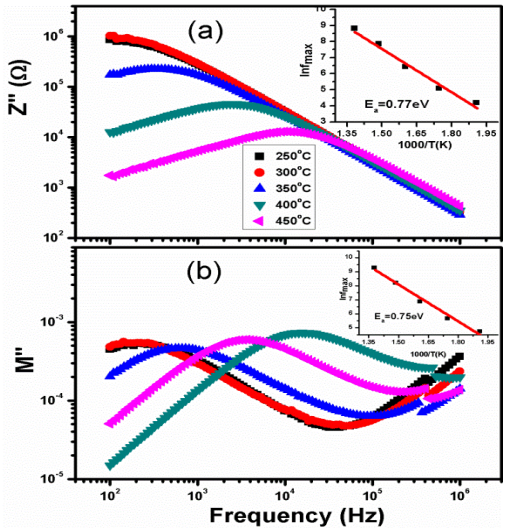

Figure 6.9: (a) Imaginary part of electrical impedance (Z"(f)) plotted in log-log scale and (b) modulus (M"(f)) plotted in linear scale of the AWN2 system at selected temperatures. The inset shows the activation energy derived from relaxation frequencies.

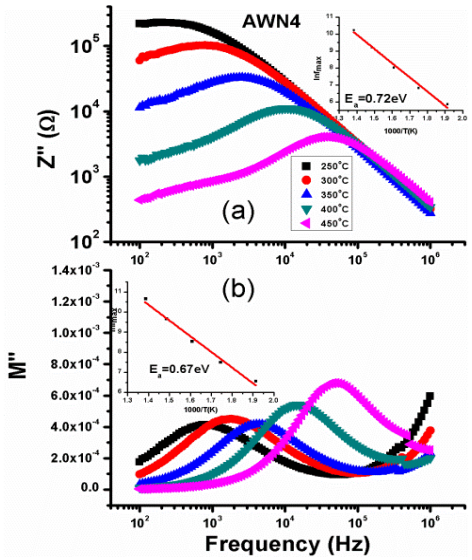

Figure 6.10: Imaginary part of electrical impedance (Z"(f)) plotted in log-log scale and modulus (M"(f)) plotted in linear scale of the AWN4 system at selected temperatures. The inset shows the activation energy derived from relaxation frequencies.

E_a^{rel} represents the activation energy of the dielectric relaxations, present in the system. The calculated activation energy for the AN system is bigger enough to assign the relaxation due to the intrinsic grain conduction effect. However, the calculated activation energies for AWN2 and for AWN4 are reduced to a lower value. In the Chapter3, it is observed that for the Sb_2O_5–doped and V_2O_5 –doped systems the activation energies also reduced sufficiently and is explained as the reason behind the lower temperature relaxations appeared in those systems. In the chapter-5, it is also observed that MnO_2 modifications do not bring in any lower temperature relaxation as the activation energies remain very close (AMN4) and even higher (AMN2) in comparison to the parent AN systems. Therefore, the lower temperature relaxations found in the AWN systems may be related to their reduced activation energies.

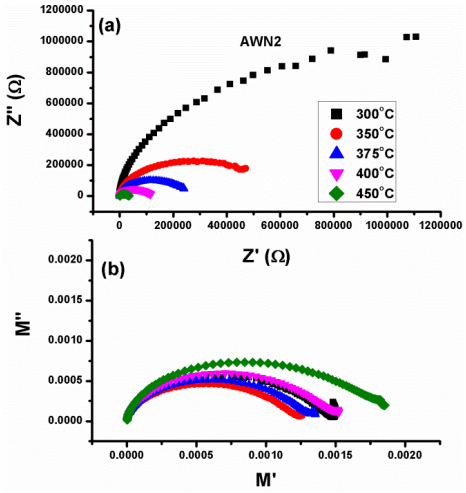

Figure6.11: (a) Cole-Cole (Z' vs. Z") and (b) Cole-Cole (M' vs. M") plots of the AWN2 system.

Cole –Cole diagram is plotted by taking real part of impedance Z' as an abscissa and imaginary part of impedance Z" as an ordinate. If the diagram appears like a semicircle then it indicates a relaxation mechanism. If more than one semicircle appears in the diagram then each semicircle attributes to a unique electrical response due to the activation of charge carriers in different regions like intrinsic (grain) or extrinsic (interfacial). If three Cole-Cole semicircles appear in the diagram within the frequency domain then the semicircle at high frequency attributes to the grain conduction, the semicircle at intermediate frequency ascribes to the grain boundary conduction and the semicircle at low frequency regime arises due to the surface conduction effect [109-112].

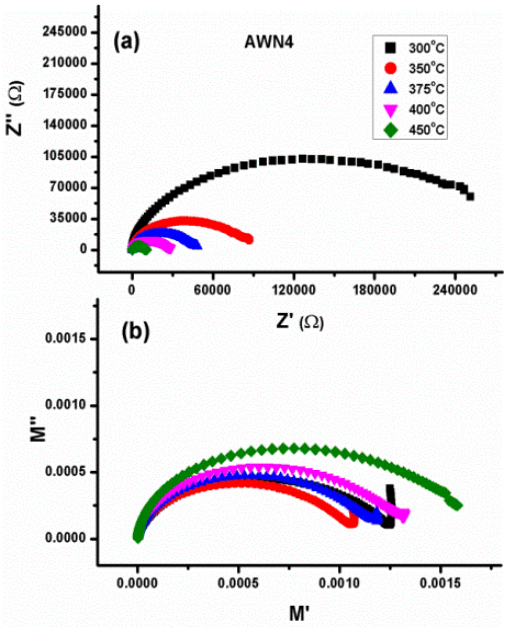

Figure6.12: (a) Cole-Cole (Z' vs. Z") and (b) Cole-Cole (M' vs. M") plots of the AWN4 system.

Fig. 6.11a and Fig. 6.12a illustrates the Cole-Cole of impedance of AWN2 and AWN4 systems in which only a single semicircle appears in the diagrams. All the semicircles are depressed *i.e.* their centres seem to be lie below the abscissa axis which indicates the nature of conduction within the compounds are of non-Debye type. For a Debye type of conduction a complete semicircle appears with its centre lie on the abscissa [109-112]. The radius of the semicircles measures the resistance of the material at that particular

temperature. It is observed that the radius of the semicircles decrease with the elevated temperature which indicates decrease in resistance of the material with increasing temperature. This shows the insulating/semiconducting nature of the material. However, the single relaxation in all the systems may be assigned to the intrinsic grain conduction effect as intrinsic charge carriers activate earlier in comparison to extrinsic regions in a high insulating material and so also may be in the $AgNbO_3$ ceramic. In order to bring a more clarification we plot the Cole-Cole of electric modulus (M' vs. M'') which has the ability to resolve two individual electric response. Electric modulus scales inversely to the capacitance whereas the electric impedance varies directly to the resistance of the region. As capacitance of intrinsic and extrinsic regions differs hugely therefore, the electric response of highest capacitive region likes surface-electrode contact completely suppresses in electric modulus but, highlights the lowest capacitive intrinsic grain region. Fig. 11b and Fig. 12b illustrates the Cole-Cole of modulus of the modified systems in which single semicircles also appear in the diagrams. This confirms that there is also dominance of intrinsic source of conductivity within the prescribed frequency and temperature range which can be attributed to the intrinsic grain conduction effect.

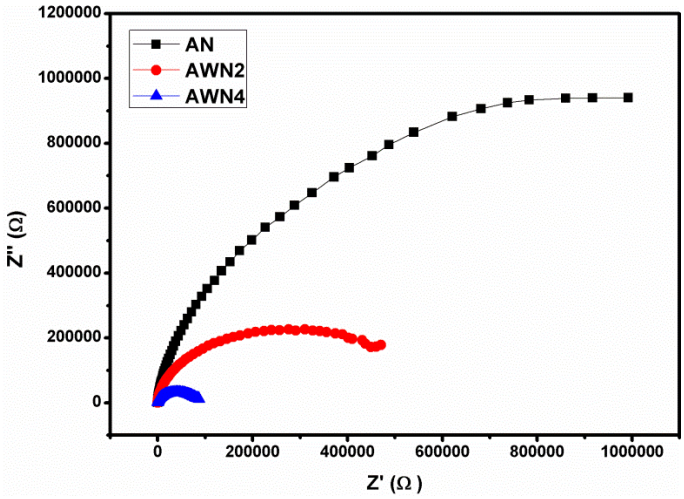

Figure 6.13: Comparison of resistance from Cole-Cole radius, at 350^{o}C.

Fig. 6.13 plots the Cole-Cole semicircles of the AN and AWN systems at 350^{o}C which shows the resistance of the material reduces sufficiently in the modified systems and the amount of reduction increases with the increase in the dopant concentration. As in the earlier discussion it is already verified therefore the reduced activation energies in the modified systems can be related to the reduced resistance of the systems.

6.5. Conclusion

$AgNbO_3$ systems modified with WO_3 were prepared by conventional solid state route. The ferroelectric and dielectric properties in the modified systems were explained on the basis of electron doping, increase in difference of the electronegativity of cations and anions and Jahn-Teller distortion. The contrast results in ferroelectric properties in AWN2 system and AWN4 system was explained on the basis of domination of Jahn-Teller distortion due to the increase in number of Jahn-Teller active ions in AWN4 systems. Intrinsic (grain) conduction was also identified as the dominant feature.

Chapter 7

Dielectric, ferroelectric and impedance spectroscopic studies of TiO_2-doped $AgNbO_3$ ceramic

7.1. Introduction

$AgNbO_3$ which assumes ABO_3 perovskite structure has been largely investigated as a parent material for microwave application and a visible light photocatalytic material. The multiphase transitions appeared in its temperature dependent permittivity ($\varepsilon\{T\}$) are associated with structural transformation, dynamics and ordering of cations i.e. Ag (A-site) and Nb (B- site). This has brought a curiosity among researchers to carry out fundamental research on it to observe the substitution effect at different cationic sites. Since its discovery by Fracombe and Lewis, a long standing debate continued to explain the slim hysteresis loop shown by the material whether belongs to antiferroelectricity or ferroelectricity. But *Fu et al*. reported the strong field induced double hysteresis loop having saturation polarisation of 52 μC/ cm^2 at a high applied field of 220kV/cm [49]. The early accepted centrosymmetric *Pbcm* structure which agrees well to antiferroelectricity has been overruled by the later research groups by suggesting to polar $Pmc2_1$at its virgin state to explain the weak ferroelectricity [57-61]. *Yashima et al*. have verified the displacement of atoms in ferrielectric order in $AgNbO_3$ lattice, which is an extremely rare in ferroelectric materials, that results net spontaneous polarisation [59]. Both, A- and B- site cation off centering are observed in the compound which also possesses strong covalency of A-O bonding [54, 55]. Instead of a very similar structural feature of lead based perovskite $AgNbO_3$ exhibits unacceptable low value of spontaneous polarisation in comparison to the lead based compounds. Structural accompanied with theoretical investigation revealed that though Nb at B-site atom goes ferroelectric ordering, the A-site Ag atom undergoes antiferroelectric ordering. *Grinberg et al.* investigated theoretically by taking a mixed structure of ferroelectric and antiferroelectric of 40 atom supercells and reported that the excess octahedral rotation of 14.5^oC due to low tolerance factor (0.956) blocks the off-centering of Ag ion [55]. The excess octahedral rotation to occupy the available space within cubic structure also forces Ag ion in antiferroelectric order. This problem can be overcome by substituting larger cation at A-site or smaller cation at B-site. In another way, by making alloy with compound of larger space volume negative pressure can be created which may open the blockage for Ag ion's proper displacement [55].

There are several modifications carried out at A-site by alkali elements (Li, Na, K) by *Kania et.al*., *Fu et.al*. and others [69-88]. The B-site is reported to be largely modified by Tantalum substitution at niobium place which has shown the best microwave properties. Some of the earlier works also reported the frequency dependent permittivity and susceptibility study in a wide range of frequency which mostly explained the dynamics of different cations which affects dielectric behaviour. In a breakthrough theoretical

investigation on effect of charge carrier doping in $SrTiO_3$, *Uchida et al.* have reported that the doping of hole can suppress the octahedral rotation which affects ferroelectric instability [35]. In the work, the authors have doped the charge carriers in the system by photo induction method in which effect of lattice distortion has not taken into consideration.

As most of the modifications in the $AgNbO_3$ system have been carried out by monovalent cations in place of Ag site and pentavalent cations specifically Ti^{5+} in place of Nb site, we have approached to modify the system by heterovalent cations in order to observe the charge carrier effect on various electric properties. Accounting the results of Uchida et al., we have chosen to dope hole in the titled compound by impurity doping method in order to observe its effect on ferroelectric instability. Again, till date the highly investigated, reported functional materials are $BaTiO_3$, $PbTiO_3$, lead zirconium titanate (PZT), lead lanthanum zirconium titanate (PLZT) and their modified systems in which the transition element titanium (Ti^{4+}) ion has occupied the B-site of the above perovskites. Therefore we select TiO_2 to dope with $AgNbO_3$ system in order to incorporate Ti^{4+} (0.61Å) in place of Nb^{5+} (0.69Å). In this paper we have reported the effect of hole doping on the dielectric, ferroelectric and electric transport properties of the systems modified with low molar percentage (x = 0.01, 0.02, 0.03 and 0.04) of TiO_2 to substitute Nb_2O_5. The improved dielectric, ferroelectric results were analysed and discussed by accounting effect of hole doping, effect of increase in difference of electronegativity and effect of Jahn-Teller distortion. This work is supposed to be useful for the fundamental research as well as for the application purpose as a functional material.

7.2. Experimental details

We prepared $AgNbO_3$/ (TiO_2) (x= 0.01, 0.02, 0.03, 0.04) by standard solid state reactions. Starting materials Ag_2O, Nb_2O_5 and TiO_2 were mixed stochiometrically for respective compound. The amount of TiO_2 was chosen to substitute Nb_2O_5 in molecular weight fraction to bring modification by incorporate titanium in place of niobium. Silver is a volatile element and hence silver based compounds suffers from loss of silver during high temperature calcination and sintering. To maintain the required stoichiometry of silver fraction, 3wt% extra Ag_2O was added to meet the silver loss due to its volatility [41, 58]. The mixtures were calcined at temperature of 830°C for 6hrs in air. The calcined powders were mixed with 3 wt% polyvinyl alcohol (PVA) solution with proper milling and uniaxially pressed into disks of diameter ~10 mm and a thickness ~1 mm using hydraulic press under ~70 MPa pressure. The prepared samples for various measurements were sintered at 1030°C for 3hrs. XRD patterns of the samples were taken by using RIGAKU ULTIMA IV using nickel filter with Cu K_α radiation issuing from a 1.6 kW Rigaku rotating anode generator. Measurements were taken on reflection mode of oriented crystal pellets for step size 0.025^o at scanning rate 10^o per minute. The microstructures of sintered pellets were observed using a Nova Nano SEM/FEI field emission scanning electron microscope (FESEM) as well as the mapping images of the samples was taken. The pellets were allowed for Au coating on the targeted surface by a sputtering unit up to two minutes. This was intended to avoid the accumulation of electrons on the surface of the samples due to electron irradiation during image. X-ray photo electron spectroscopy was taken to examine the oxidation states of the incorporated dopants *i.e.* titanium and other constituent elements. The data were obtained by using Thermo ESCALAB 250 physical electronics photoelectron spectrometer having Al K_α X-ray (1486.6 eV) as exciting radiation. The binding energy was determined by reference to the C 1s line at 284.8 eV. The impedance data were taken by using HIOKI IMPEDANCE ANALYZER

IM3570 within frequency domain of 100 Hz to 1 MHz in a temperature range 25^{o}C - 450^{o}C. Hysteresis loops were taken by Radiant precision ferroelectric characterisation system, a standard ferroelectric testing machine (Radiant Technology). Raman spectrum was measured using a laser Raman spectrometer (Horriba Scientific Instruments T6400) at room temperature. The power of the incident laser beam was 200 mW with monochromatic wavelength 514 nm.

7.3. Characterisations

7.3.1. XRD, FESEM, XPS and RAMAN study

The XRD patterns of all the synthesized samples are shown in Fig. 7.1. Positions of all the diffraction peaks are well indexed to orthorhombic $AgNbO_3$ (JCPDS Card No. 52-0405 and 070-

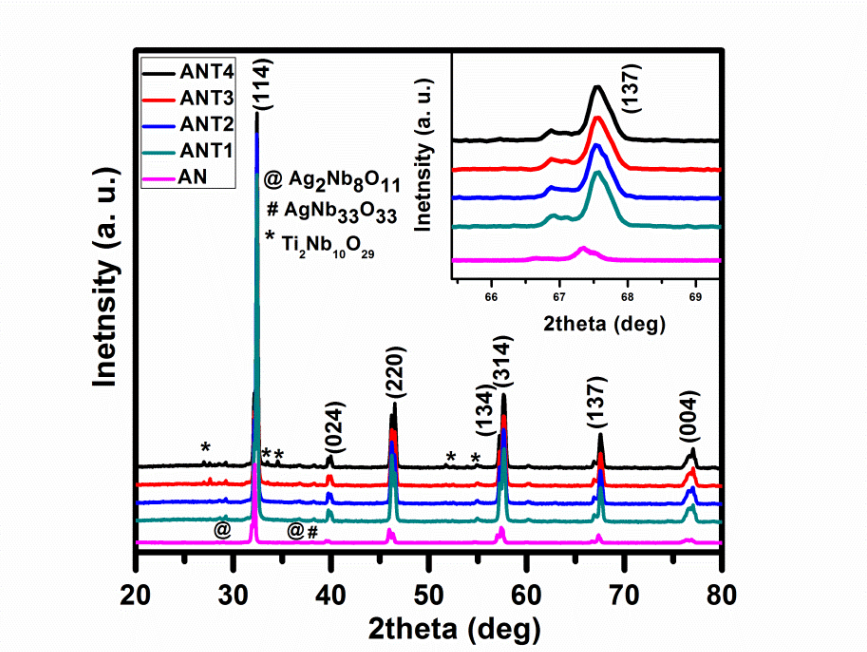

Figure 7.1:X-Ray diffraction pattern of the AN and its modified systems. The inset shows the enlarged view of (137) peak.

Compound→ / Lattice Constant↓	AN	ANT1	ANT2	ANT3	ANT4
a (Å)	3.9541	3.9556	3.9536	3.9528	3.9544
b (Å)	3.9002	3.9014	3.9020	3.9042	3.9015
c (Å)	3.9331	3.9353	3.9350	3.9333	3.9327

Table 7.1: Lattice parameters calculated from the Check cell software application.

4738). Minute traces of secondary phases are identified as $AgNb_{13}O_{33}$, $AgNb_7O_{18}$ which are unavoidable irrespective of synthesis conditions [41]. The impurity secondary phase in the modified systems is identified as $Ti_2Nb_{10}O_{29}$ having a negligible intensity in comparison to the parent phase. The prominence of these impurity phases increases with the increase in the concentration of TiO_2. The lattice parameters are calculated by Check-cell software application by considering the structural unit equivalent to the single formula unit $AgNbO_3$ which are listed in the table 7.1. Though, there are noticeable changes in the lattice parameters but the overall volume of unit cell remains approximately same. The shifting of diffraction peak suggests a successful substitution of titanium at the desired site.

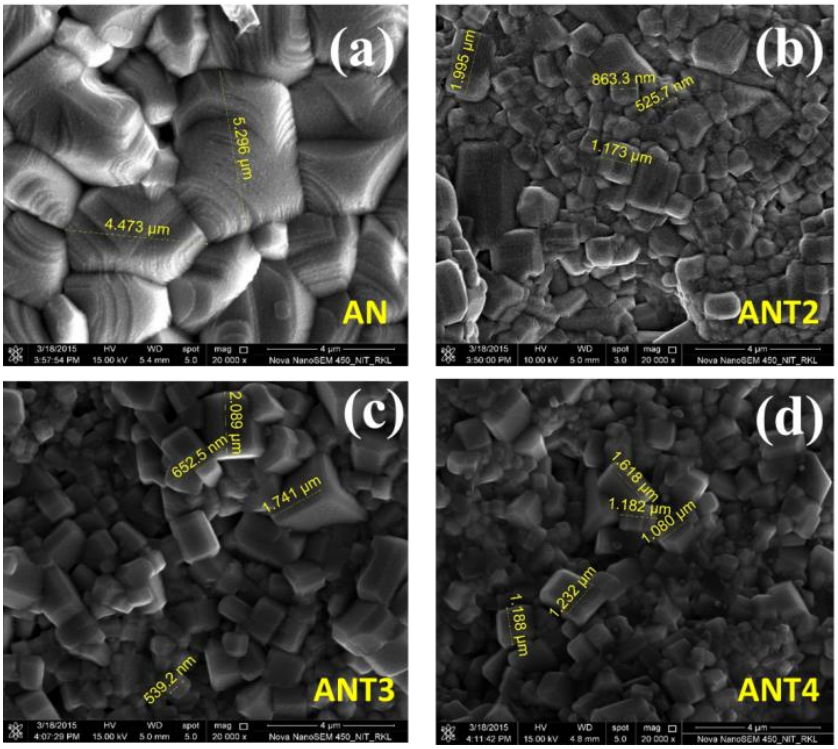

Figure 7.2: FESEM images of the AN, ANT2, ANT3 and ANT4 systems.

Fig. 7.2 illustrates the FESEM images of the AN and its modified systems. The grains of the AN sample are of polyhedron shape which distributes inhomogeneously having size ranges from 1.2µm to 5µm. The substitution of titanium has reduced the grain size. Inhomogeneous distribution of grains from nano scale (~ 500 nm) to micro scale (~2 µm) is observed in the modified system. The shape of the grains has also transformed into cube/cuboid shape in the modified systems. Fig. 7.3 illustrates the XPS spectra of the AN and its modified system. The binding energies corresponding to the position of the peaks agree with the existence of Ag^{+1} and Nb^{+5} states. It is also confirmed that titanium exists in the sample both in Ti^{+3} and Ti^{+4} oxidation states [54, 134]. This indicates the successful hole doping in the system. In addition, Ti^{3+} ($3d^1$) is a Jahn-Teller active ion and hence will promote Jahn-Teller distortion [32, 33].

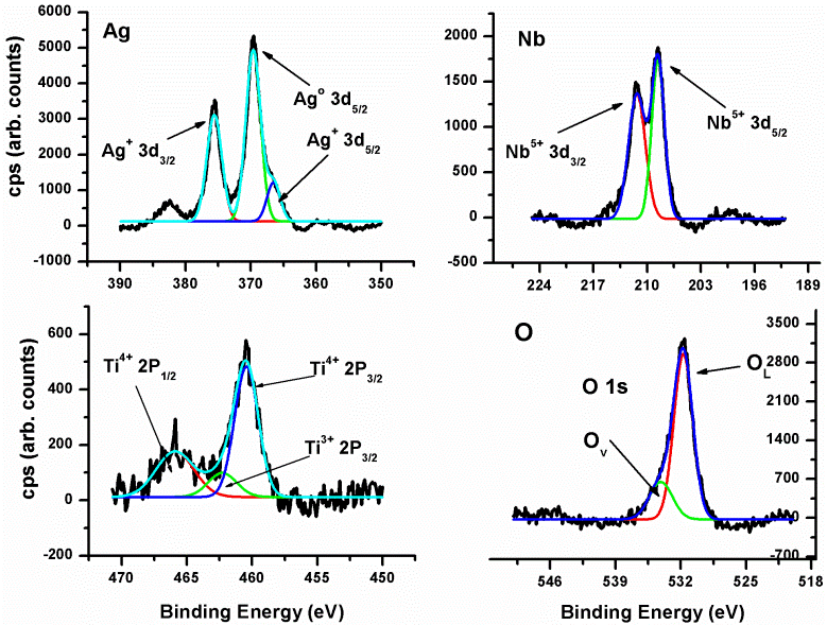

Figure 7.3: X-ray photoelectron spectroscopy images of the ANT system showingthe possible oxidation states of the constituent elements.

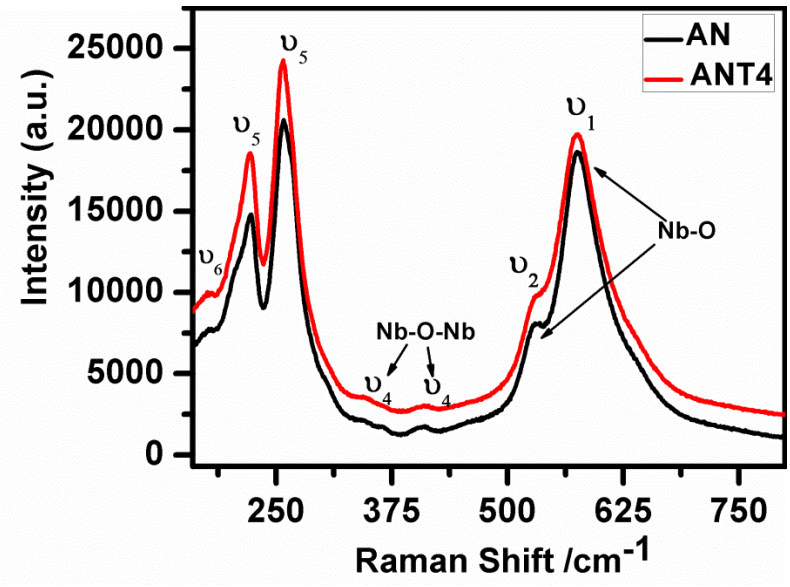

Figure 7.4: Raman spectra of the AN and ANT4 system showing the possible vibrational modes of the systems.

Fig.7.4 shows the Raman spectra of the AN and its modified system. The intense modes at 170 – 300 cm^{-1} and at 570 – 600 cm^{-1} indicates the vibration modes of NbO_6 octahedra which match to the earlier reported values [113, 114]. In the modified system, there appears a slight shifting of the vibrational modes towards lower wave number side. This indicates the increase in bond strength in between metal cation and oxygen anion. According to Pauling scale, the electronegativity of Ti is 1.54 and that of Nb is 1.6 and therefore, when Ti is substituted in place of Nb, the electronegativity difference between the Nb and O increases. The increasing difference in electronegativity between metal and oxygen signifies for more ionic character in the bonds. Therefore, the electrostatic attraction among the metal and oxygen atom increases accordingly and as a result it

enhances the bond strength comparatively. The shifting of Raman modes also indicates the successful incorporation of titanium in place of niobium.

7.3.2. Dielectric study

Fig.7.5, Fig 7.6 and Fig 7.7 illustrate the temperature dependent dielectric constant (ε) and loss (tanδ) at selected frequencies for the modified systems. The heating and cooling cycles of individual samples along with their thermal hysteresis are also shown in its different layers.

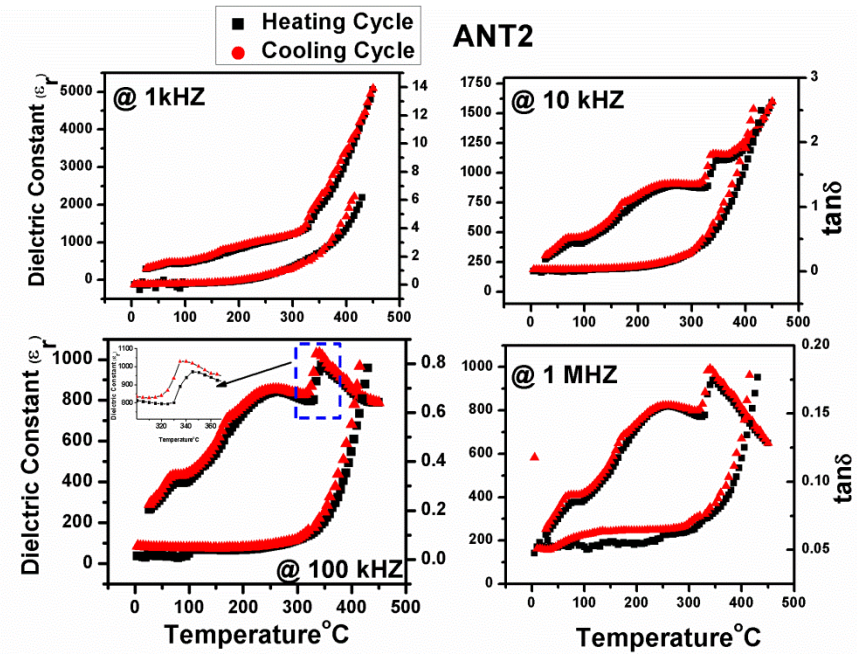

Figure 7.5: Temperature dependent relative permittivity and tangent loss of ATN2 systems at selected frequency. The heating and cooling cycles with the thermal hysteresis are also shown at different layers.

From the position of dielectric anomalies, nature and shape of the heating and cooling curve of the temperature dependent relative permittivity it is confirmed that the quality of the crystal is suitable for other characterisations though silver loss is imminent in the compounds. There is a significant improvement observed in the dielectric values of the modified systems. The low temperature dielectric anomaly (T_C^{FE}) shifts towards lower temperature and the high temperature dielectric anomaly (T_C^{AFE}) shifts slightly towards higher temperature. The modification has also brought an increase in the dielectric loss but the rate of increase is high above the Curie point (T_C^{AFE}) whereas it is very minimal below the mentioned point. In a modified system the various parameters of the dopants which play crucial role in the systems are identified such as: atomic or ionic radii, lattice parameters of the compound, ionicity and covalency of the bonds, local potentials, polarisabilities of the ions and bonds, nature and concentrations of the introduced defects like vacancies and interstitial ions [51].

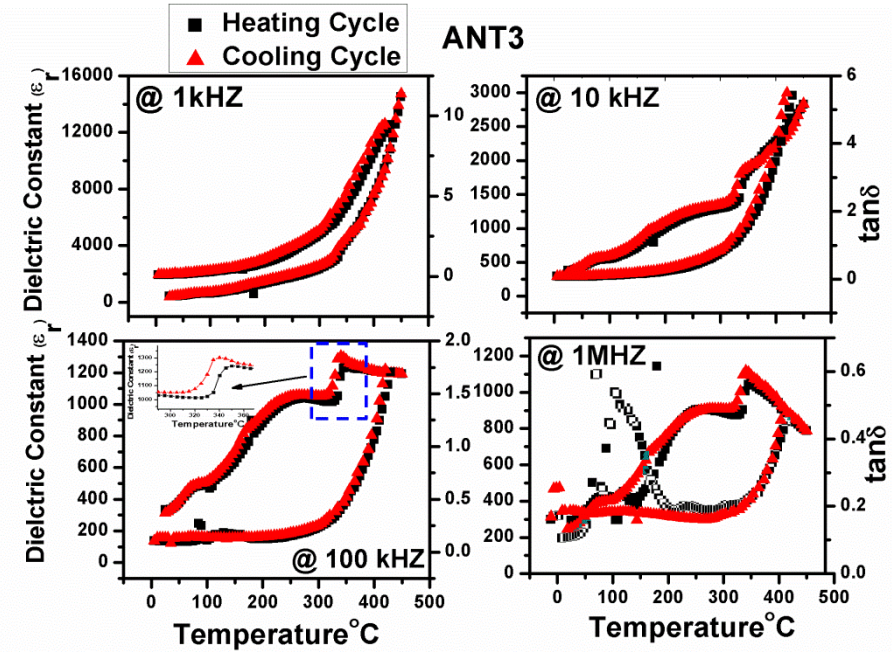

Figure 7.6: Temperature dependent relative permittivity and tangent loss of ANT3 system at selected frequency. The heating and cooling cycles with the thermal hysteresis are also shown at different layers.

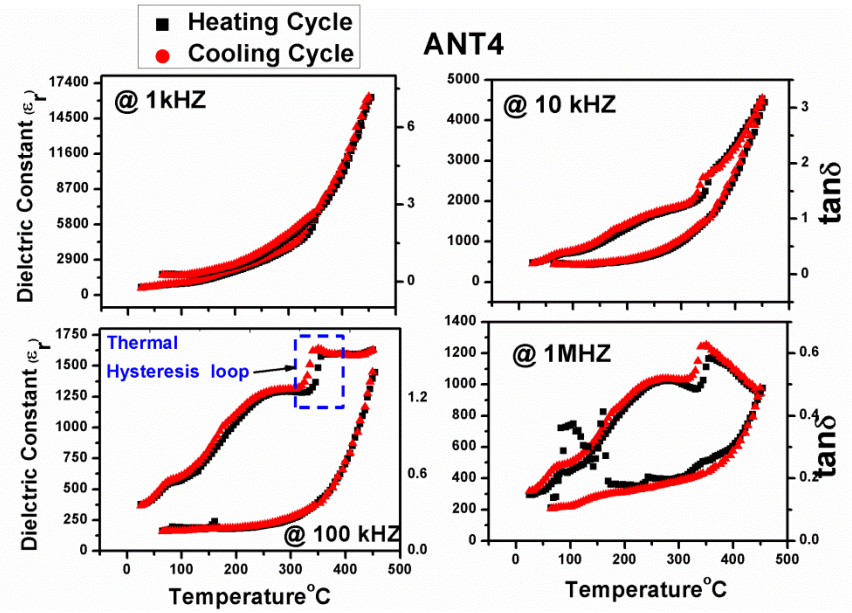

Figure 7.7: Temperature dependent relative permittivity and tangent loss of ANT4 systems at selected frequency. The heating and cooling cycles with the thermal hysteresis are also shown at different layers.

These parameters of the dopants often generate some additional dipole moments which affects polarisation mechanism and net polarisability of the systems. Apart from this, porosity, grain size and secondary phases can also affect the electric properties of a ceramic. In the AN modified systems, though small but a noticeable changes in the lattice parameters are observed, we can expect for the NbO_6 octahedra linked lattice distortion. Therefore, this definitely influences the cationic dynamics which is a very crucial mechanism in the AN system and is the source of the multiple phase transition which relates to ferroelectric and antiferroelectric behaviours. It is also established that the

dielectric materials with high permittivity are linked to the BO_6 octahedra joined to each other at their top. Therefore, the cation located at the centre of the octahedra plays the crucial role in dominating the dielectric properties of high permittivity ceramic materials. Again, it is also expected that the incorporation of smaller cations in place of larger cation in BO_6 octahedra increases the rattling space for cation movement. The partial substitution of Ti^{4+} (0.61 Å) in place of Nb^{5+} (0.69 Å) might have increased the rattling space which enhances cation dynamics as well as polarisability. In the manner how Curie points varies in our case, has also been reported in the Li, Na substituting Ag as well as Ta substituting Nb in the AN system. Such type of behaviour is explained due to the generation of the internal stress as an effect of substitution. But, it is already established that Curie temperature depends upon the concentration of dopants and the bond strength between the metal and the oxygen atom in a perovskite oxide. From the study of Raman spectra, it was explained that the partial incorporation of titanium in place of niobium has increased the overall bond strength. Therefore, there is no noticeable effect of doping on the Curie temperature in the modified systems. There are several factors which are responsible for loss in dielectric materials can be classified into two classes: (a) intrinsic loss and (b) extrinsic loss. The intrinsic loss arises from the anharmonic phonon decay process in pure crystal lattice whereas the extrinsic loss finds its source from crystal defects, grain boundaries, pores and secondary or impurity phases. In the subsequent section of impedance spectroscopy analysis, the presence of extrinsic conduction effect at higher temperatures will be verified in the modified systems. The extrinsic conduction sources comprises various interfaces like grain boundary and sample-electrode contact surfaces along with the presence of impurity phases, pores, defects, interstitial ions etc. As we have traced the presence of impurity secondary phases from the XRD pattern as well as the expectation of increase in grain boundary densities due to reduced grain size therefore, the comparatively high dielectric loss above Curie point in the modified systems can be related to the conduction of these extrinsic sources.

7.3.3. Ferroelectric study

Fig. 7.8shows the polarisation verses electric field (P-E) at RT of the AN and its modified systems, plotted at a common applied voltage for comparison. An unsaturated slim hysteresis loop of P_r = 0.037 μC/cm^2, P_{max} = 0.2444 μC/cm^2 is observed for AN system which matches to the earlier report. The substitution of titanium has changed the nature of the loop. The curve at highest voltage region gradually rounds up, approaches towards a lossy feature as titanium concentration increases. Both the remnant polarisation as well as the coercive field has increased significantly. Though, theoretical work carried out by *Uchida et al.* was taken in $SrTiO_3$ but the effect of carrier doping on BO_6 octahedral rotation may be considered as universal. Generally, carrier doping in a material creates variation in ionic radii as well as in tolerance factor and which can control the octahedral rotation [35]. Since, the doped holes in an oxide material occupies top of the valence band with oxygen 2p orbital, but in $AgNbO_3$ system, the top of valence band consists mostly of oxygen 2p and to some extent of Ag 4d orbitals [132].It is reported that the doping of hole increases the tolerance factor, which suppresses the octahedral rotation [35].Titanium mostly exists in Ti^{3+}, Ti^{4+} oxidation states in a compound and the most preferable one is the Ti^{4+} state which is already confirmed from our XPS result. Hence substitution of titanium in place of niobium will inject holes in the AN system. In $AgNbO_3$ system, the excess octahedral tilting locks the Ag off-centering and which results weak ferroelectricity [55]. Since, doping of holes suppresses the octahedral rotation, which can result unlocking of the off-centering behaviour of the Ag ions and lead to an increase of

the dipole moments in the modified AN system. We expect the enhanced remnant polarisation value is due to the effect of hole doping in the AN system.

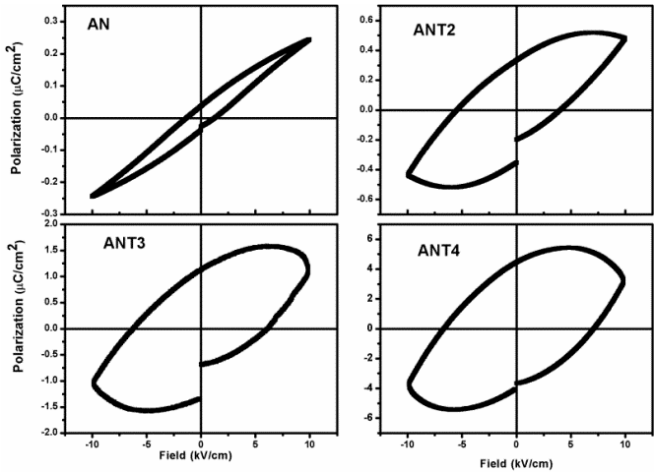

Figure 7.8: P-E hysteresis loop of the AN, ANT2, ANT3 and ANT4 systems for 10kV of applied field.

Table-7.2: Ferroelectric parameters of AN and ANT systems.

Applied Filed	Saturation & Remnant Polarization ($\mu C/cm^2$)	AN	ANT2	ANT3	ANT4
10Kv	P_{max}	0.245	0.48	1.44	4.90
	P_r	0.035	0.33	1.14	4.38

Again, as it was explained earlier that the incorporation of Ti in place of Nb has increased the difference of electronegativity between the metal and oxygen and hence the ionic character of the bonds increases. It is already established that ionicity of the bonds provides polar character to it whereas covalency of the bonds provides non-polar character to it. The increasing ionic character makes the bonds polar in nature. In other words, the incorporation of Ti increases the polarisation in the modified systems, which completely agrees with our experimental results. From the XPS result, it is confirmed that titanium exists in Ti^{3+} ($3d^1$) and Ti^{4+} ($3d^0$) states. Between these two oxidation states, Ti^{3+} ($3d^1$) are a Jahn-Teller active ion and can expect of favouring a distortion within its octahedra which will reduce the octahedral tilting/rotation. From the evolution of P-E loop, one can notice that there is significant enhancement in ferroelectric parameters in the modified systems. The P_r value in ANT4 system is increased ~ 100 times of the parent AN system. Increase in difference of electronegativity between cation and anion due to titanium incorporation increase the polar nature of the bonds. Though, doping of hole favours for suppression of octahedral tilting/rotation but Jahn-Teller distortion can be considered as a dominative feature in ANT4 system. The counts of Jahn-Teller active ions increase with the increase concentration of titanium.

It is earlier discussed in the introduction part that if the distortion in the perovskite structure reduces then it will widen the energy gap between the conduction band and

valence band [1-3, 30]. Fig. 7.9 illustrates the UV spectroscopy of the AN and ANTsystems. It is observed that the band gap of ANT4 system has increased by some value than the AN system. This indicates that in the ANT4 system the structural distortion due to octahedral tilting/rotation is reduced and which is most probably due to the dominance of Jahn-Teller distortion over other possible factors.

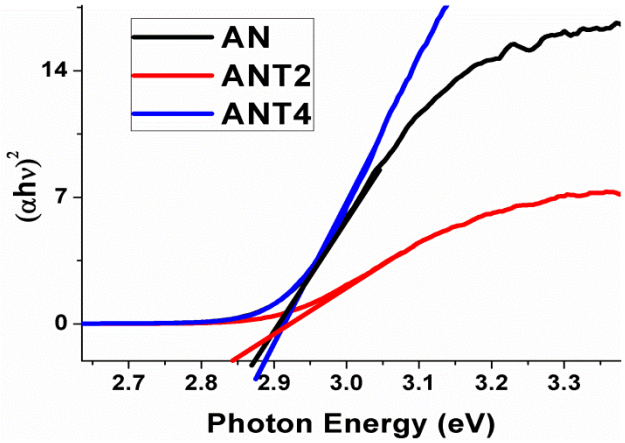

Figure 7.9: Band gap calculated from the UV-spectra of the AN and its modified systems.

Jaykumar et al. have reported that the leaky feature in their modified bismuth ferrite system is due to the anion vacancies or the valence fluctuation of the transition metal ions leading to electronic conduction [122]. *Das et al.* has mentioned the presence of leakage current which overshadow the domain reorientation in their report on modified bismuth ferrite nano tube system [135]. The above explanation may hold to our results. But in our modified AN system, the lossy feature of the P-E loop can be related to the charge carrier (hole) doping which may have increased the leakage current. The coercivity is mostly related with the friction which arises due to the domain orientation. We assume that the reduced grain size below to the micro level has enhanced the friction during domain orientation.

7.3.4. Complex impedance study

A polycrystalline sample consists of grain (intrinsic) region and interfaces like grain boundary and electrode-sample contact (extrinsic) regions. Apart from this, the surface structure contains grains and lattice defects like grain boundaries, pores, cracks, vacancies etc. The charge carriers at different regions require different energies to activate and participate in conduction process. Complex impedance spectroscopy study is a technique to analyse the electric transport properties of the material and to distinguish the activated regions and the nature of charge carriers [109-112, 123-125]. Lots of information can be extracted from the relaxation peaks appearing in the imaginary part of impedance (Z") and electrical modulus (M"). In some cases, the intrinsic and extrinsic contribution overlaps and cannot be properly resolved in the Z" (f) as it scales directly to the resistance of the grain and interface regions. The inability of resolving the multiple relaxations properly within low frequency regime in Z" can be solved in better way in M" as the latter one scales inversely to capacitances. Fig.7.10 shows selective plots of the (a) impedance (Z"(f)) and (b) electrical modulus (M"(f)) respectively, which exhibits relaxation process. The diagram of Z"(f) is plotted in log-log scale in order to highlight the peak region as well as keep all the files in a single figure but M"(f) is plotted in linear scale. A weak relaxation peak enters through the low frequency window of M"(f) around 345 ^{o}C in the parent AN system which becomes prominent and shifts towards higher frequency side

with elevated temperature. The low frequency relaxation also appears in Z"(f) but in a later stage around 375 ^{o}C and in similar manner shifts towards higher frequency with rising temperature. The broadness of the relaxation peak indicates the distribution of relaxation time which depends upon the uniformity of the grain size [90-92].

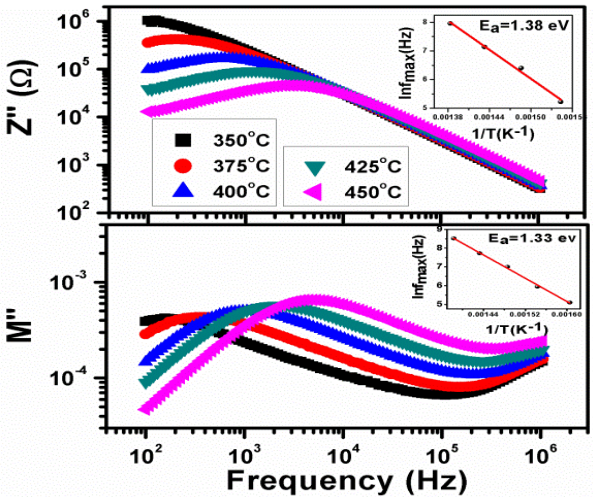

Figure 7.10: Imaginary part of electrical impedance (Z"(f)) plotted in log-log scale and modulus (M"(f)) plotted in linear scale of the AN system at selected temperatures. The inset shows the activation energy derived from relaxation frequencies.

The existing dipoles contribute their maximum electrical response at the frequency corresponding to the relaxation peak and beyond which they remain in the relaxed state. The plots the log f_{max} vs. 1/T separately for Z"(f) and M"(f) are shown in the inset of figures indicates the relaxation process which is characterised by Arrhenius type behaviour ($f = f_0 \exp (E_a^{rel}/ k_BT)$), where f_0 is the pre-exponential factor and E_a^{rel} represents the activation energy of dielectric relaxations. We found the value of E_a^{rel} to be of 1.33eV and 1.38eV from electric modulus and impedance data respectively which is a bigger enough to be assigned with possible grain conduction only [116].

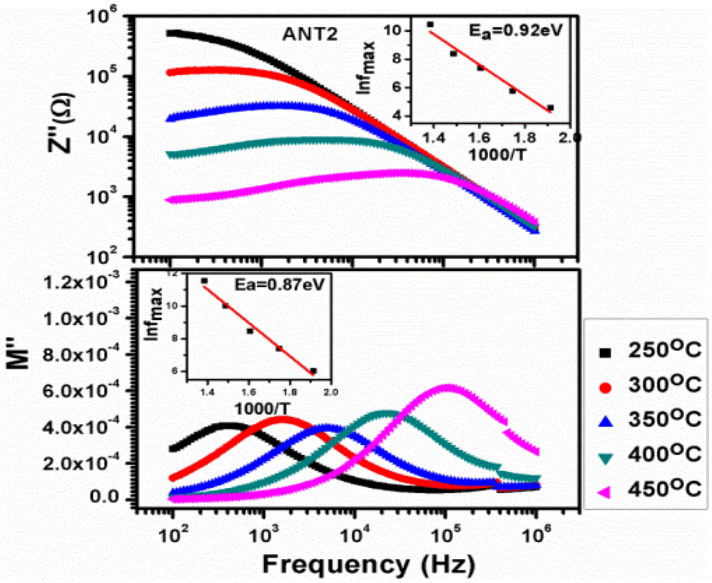

Figure 7.11: Imaginary part of electrical impedance (Z"(f)) plotted in log-log scale and modulus (M"(f)) plotted in linear scale of the ANT2 system at selected temperatures. The inset shows the activation energy derived from relaxation frequencies.

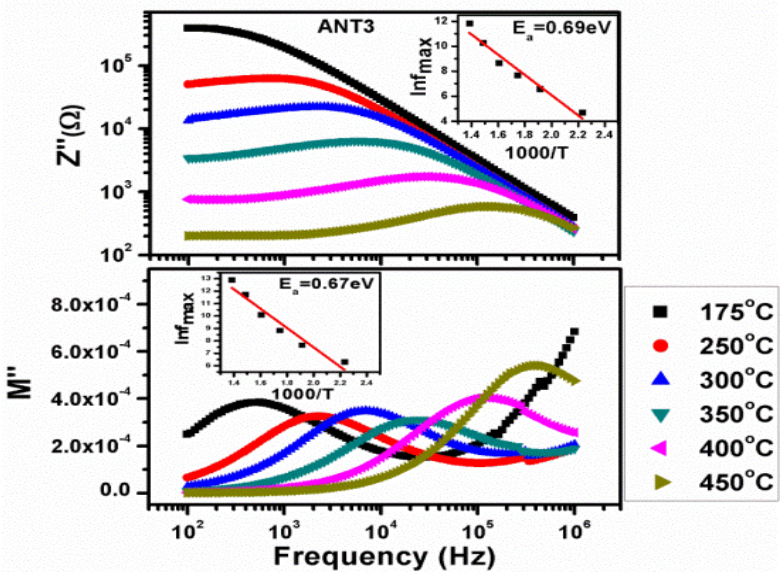

Figure 7.12: Imaginary part of electrical impedance (Z"(f)) plotted in log-log scale and modulus (M"(f)) plotted in linear scale of the ANT3 system at selected temperatures. The inset shows the activation energy derived from relaxation frequencies.

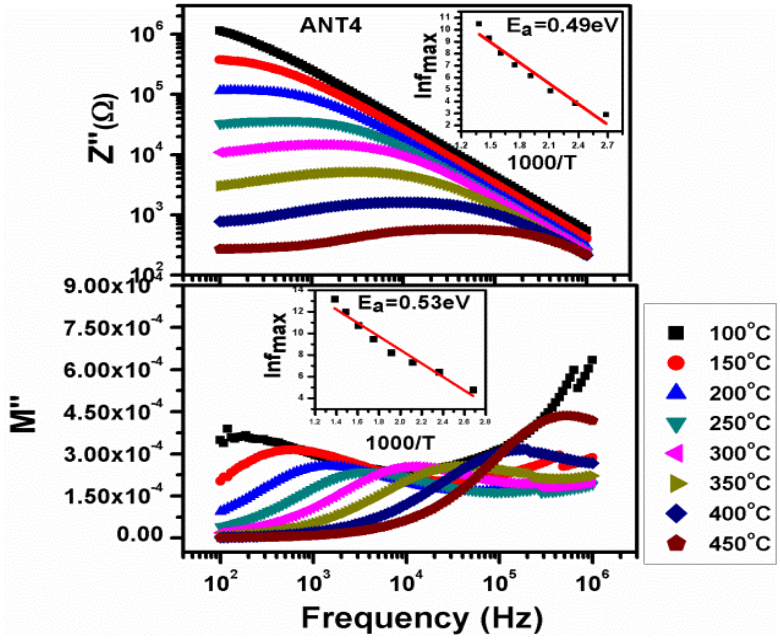

Figure 7.13: Imaginary part of electrical impedance (Z"(f)) plotted in log-log scale and modulus (M"(f)) plotted in linear scale of the ANT4 system at selected temperatures. The inset shows the activation energy derived from relaxation frequencies.

Fig. 7. 11, Fig.7.12 and Fig. 7.13 illustrate the combine plot of Z"(f) in log-log scale and M"(f) in linear scale, which illustrate the relaxation behaviours of the ANT2, ANT3 and ANT4 systems respectively. The low frequency relaxations appear comparatively at low temperatures such as ~ 250 ^{o}C in the ANT2 system, ~ 175 ^{o}C in the ANT3 system and ~ 150 ^{o}C in the ANT4 system which arises in the frequency domain much earlier compared to parent system (~ 345 ^{o}C). Like the parent system the relaxation peaks shift towards higher temperature as temperature elevates. But, the substitution of Titanium has highly broadened the peak regions. This is due to the drastic reduction in grain size with greater non-uniformity in its distribution and change in its shape. Following the previous

approach we have calculated the activation energies from the Arrhenius region of relaxation frequencies. It is observed that the value of the activation energy decreases with the content of titanium substitution. We expect that the appearance of low frequency relaxations at comparatively lower temperatures in the modified systems is due to the decrease in their activation energies. The decrease/increase in the activation energy has been related to the suppression/enhance in the oxygen vacancy after modification in the system [121, 136]. But in the chapter-4, we have explained the reduced activation energy in the modified system in terms of drastic reduction in the resistance of the compounds [136].The presence of multiple relaxation processes such as grain, grain boundary or surface conduction etc. can be verified by investigating the Cole-Cole of impedance (Z'' vs. Z') and electric modulus (M'' vs. M') in the AN and its modified systems. In the chapter -3, we have described the relaxation of the AN system.

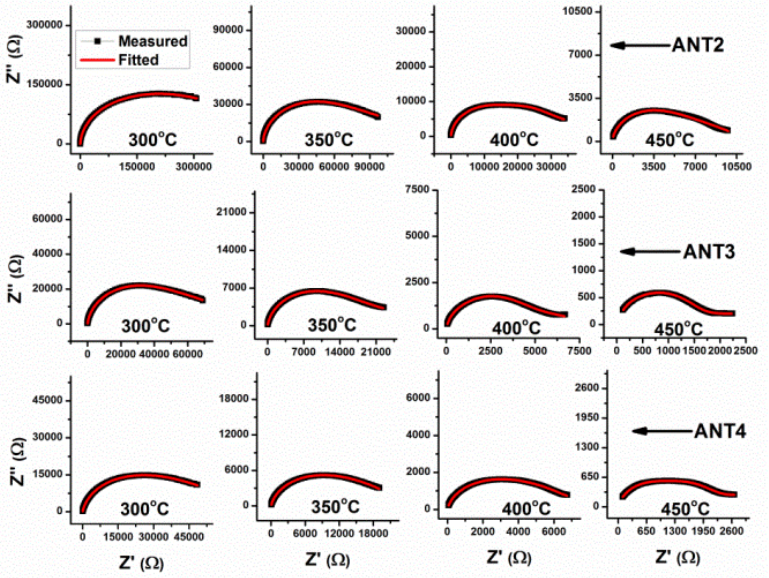

Figure 7.14: Cole-Cole (Z' vs. Z'') plot of the ANT2, ANT3 and ANT4 systems simulated with equivalent circuit model of R_s ($R_iC_iQ_i$) (R_eQ_e).

Fig. 7.14 illustrates the Cole-Cole of impedance of the modified systems for selected higher temperatures. Unlike the symmetric semicircles of the parent system, it is observed that the shape of the semicircle of the modified systems appears unsymmetrical in these temperature belts. A tail region appears at low frequency regime around the end temperatures (~ 400^{o}C and above) which increases with the increasing content of titanium. Again, the equivalent circuit model of R_s ($R_iC_iQ_i$) properly simulates the apparent symmetric semicircles (not shown in figures) up to ~275^{o}C in ANT2, ~250^{o}C in ANT3 and ~200^{o}C in ANT4 systems. Beyond the mentioned temperatures, the Cole-Cole semicircles are well simulated with the model of R_s ($R_iC_iQ_i$) (R_eQ_e), as shown in figure 7.13. This indicates that in these temperature belts some extrinsic sources also contribute to the total conduction. The drastic reduction in the grain sizes up to nano scale with highly non-uniformity distribution of grains as it is observed from the FESEM images and the presence of impurity secondary phases in the modified systems as confirmed from the XRD patterns may be some possible causes of being possible extrinsic conduction sources. We have cross checked the presence of external effect by studying the Cole-Cole of modulus which is illustrated in the Fig. 7.15 as it has the ability to suppress the

extrinsic surface conduction effect [34-36]. The single semicircle appears in the spectrum corresponds to the intrinsic grain conduction effect. It is also observed that the low frequency tail region of Cole-Cole of impedance disappears in the Cole-Cole of modulus which indicates that the source of the conduction process which responsible for this region must be of extrinsic in nature and hence holds our assumption of presence of extrinsic conduction effect in the modified systems at higher temperatures.

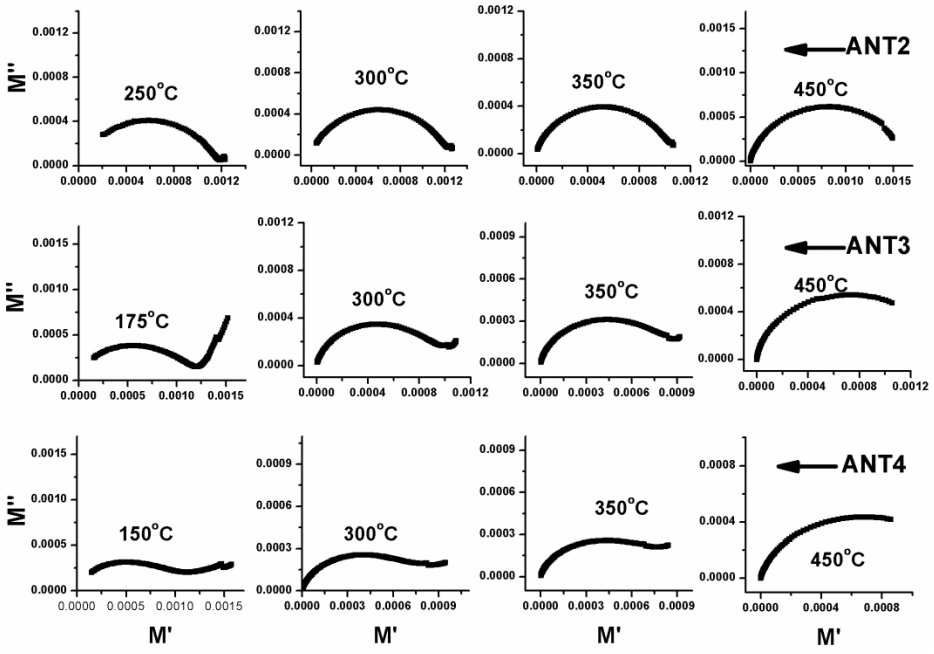

Figure 7.15: Cole-Cole (M' vs. M'') plot of the ANT2, ANT3 and ANT4 systems.

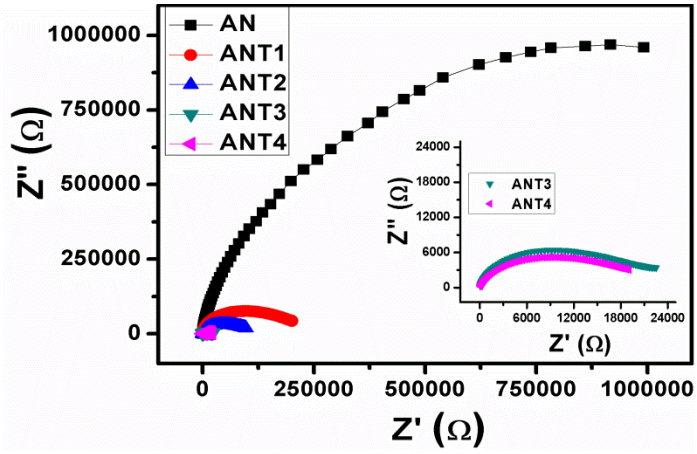

Figure 7.16: Comparison of Cole-Cole semicircles of the AN and its modifies systems at 350°C to verify the variation of resistance due to modification.

Fig. 7.16 illustrates the comparative plot of Cole-Cole semicircles of AN and its modified systems. The significant decrease in radius of the semicircles with increase in titanium concentration indicates drastic reduction in resistance after modifications. It is confirmed from the FESEM image that the grain size has reduced significantly which must have increased the density of grain boundary in the system. It is already established that grain boundary is more resistive than interior grain and hence resistance of the modified system

should have increased. The contrast result can be explained by assuming the conducting grain boundaries. The doping of hole might have reduced the grain boundary resistance as it is already verified the presence of extrinsic conduction in the modified systems. The order of the resistance 10^6 in the AN system has reduced to the order of 10^4 (ANT1, ANT2) and 10^3 (ANT3, ANT4) with titanium content. This may be the possible cause for the decrease in the activation energy.

Table 7.3: Resistance values of parent and modified systems at different temperatures

Systems→ / **Temp (^{o}C)↓**	**AN Resistance (Ω)**	**ANT2 Resistance (Ω)**	**ANT3 Resistance (Ω)**	**ANT4 Resistance (Ω)**
25	2.999E7	2.89E7	9.22E6	4.248E6
50	4.899E7	3.789E7	9.86E6	4.748E6
75	1.501E8	3.922E7	1.083E7	4.915E6
100	2.191E8	3.323E7	6.94E6	3.214E6
125	9.945E7	2.463E7	3.558E6	1.8E6
150	6.976E7	1.266E7	1.907E6	992200
175	4.984E7	7.143E6	1.058E6	575900
200	2.852E7	4.749E6	640600	353000
225	1.976E7	3.625E6	377200	216200
250	9.809E6	2.873E6	222800	134300
275	8.965E6	1.524E6	134300	90130
300	7.817E6	771200	87590	60900
325	5.436E6	385200	54940	38640
350	2.794E6	152800	27060	22730
375	1.091E6	89950	14040	12740
400	443200	48720	7766	7576
425	247800	24120	4574	4364
450	125500	11550	2955	2631

It is also established that the source of AC and DC conductions are different [137]. The activation energies which were derived from the impedance relaxation peaks are AC in nature. The AC relaxation appears due to the movement of charge carriers associated with dipoles which are frequency dependent and confines with the potential barriers at several interfaces [109-111]. However, the intrinsic grain resistance is of DC source which arises from the movement of the free charge carriers that are frequency independent which accumulates at the various interfaces and heighten the potential barrier. As soon as the free charge carriers conduct at certain elevated temperature, this potential barrier gradually breaks and this let for long range movement of free charge carriers along different interfaces.

The nature of these free charge carriers such as polarons, oxygen vacancies or ions can be calculated from the activation energies derived from the linear portion of the temperature dependent variation of intrinsic resistance [119, 120].We have extracted the value of 'R_i' from the best fitted curve and plotted as a function of temperature as shown in figure. 15 which is found to obey the Arrhenius behaviour of $R = R_o * \exp(E_a^{con}/ k_B T)$, where E_a^{con}- activation energy for the relevant conduction process. We found three Arrhenius regions which are divided into ferroelectric (FE), antiferroelectric (AFE) and paraelectric (PE) regions. The activation energies are calculated and are illustrated in Fig. 7.17.

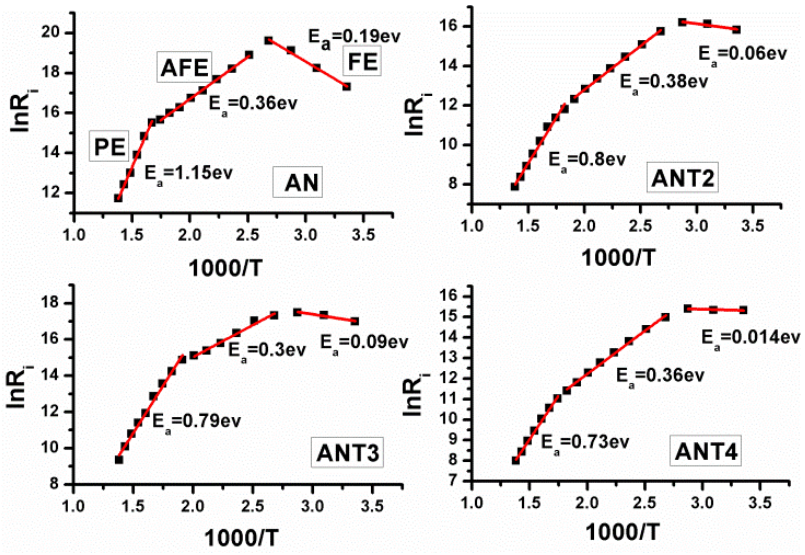

Figure 7.17: Activation energies calculated from Arrhenius formula distinguishes ferroelectric (FE), antiferroelectric (AFE) and paraelectric (PE) regions derived from intrinsic resistance (R_i).

In order to identify the nature of charge defects participated in the observed relaxation and conduction mechanism, we searched the previous literature which have reported the activation energies of approximately equal the value we have obtained. The activation energy estimated in the ferroelectric region and thereafter, throughout the antiferroelectric regions for all the samples are indicated in the figure. Such a low value of activation energies have been mentioned in perovskite oxide and in several complex oxide systems and which are attributed to the migration of localized charge carriers such as polaron. High temperature sintering creates a possibility for presence of oxygen vacancies in metal oxide systems which forces electrons to occupy the site as charge compensators. The lattice distortions somehow accompanied with the compensating electrons to form bound states which often act as effective dipoles. When the electrons hop in association with the lattice distortion in response to the applied ac field that generates short range polaronic

hopping as well and hence, dipole reorientation takes place. Again, the estimated activation energy in the paraelectric region for all the samples is very much similar to the value of ionic conduction or migration of oxygen vacancies. It is reported that small polarons play a vital role during high polarisation whereas the migration of oxygen vacancies has its importance during relaxation processes inside the material [119, 120].

7.4. Conclusion

The $AgNbO_3$ system doped with hole as a charge carrier was successfully prepared by incorporating Ti^{3+} and Ti^{4+} ion in place of Nb^{5+} site. The effect of hole doping impressively improved both the dielectric as well as ferroelectric properties. Dielectric constant increased to an extremely high value with comparatively low dielectric loss. Though, P-E loops are lossy in nature but remnant polarisation has increased ~ 100 times in the ANT4 system for which Jahn-Teller distortion effect is supposed to be a crucial factor. Impedance spectroscopic analysis revealed the presence of both the intrinsic and extrinsic conduction effect in the modified systems within the frequency domain. The resistance of the modified systems decreased drastically which was supposed to be the reason behind lowering of their activation energies. Moreover, TiO_2 doped $AgNbO_3$ system with its improved dielectric and ferroelectric properties can be used as a functional material for high energy storage capacitor and memory applications.

Chapter 8

Conclusion and Future Work

We have successfully prepared the samples of $AgNbO_3$ and its modified systems by conventional solid state route. The dielectric, ferroelectric and impedance spectroscopic studies of the different systems are systematically carried out. As per the objective we have mentioned in the introduction part we are successful in improving the electrical properties and particularly ferroelectric properties. As we have chosen a number of dopants we are able to collect a lot of information. From the isovalent doping systems we are able to get better ferroelectric as well as dielectric properties in the V_2O_5-doped AN system. This modification shows how the changes in surface morphology of the AN system affect its electrical properties. The huge dielectric loss of this system indicates more semiconducting behaviour than insulating property of the parent system and semiconducting ferroelectrics are now seen a wide applications in the electronic industries. In the Sb_2O_5-doped AN system, the results in dielectric as well as ferroelectric are interesting. Particularly, the complete change in shape and nature of the temperature dependent permittivity plot is not properly understood for which structural investigation is necessary which we are planning as our future research proposal.

In the alieovalent doping systems much information were extracted from the experimental results. The effect of charge carriers doping, the effect of electronegativity of the dopants, Presence of Jahn-Teller active cations at octahedral site is better understood by analysing the results. The ferroelectric property particularly remnant polarisation at the 0.4 mole of MnO_2, WO_3 as well as TiO_2 substitution in the AN system. Among the several factors which control octahedral tilting/rotation as discussed in the introduction part, Jahn-Teller distortion will dominate if all the factors coexist in the systems. From the XPS results, the presence of Jahn-Teller cations (Mn^{3+}, W^{5+} and Ti^{3+}) were confirmed and whose numbers increases with the increase dopant concentration. A comparative analysis of all the alieovalent modified systems it is observed that a positive approach with respect to ferroelectric result obtains at higher concentration of dopants. Again only accounting the WO_3-doped AN system, the contrast decreasing and increasing ferroelectric parameters in the AWN2 and AWN4 systems respectively indicates that the number of Jahn-Teller active ions matter a more in bringing improvement in ferroelectric properties. TiO_2-doped system provides the extreme success results in terms of both dielectric as well as ferroelectric properties which can be used in different functional materials.

The impedance spectroscopic analysis successfully provided information regarding the role of precipitated metallic silver particles in the electric properties. Absence of extrinsic conduction within the temperature containing major dielectric anomalies of $AgNbO_3$ indicates that the precipitated metallic silver particles have no such effective role in shaping its dielectric constant or loss which are more intrinsic in nature. In addition to this, low temperature relaxations in the modified systems are related to the accordingly reduction in the activation energies. The resistance of the systems and the activation energies is supposed to be affecting each other apart from other factors reported by previous literatures.

Future scope

(i) To structurally investigate the effect of Jahn-Teller active cations on octahedral distortion.

(ii) To investigate the effect of charge carrier doping at A (Ag)-site of the $AgNbO_3$ ceramic.

(iii) To prepare samples of the modified systems by chemical routes and check the particle size effect on electrical properties.

(iv) To fabricate thin film of the material with suitable substrates and investigate the effect of substrates.

(v) To study the effect of defects created by heavy ion implantation technique.

Bibliography

[1] Hill, N. A. (2000). "Why are there so few magnetic ferroelectrics?" *The Journal of Physical Chemistry B*, *104*(29), 6694-6709.

[2] Woodward, P. M. (1997). "Octahedral tilting in perovskites. I. Geometrical considerations." *Acta Crystallographica Section B: Structural Science*, *53*(1), 32-43.

[3] Woodward, P. M. (1997). "Octahedral tilting in perovskites. II. Structure stabilizing forces." *Acta Crystallographica Section B: Structural Science*, *53*(1), 44-66.

[4] Zhu, J., Li, H., Zhong, L., Xiao, P., Xu, X., Yang, X., & Li, J. (2014). "Perovskite Oxides: Preparation, Characterizations, and Applications in Heterogeneous Catalysis." *ACS Catalysis*, *4*(9), 2917-2940.

[5] Y. Mao, H. Zhou, S. S. Wong, (2010), Synthesis, Properties, and Applications of Perovskite Phase Metal Oxide Nanostructures, *Material Matters* 5.2, 50.

[6] F. Dogan, H. Lin, M. G.Viry and O. Peña, *Sci. Technol. Adv. Mater.* 16 (2015) 020301 (1pp).

[7] Rodel J. Jo W., Seifert T. P. K., Anton E. M and Granzow T, (2009) "Perspective on the Development of the Lead-free Piezoceramics", *J.Am.Ceram.Soc.*, 92[6], 1153-1177.

[8] https://vi.wikipedia.org/wiki/T%E1%BB%AB_%C4%91i%E1%BB%87n_tr%E1%BB%9F_si%C3%AAu_kh%E1%BB%95ng_l%E1%BB%93

[9] http://www.intechopen.com/books/nanowires/multi-physics-properties-in-ferroelectric-nanowires-and-related-structures-from-first-principles

[10] http://www.doitpoms.ac.uk/tlplib/ferroelectrics/printall.php

[11] https://www.quora.com/What-are-the-implications-of-the-newly-proposed-state-of-matter-the-Jahn-Teller-metal

[12] K. C. Cao, Dielectric phenomena of solids.

[13] Physics of Ferroelectrics: A Modern Perspective, edited by. K. Rabe, C. H. Ahn, and J.-M. Triscone (Springer, New York, 2007).

[14] Shimada T. and Kitamura T. "Multi-Physics Properties in Ferroelectric Nanowires and Related Structures from First-Principles"DOI: 10.5772/39520.

[15] Cross,L.E. (1996)."Ferroelectric materials for electromechanical transducer applications." *Materials chemistry and physics*, *43*(2), 108-115.

[16] M. E. Lines and A. M. Glass, Principles and Applications of Ferroelectrics and Related Materials (Clarendon Press, Oxford, 1977).

[17] Valasek, J. (1921). "Piezo-electric and allied phenomena in Rochelle salt." *Physical review*, *17*(4), 475.

[18] Mueller, H. (1940). "Properties of Rochelle salt." *Physical Review*, *57*(9), 829.

[19] Slater, J. C. (1941). "Theory of the transition in KH_2PO_4." *The Journal of Chemical Physics*, *9*(1), 16-33.

[20] Cohen, R. E.; Krakauer, H. *Ferroelectrics* 1992, *136*, 95.

[21] Cohen, R. E. (2000). "Theory of ferroelectrics: a vision for the next decade and beyond." *Journal of Physics and Chemistry of Solids*, *61*(2), 139-146.

[22] Megaw, H. D. (1968). "A simple theory of the off-centre displacement of cations in octahedral environments." *Acta Crystallographica Section B: Structural Crystallography and Crystal Chemistry*, *24*(1), 149-153.

[23] Brown, I. D. (1992). "Chemical and steric constraints in inorganic solids." *Acta Crystallographica Section B: Structural Science*, *48*(5), 553-572.

[24] Hay, P. J., Thibeault, J. C., & Hoffmann, R. (1975). "Orbital interactions in metal dimer complexes." *Journal of the American Chemical Society*, *97*(17), 4884-4899.
[25] Garcia-Fernandez, P., Aramburu, J. A., Barriuso, M. T., & Moreno, M. (2010). "Key role of covalent bonding in octahedral tilting in perovskites." *The Journal of Physical Chemistry Letters*, *1*(3), 647-651.
[26] Mizokawa, T., Khomskii, D. I., &Sawatzky, G. A. (1999). "Interplay between orbital ordering and lattice distortions in $LaMnO_3$, YVO_3, and $YTiO_3$." *Physical Review B*, *60*(10), 7309.
[27] Bilc, D. I., & Singh, D. J. (2006). "Frustration of Tilts and A-Site Driven Ferroelectricity in $KNbO_3$− $LiNbO_3$ Alloys." *Physical review letters*, *96*(14), 147602.
[28] Goldschmidt, V.M. (1926), I: Mat.-Naturv. Kl. No. 2, 8.
[29] Shannon, R. T. (1976). "Revised effective ionic radii and systematic studies of interatomic distances in halides and chalcogenides." *ActaCrystallographica Section A: Crystal Physics, Diffraction, Theoretical and General Crystallography*, *32*(5), 751-767.
[30] Bhuvanesh, N. S., &Gopalakrishnan, J. (1997). "Solid-state chemistry of early transition-metal oxides containing d^0 and d^1 cations." *Journal of material chemistry*, *7*(12), 2297-2306.
[31] Pavarini, E., Yamasaki, A., Nuss, J., & Andersen, O. K. (2005). "How chemistry controls electron localization in 3d1 perovskites: a Wannier-function study." *New Journal of Physics*, *7*(1), 188.
[32] Kugel K. I. and Khomskii D. I., (1982) "The Jahn-Teller effect and magnetism: transition metal compounds", *Sov. Phys. Usp.* 25(4), 231-256.
[33] Lufaso M. W. andWoodward P. M., (2004)"Jahn-Teller distortions, cation ordering and octahedral tilting in perovskites" *ActaCryst.* B 60, 10-20.
[34] Garcia-Fernandez, P., Bersuker, I. B., & Boggs, J. E. (2007). "Why are some ML2 molecules (M= Ca, Sr, Ba; L= H, F, Cl, Br) bent while others are linear? Implications of the pseudo Jahn-Teller effect." *The Journal of Physical Chemistry A*, *111*(41), 10409-10415.
[35] Uchida, K., Tsuneyuki, S., &Schimizu, T. (2003). "First-principles calculations of carrier-doping effects in $SrTiO_3$." *Physical Review B*, *68*(17), 174107.
[36] Wang, Y., Liu, X., Burton, J. D., Jaswal, S. S., &Tsymbal, E. Y. (2012). "Ferroelectric instability under screened coulomb interactions." *Physical review letters*, *109*(24), 247601.
[37] Cohen R. E., (1992) "Origin of Ferroelectricity in Perovskite Oxides", 358, 136-138.
[38] Kuroiwa Y., Aoyagi S., Sawada A., Harada J., Nishibori E., Takata, M., & Sakata, M. (2001). "Evidence for Pb-O covalency in tetragonal $PbTiO_3$." *Physical review letters*, *87*(21), 217601.
[39] Francombe M. H.,& Lewis B. (1958). "Structural and electrical properties of silver niobate and silver tantalate." *ActaCrystallographica*, *11*(3), 175-178.
[40] Lukaszewski M., Kania A., &Ratuszna A. (1980). "Flux growth of single crystals of $AgNbO_3$ and $AgTaO_3$." *Journal of Crystal Growth*, *48*(3), 493-495.
[41] Kravchenko O. Y., Gadzhiev G. G., Omarov Z. M., Reznichenko L. A., Abdullaev K. K., Razumovskaya O. N &Verbenko I. A. (2011). "Phase transformations and properties of $Ag_{1-}yNbO_{3-y/2}$ ($0 \leq y \leq 0.20$) ceramics." *Inorganic Materials*, *47*(8), 919-925.
[42] Lukaszewski L.; Pawelczyk M.; Handerek J. &Kania A. (1983), *Phase Transit*. 3, pp. 247-258.

[43] Pisarski M., & Dmytrow D. (1987). "Phase transitions in ceramic $AgNbO_3$ investigated at high hydrostatic pressure." *Ferroelectrics, 74*(1), 87-93.
[44] Kania A. (1998). "An additional phase transition in silver niobate $AgNbO_3$." *Ferroelectrics, 205*(1), 19-28.
[45] Kania A., Niewiadomski A., Miga S., Jankowska-Sumara I., Pawlik M., Ujma Z &Suchanicz J. (2014). "Silver deficiency and excess effects on quality, dielectric properties and phase transitions of $AgNbO_3$ceramics."*Journal of the European Ceramic Society, 34*(7), 1761-1770.
[46] Zhang T., Zhang C., Wang L., Chai Y., Shen S., Sun Y., Yuan H., and Feng S. (2014). "Low-Temperature Phase Transition in $AgNbO_3$" J. Am. Ceram. Soc., 1–4.
[47] Kania A., Roleder K., &Lukaszewski M. (1984). "The ferroelectric phase in $AgNbO_3$." *Ferroelectrics, 52*(1), 265-269.
[48] Saito A., Uraki S., Taniguchi H., Taniyama T., and Itoh M., (2005) "Growth of Lithium Doped Silver Niobate Single Crystals and Their Piezoelectric Properties," *Mater. Sci. Eng., B*, 120, 166–169.
[49] Fu D., Endo M., Taniguchi H., Taniyama T., &Itoh M. (2007). $AgNbO_3$: "A lead-free material with large polarization and electromechanical." *Applied physics letters, 90*, 252907.
[50] Ratuszna A., Pawluk J., &Kania A. (2003). "Temperature evolution of the crystal structure of $AgNbO_3$." *Phase Transitions: A Multinational Journal,76*(6), 611-620.
[51] Weirauch D. F.,&Tennery V. J., (1967). "Electrical, X-Ray, and Thermal Expansion Studies in the System $KNbO_3$-$AgNbO_3$." *Journal of the American Ceramic Society, 50*(12), 671-673.
[52] Pawełczyk M. (1987). "Phase transitions in $AgTa_xNb_{1-x}O_3$ solid solutions." *Phase Transitions, 8*(4), 273-292.
[53] Verwerft M., Dyck D. V., Brabers V. A. M., Landuyt J. V. & Amelinckx S., (1989), *Phys. Stat. Sol.* (a) 112,451-466.
[54] Kruczek M., Talik E., &Kania A. (2006). "Electronic structure of $AgNbO_3$ and $NaNbO_3$ studied by X-ray photoelectron spectroscopy." *Solid state communications, 137*(9), 469-473.
[55] Grinberg I., &Rappe A. M., (2004). "Silver solid solution piezoelectrics." *Applied physics letters, 85*(10), 1760-1762.
[56] Shigemi A.,& Wada T. (2008). "Crystallographic phase stabilities and electronic structures in AgNbO3 by first-principles calculation." *Molecular Simulation, 34*(10-15), 1105-1114.
[57] Sciau P., Kania A., Dkhil B., Suard E., &Ratuszna A., (2004). "Structural investigation of $AgNbO_3$ phases using x-ray and neutron diffraction." *Journal of Physics: Condensed Matter, 16*(16), 2795.
[58] Levin I., Krayzman V., Woicik J. C. Karapetrova J., Proffen T., Tucker M. G., &Reaney I. M. (2009). "Structural changes underlying the diffuse dielectric response in $AgNbO_3$." *Physical Review B, 79*(10), 104113.
[59] Yashima M., Matsuyama S., Sano R., Itoh M., Tsuda K., & Fu, D. (2011). "Structure of ferroelectric silver niobate $AgNbO_3$." *Chemistry of Materials, 23*(7), 1643-1645.
[60] Niranjan M. K., Asthana S., (2012) "First principles study of lead free piezoelectric $AgNbO_3$ and $(Ag_{1-x}K_x)NbO_3$ solid solutions", *Solid State Communications* 152, 1707–1710.

[61] Chang H. B., Shang M. Y., Zhang C. Y., Yuan H. M., and Feng S. H. "Hydrothermal Syntheses and Structural Phase Transitions of $AgNbO_3$," (2012), *J.Am. Ceram. Soc.*, 95, 3673–77.

[62] Kugel, G. E., Fontana, M. D., Hafid, M., Roleder, K., Kania, A., & Pawelczyk, M. (1987). A "Raman study of silver tantalate ($AgTaO_3$) and its structural phase transition sequence." *Journal of Physics C: Solid State Physics*, *20*(9), 1217.

[63] Hafid, M., Kugel, G. E., Kania, A., Roleder, K., & Fontana, M. D. (1992). "Study of the phase transition sequence of mixed silver tantalate-niobate ($AgTa_{1-x}Nb_xO_3$) by inelastic light scattering." *Journal of Physics: Condensed Matter*, *4*(9), 2333.

[64] Fortin, W. &Kugel, G. E.; Grigas, J. &Kania, A. (1996), J.Appl. Phys. 79, 4273-428.

[65] Volkov A. A., Gorshunov B. P., Komandin G., Fortin W., Kugel G. E., Kania A., &Grigas J. (1995). "High-frequency dielectric spectra of $AgTaO_3$-$AgNbO_3$ mixed ceramics." *Journal of Physics: Condensed Matter*, *7*(4), 785.

[66] Petzelt J., Kamba S., Buixaderas E., Bovtun V., Zikmund Z., Kania A., &Komandin G. (1999). "Infrared and microwave dielectric response of the disordered antiferroelectric Ag $(Ta,Nb)O_3$ system." *Ferroelectrics*, *223*(1), 235-246.

[67] Miga S., Kania A. and Dec J. (2011), "Freezing of the Nb^{5+} ion dynamics in $AgNbO_3$ studied by linear and nonlinear dielectric response", *J. Phys.: Condens. Matter*23**,** 155901-155904.

[68] Nalbandyan V. B.; Medviediev B. S. &Beliayev I. N. (1980), "Study of the Silver Niobate lithium Niobate Systems", Izv.Akad. Nauk SSSR, *Neorg.Mater*. 16, 1819-1823.

[69] Kania A., & Kwapulinski J. (1999). "$Ag_{1-x}Na_xNbO_3$ (ANN) solid solutions: from disordered antiferroelectric $AgNbO_3$ to normal antiferroelectric $NaNbO_3$." *Journal of Physics: Condensed Matter*, *11*(45), 8933.

[70] Kania A. (2001). "Dielectric properties of $Ag_{1-x}A_xNbO_3$ (A: K, Na and Li) and $AgNb_{1-x}Ta_xO_3$ solid solutions in the vicinity of diffuse phase transitions." *Journal of Physics D: Applied Physics*, *34*(10), 1447.

[71] Kania A. and Miga S., (2001) "Preparation and Dielectric Properties of $Ag_{1-x}Li_xNbO_3$ (ALN) Solid Solutions Ceramics," *Mater. Sci. Eng. B*, 86, 128–33.

[72] Takeda T., Takahashi Y., Wada N., &Sakabe Y. (2003). "Effects of substitution of Na and K ions for Ag ion in (Ag, Li) NbO_3Ceramics."*Japanese journal of applied physics*, *42*(9S), 6023.

[73] Fu D., Endo M., Taniguchi H., Taniyama T., Koshihara S. Y., &Itoh M., (2008). "Piezoelectric properties of lithium modified silver niobate perovskite single crystals." *Applied Physics Letters*, *92*(17), 172905-172905.

[74] Fu D., Itoh M., &Koshihara S. Y., (2009). "Dielectric, ferroelectric and piezoelectric behaviors of $AgNbO_3$-$KNbO_3$ solid solution." *Journal of Applied Physics*, *106*(10), 104104-1.

[75] Fu D., Endo M., Taniguchi H., Taniyama T., Itoh M., &Koshihara S. Y., (2011). "Ferroelectricity of Li-doped silver niobate (Ag, Li) NbO_3." *Journal of Physics: Condensed Matter*, *23*(7), 075901.

[76] Fu D., Arioka T., Taniguchi H., Taniyama T., &Itoh M., (2011). "Ferroelectricity and electromechanical coupling in $(1-x)AgNbO_3$-xNaNbO3 solid solutions." *Applied Physics Letters*, *99*(1), 012904.

[77] Hu X., Valant M., & Suvorov D. (2006). "Phase transitions and dielectric properties of the $Ag_{1-x}Bi_{x/3}NbO_3$ system." *Journal of applied physics*,*99*(12), 4109.

[78] Kania, A. (1983), "$AgNb_{1-x}Ta_xO_3$ Solid Solutions-Dielectric Properties and Phase Transitions" *Phase Transit*. 3, 131-139.
[79] Kania A.; Roleder K.; Kugel G. E. & Fontana M. D. (1986*), J. Phys. C: Solid State Phys.* 19, 9-20.
[80] Kania A. (1989). "Flux growth of $AgTa_xNb_{1-x}O_3$ (ATN) solid solution single crystals." *Journal of Crystal Growth*, *96*(3), 703-704.
[81] Sakabe Y., Takeda T., Ogiso Y. & Wada N. (2001), *Jpn. J. Appl. Phys*. Part 1, 42, 5675-5678.
[82] Valant M., Suvorov D., Hoffman C. and Sommariva H. (2001), " Ag(Nb,Ta)O3-based ceramics with suppressed temperature dependence of permittivity" *Journal of the European Ceramic Society*,21, 2647-2651.
[83] Valant M., Axelsson A. K., & Alford N. (2007). "Review of Ag (Nb, Ta) O_3 as a functional material." *Journal of the European Ceramic Society*, *27*(7), 2549-2560.
[84] Valant M., Axelsson A. K., Zou B., & Alford N. (2007). "Oxygen transport during formation and decomposition of $AgNbO_3$ and $AgTaO_3$." *Journal of materials research*, *22*(06), 1650-1655.
[85] Valant M., Suvorov D., & Meden A. (1999). "New High-Permittivity $AgNb_{1-}xTa_xO_3$ Microwave Ceramics: Part I, Crystal Structures and Phase-Decomposition Relations." *Journal of the American Ceramic Society*, *82*(1), 81-87.
[86] Valant M.,& Suvorov D. (1999). "New High-Permittivity $AgNb_{1-x}Ta_xO_3$ Microwave Ceramics: Part II, Dielectric Characteristics." *Journal of the American Ceramic Society*, *82*, 88-93.
[87] Khan H. U., Sterianou I., Miao S., Pokorny J., & Reaney I. M. (2012). "The effect of Li-substitution on the M-phases of $AgNbO_3$." *Journal of Applied Physics*, *111*(2), 024107.
[88] Guo X., Zhu N., Xiao M., & Wu X. (2007). "Structural and Dielectric Properties of Ag $(Nb_{0.\ 8}Ta_{0.\ 2})_{1-\ x}Sb_xO3$ ($x \leq 0.08$) Ceramics." *Journal of the American Ceramic Society*, *90*(8), 2467-2471.
[89] Koh J. H., Khartsev S. I., and Grishin A., (2000) "Ferroelectric Silver Niobate-Tantalate Thin Films," *Appl. Phys. Lett.*, 77, 4416–8.
[90] Telli M. B., Bharadwaja S. S. N., Biegalski M. D., and Trolier-Mckinstry S., (2006), "(001) Epitaxial AgTaO3 and AgNbO3 Thin Films on (001) SrRuO3/(001) LaAlO3 Substrates by Chemical Solution Deposition," *Appl. Phys. Lett.*, 89, 252907, 3pp.
[91] Sakurai H., Yamazoe S., and Wada T., (2010), "Ferroelectric and Antiferroelectric Properties of $AgNbO_3$ Films Fabricated on (001), (110), and (111) $SrTiO_3$ Substrates by Pulsed Laser Deposition," *Appl. Phys. Lett.*, 97, 042901, 3pp
[92] Kato H., Kobayashi H., &Kudo A. (2002). "Role of Ag+ in the band structures and photocatalytic properties of AgMO3 (M: Ta and Nb) with the perovskite structure." *The Journal of Physical Chemistry B*, *106*(48), 12441-12447.
[93] Li G., Kako T., Wang D., Zou Z., & Ye J. (2009). "Enhanced photocatalytic activity of La-doped AgNbO 3 under visible light irradiation." *Dalton Transactions*, (13), 2423-2427.
[94] Li G., Yan S., Wang Z., Wang X., Li Z., Ye J., &Zou Z. (2009). "Synthesis and visible light photocatalytic property of polyhedron-shaped $AgNbO_3$." *Dalton Transactions*, (40), 8519-8524.
[95] Wu W., Liang S., Chen Y., Shen L., Yuan R., & Wu L. (2013). "Mechanism and improvement of the visible light photocatalysis of organic pollutants over

microcrystalline $AgNbO_3$ prepared by a sol–gel method." *Materials Research Bulletin*, *48*(4), 1618-1626.
[96] AndrisSutka and GundarsMezinskis, Front. *Mater. Sci*. 6 (2012) 128–141.
[97] Raul Valenzuela, Magnetic ceramics, New York, Cambridge university press, 1994.
[98] A.B. Salunkhe, V.M. Khot, M.R. Phadatare, S.H. Pawar, (2012), *Journal of Alloys and Compounds* 514 91–96.
[99] http://lipidlibrary.aocs.org/physics/xray/index.htm, 15/07/2015.
[100] B D Cullity, Elements of X-Ray Diffraction, Addison-Wesley Publishers, 1978.
[101] S K Kulakarni, Nanotechnology: principles and practice, Capital publishing company.
[102] Jin Zhong Zhang, Optical properties and spectroscopy of nanomaterials, world scientific publications
[103] http://www.photometrics.net/fesem.html, 15/07/2015.
[104] Vadim F. Lvovich, Impedance spectroscopy: Applications to Electrochemical and Dielectric Phenomena, a john wiley& sons, inc., publication, 2012.
[105] R. L. Jones, M. Thrall, and C. M. B. Henderson, (2010) *Mineralogical Magazine* 74 507-519.
[106] D. Xu, S. Cao, J. Zhang, B. Cheng and J. Yu, (2014)"Effects of the preparation method on the structure and the visible-light photocatalytic activity of Ag_2CrO_4" BeilsteinJ.Nanotechnol., 5, 658–666.
[107] L. Yang, J. Liu, H. Chang and S. Tang, RSC Adv. 5 (2015) 59970–59975.
[108] B D Cullity and C D Graham, Introduction to magnetic materials, (2012) A John Willey& Sons, inc publication,.
[109] E. Barsoukov and J. R. Macdonald, *Impedance Spectroscopy Theory, Experiment, and Applications*, 46 (Wiley, Hoboken, NJ, 2005).
[110] Gerhardt R. (1994). "Impedance and dielectric spectroscopy revisited: distinguishing localized relaxation from long-range conductivity." *Journal of Physics and Chemistry of Solids*, *55*(12), 1491-1506.
[111] Almond D. P., & West A. R. (1983). "Impedance and modulus spectroscopy of "real" dispersive conductors." *Solid State Ionics*, *11*(1), 57-64.
[112] N. Ortega, Ashok Kumar, P. Bhattacharya, S. B. Majumder, and R. S. Katiyar, (2008), "Impedance spectroscopy of multiferroic $PbZr_xTi_{1-x}O_3/CoFe_2O_4$ layered thin films", Phys. Rev. B 77, 014111.
[113] Lia G., Kako T., Wang D., Zou Z., Ye J., (2007), "Composition dependence of the photophysical and photocatalytic properties of (AgNbO3)1-x(NaNbO3)x solid solutions" Journal of Solid State Chemistry, 180, 2845–2850.
[114] Li G., Bai Y., Zhang W. F., Zhang H., (2013), "Enhanced visible light photocatalytic properties of AgNbO3/AgSbO3 composites", Materials Chemistry and Physics 139, 1009-1013.
[115] Mathpal M.C., Kumar P., Kumar S., Tripathi A.K., Singh M.K., Prakash J. and Agarwal. A, (2015), "Opacity and plasmonic properties of Ag embedded glass based metamaterials", *RSC Adv.*, 5, 12555-12562.
[116] Mukherjee S., Srivastava A., Gupta R., &Garg A. (2014). "Suppression of grain boundary relaxation in Zr-doped $BiFeO_3$ thin films." *Journal of Applied Physics*, *115*(20), 204102.
[117] F. Hong, Z. Cheng, S. Zhang and X. Wang, (2012), "Dielectric relaxation in the $DyMn_{1-x}Fe_xO_3$" *J. Appl. Phys.* 111, 034104.

[118] C.V.Ramana, Y.D.Kolekar, K. Bharathi, B. Sinha, and K.Ghosh, (2013), "Correlation between structural, magnetic, and dielectric properties of manganese substituted cobalt ferrite", *J. Appl. Phys.* 114, 183907.
[119] Raymond O., Font R., Suarez-Almodovar N., Portelles,J., & Siqueiros J. M. (2005). "Frequency-temperature response of ferroelectromagnetic Pb ($Fe_{1/2}Nb_{1/2}$)O_3 ceramics obtained by different precursors. Part II. Impedance spectroscopy characterization." *Journal of applied physics*, *97*(8), 084108.
[120] Raymond O., Font R., Portelles J., Suárez-Almodovar N., & Siqueiros J. M. (2006). "Frequency-temperature response of ferroelectromagneticPb($Fe_{1/2}Nb_{1/2}$)O_3 ceramics obtained by different precursors. III. Dielectric relaxation near the transition temperature." *Journal of applied physics*, *99* (12), 124101.
[121] Tamilselvan A., Balakumar S., Sakar M., Nayek C., Murugavel P., & Kumar K. S. (2014). "Role of oxygen vacancy and Fe–O–Fe bond angle in compositional, magnetic, and dielectric relaxation on Eu-substituted $BiFeO_3$ nanoparticles." *Dalton Transactions*, *43*(15), 5731-5738.
[122] Jayakumar O. D., Achary S. N., Girija K. G., Tyagi A. K., Sudakar C., Lawes G., &Ahuja R. (2010), "Theoretical and experimental evidence of enhanced ferromagnetism in Ba and Mn co substituted $BiFeO_3$." *Applied Physics Letters*, *96*(3), 032903.
[123] Panda R. K., &Behera D. (2014). "Investigation of electric transport behaviour of bulk $CoFe_2O_4$ by complex impedance spectroscopy." *Journal of Alloys and Compounds*, *587*, 481-486.
[124] Panda R. K., Muduli R., Kar S. K., &Behera D. (2014). "Dielectric relaxation and conduction mechanism of cobalt ferrite nanoparticles." *Journal of Alloys and Compounds*, *615*, 899-905.
[125] Panda R. K., Muduli R., &Behera D. (2015). "Electric and magnetic properties of Bi substituted cobalt ferrite nanoparticles: Evolution of grain effect." *Journal of Alloys and Compounds*, *634*, 239-245.
[126] Wu Y.,& Cao G. (1999). "Enhanced ferroelectric properties and lowered processing temperatures of strontium bismuth niobates with vanadium doping." *Applied physics letters*, *75*(17), 2650-2652.
[127] Wu Y.,& Cao G. (2000). "Influences of vanadium doping on ferroelectric properties of strontium bismuth niobates." *Journal of materials science letters*, *19*(4), 267-269.
[128] Yin P., Lingxia L., Lifeng C., &Qingwei L. (2012). "Correlation between crystal structure and properties of ultra-high dielectric constant ceramics x$SrCO_3$-Bi_2O_3-Ag (Nb,Ta)O_3." *Journal of electroceramics*, *28*(4), 209-213.
[129] Ogawa H., Taketani H., Kan A., Fujita A., and Zouganelis G., *J. Eur. Ceram. Soc.* 25 (2005) 2859–63.
[130] Ogawa H., Kan A., and Ishihara S., (2003) *J. Eur. Ceram. Soc.* 23, 2485–88.
[131] Jiang J., Kucernak A., (2002), Electrochemical super capacitor material based on manganese oxide:preparation and characterization". *ElectrochimicaActa*, 47, 2381-2386.
[132] Cabuk, S., &Simsek, S. (2008). "First-principles studies of the electronic structure and optical properties of AgBO3 (B= Nb,Ta) in the paraelectric phase." *Open Physics*, *6*(3), 730-736.
[133] Khyzhun O.Y., "XPS, XES and XAS studies of the electronic structure of tungsten oxides" (2000), *J. Alloys and Compounds*, 305, 1–6.

[134] S. Hashimoto and A. Tanaka, (2002), "Alteration of Ti 2p XPS spectrum for titanium oxide by low-energy Ar ion bombardment" *Surf. Interface Anal*. 34,262–265.
[135] Das, R., Khan, G. G., &Mandal, K. (2012). "Enhanced ferroelectric,magnetoelectric, and magnetic properties in Pr and Cr co-doped BiFeO3 nanotubes fabricated by template assisted route." Journal of Applied Physics, 111(10), 104115.
[136] Muduli, R., Pattanayak, R., Kumar, S., Kar, S. K., Kumar, P., Panigrahi, S., & Panda, R. K. (2016). "Dielectric, ferroelectric and impedance spectroscopic study of Ta_2O_5, Sb_2O_5, and V_2O_5-doped $AgNbO_3$ ceramic." Journal of Alloys and Compounds, 656, 33-44.
[137] GhoshA., Phys. Rev. B 47 (1993) 15 537-15 542.

List of Publications:

1. **R. Muduli**, R. Pattanayak, S. Kumar, S. K. Kar, P. Kumar, S. Panigrahi, R. K. Panda, Journal of Alloys and Compounds 656 (2016) 33-44.
2. **R. Muduli**, R. Pattanayak, S. Raut, P. Sahu, S. V, S. Rath, P. Kumar, S. Panigrahi, R.K. Panda,Journal of Alloys and Compounds664(2016) 715-725.
3. **R. Muduli**, P. Kumar, R.K.Panda, S. Panigrahi, accepted, Materials of Chemistry and physics.
4. R K Panda, **R Muduli,** D Behera, Journal of Alloys and Compounds 615 (2014) 899-905.
5. R K Panda, **R Muduli,** D Behera, Journal of Alloys and Compounds 634 (2015) 239-245.
6. R patnayak, S Panigrahi, T Dash, **R Muduli**, D Behera, Physica B: Condensed Matter 474 (2015)57-63.
7. R Pattanayak, **R Muduli**, R K Panda, T Dash, P Sahu, S Raut1, S Panigrahi, Physica B: Condensed Matter accepted.

Curriculum Vitae:

Rakesh Muduli

Research Scholar

Department Physics & Astronomy

National Institute of Technology, Rourkela

Odisha

India, Pin-769008

Education:

10^{th} class, Board of secondary education, Odisha	1995
12^{th} class, Council of Secondary Education, Odisha	1997
Bachelor in Physics, Utkal University, Odisha,	2000
Master in Physics, Utkal University, Odisha	2003

Research Scholar and pursuing Ph.D.2011-
Department of Physics and Astronomy
NIT Rourkela